Università degli Studi di Padova

Dipartimento di Scienze Chimiche

SCUOLA DI DOTTORATO DI RICERCA IN SCIENZE MOLECOLARI

INDIRIZZO SCIENZE CHIMICHE

CICLO XXVIII

ULTRAFAST RELAXATION DYNAMICS OF MULTICHROMOPHORIC SYSTEMS THROUGH ADVANCED OPTICAL SPECTROSCOPIES

Direttore della Scuola : Ch.mo Prof. Polimeno Antonino

Coordinatore d'indirizzo: Ch.mo Prof. Polimeno Antonino

Supervisore :Ch.ma Prof.ssa Collini Elisabetta

Dottorando : Luca Bolzonello

Contents

Abstract

The light-matter interaction is one of the most interesting phenomena occurring in Nature. The interaction with light provides energy to the molecules, which is then released in the process of relaxation. This thesis deals with the investigation of relaxation mechanisms of molecules from a semi-quantum point of view. The use of quantum mechanics models is necessary to understand the operations and the results of advanced optical spectroscopies, such as 2D electronic spectroscopy, used precisely for the study of excitation and relaxation of molecules. The study and characterization of relaxation processes is of crucial importance to devise strategies to exploit and gain energy from them. Relaxation, as widely known, is strongly influenced by the surroundings and by the vibrations of the molecules. Therefore, we compared the relaxation dynamics of two systems with very different couplings with the environment. The first are aggregates of porphyrins that have weak coupling with the environment. However, it will be shown that the excitation is coupled with low frequency vibrations. The second is a quadrupolar system studied in its monomeric and dimeric form in different solvents. Surprisingly, a strong coupling between the dye transitions and a vibration of the solvent molecules was found. If confirmed, this effect could lead to new strategies for engineering light harvesting systems.

Abstract (italiano)

L'interazione luce-materia è sicuramente uno dei più interessanti fenomeni in Natura. L'interazione con la luce fornisce energia alle molecole, che viene poi rilasciata nel processo di rilassamento. Questa tesi tratta meccanismi di rilassamento di molecole da un punto di vista semi-quantomeccanico. Questa trattazione è necessaria per comprendere il funzionamento e i risultati di spettroscopie ottiche avanzate, come la spettroscopia ottica 2D, utilizzate appunto per lo studio dell'eccitazione e del rilassamento delle molecole. Lo studio e la caratterizzazione di processi di rilassamento è di fondamentale importanza per ideare strategie per sfruttare il rilassamento al fine di ricavare parte dell'energia. Rilassamento che, come è noto, è fortemente influenzato dall'intorno e dalle vibrazioni delle molecole. Si sono quindi confrontate le dinamiche di rilassamento di due sistemi caratterizzati da accoppiamenti con l'intorno molto diversi. Il primo sistema considerato sono aggregati di porfirine che hanno uno scarso accoppiamento con l'intorno. Tuttavia si dimostrerà invece che tali sistemi sono caratterizzati da un forte accoppiamento con vibrazioni a bassa frequenza. Il secondo invece è un sistema quadrupolare del quale si studiano sia il monomero che il dimero in solventi diversi. Sorprendentemente si è trovato un forte accoppiamento delle molecole con una vibrazione del solvente, che se si dimostrerà vera, potrebbe aprire a nuove strategie per l'ingegnerizzazione di sistemi di light harvesting.

INTRODUCTION

Nature is a continuous fight between thermodynamics and kinetics. Thermodynamics decides where a system has to go whereas kinetics tells it how. Thermodynamics would send a system to an equilibrium, tending to a minimum of energy. Kinetics simply makes the system to follow the faster path. The first evidence of discrepancy between them is the theory of Marcus[1], [2]. Marcus law is a kinetic law for electron transfer. It states that the most thermodynamically favorable process is not necessarily the faster. Let's think to charge separation that takes place in a solar cell. Thermodynamics states that charges must recombine. Kinetic makes charges to migrate to the electrodes before recombination. An immediate recombination would not allow exploiting the energy of recombination.

Generally, a system needs an external perturbation to get out of the equilibrium reaching a state with an excess of energy. Then, the excess energy will be released going back to the equilibrium. Controlling how it "relaxes" gives the possibility of exploiting the energy of such a process.

Focalizing on molecular systems, light is the main tool used by Nature to perturb equilibrium, providing excess energy to the molecules. Once out of the equilibrium, molecules relax through a great variety of processes. Nature engineers very smart processes to convey relaxation energy in useful processes. For example, in the case of photosynthesis, the excited state generated by the absorption of a photon, preferentially relaxes back not by reemitting a photon, the thermodynamically favorable process, but charge separation takes place because it is simply faster. The study of the interaction between light and molecules and the relaxation of the excited state is the main task of optical spectroscopy.

In particular, ultrafast time-resolved spectroscopy looks at excited state relaxation to unravel the secrets of energy dynamics. Understanding these relaxation processes is the basis for engineering and exploiting efficient systems to collect energy.

Energy transfer (ET) is one of the most important relaxation processes taking place in light harvesting systems. At room temperature, the two main ET mechanisms are the Forster ET [3] and the Dexter ET [4]. The former is based on the assumption of dipolar interactions and exploits the resonance between the states of the molecules involved, while the latter is essentially a double electron transfer. Forster ET is the most widely applied and successful model applied to describe ET in natural or artificial systems.

The progress of the knowledge of dynamical processes can be tracked with technological advancements and the ability to perform experiments with increasing time resolution. The advent of the laser in the 1960s pushed resolution from microseconds to nanoseconds to picoseconds. Recently, advancement of laser technology allows controlling visible laser pulses with few femtoseconds of time duration, the same order of magnitude of quantum oscillations. This capability, tuned in new experimental techniques, opens new possibilities for investigating and understanding the energy dynamics of complex systems.

The exploitation of these new technologies leads, for example, to the discovery of a new energy transfer scheme possibly active at room temperature called quantum coherent energy transfer. It is based on the superposition between states sited on different molecules that allows the excitation to follow the most convenient path[5]. Quantum coherent energy transfer is thought to be responsible of the great energy transfer yield in natural light harvesting systems.

This discovery was very surprising because at room temperature the coherence between electronic states dephases very quickly and this should not give to the system the time necessary to perform quantum transfer. However, it is hypothesized that coherence survives because of the favorable environment. The environment, which is usually the main responsible of the dephasing of quantum superpositions, could help coherence with its structure, vibrations and noise. In natural light harvesting complexes, the proteic scaffold keeps the numerous chlorophylls in an appropriate geometry. Moreover, also the presence of suitable environmental fluctuations or suitable vibrations could keep electronic states in coherence for times longer than expected or even recreate coherence between them after dephasing [6]. Thus, the environment that surrounds molecules is absolutely crucial in their relaxation dynamics.

There are still many open questions about quantum transfer, its effective relevance in Nature and the possibility of exploiting it in artificial devices. Techniques able of capturing experimental evidences for quantum transfer are currently at the forefront of optical spectroscopy.

The first aim of this thesis was to develop a set of setups for optical techniques able indeed to capture the subtle quantum effects in excitation relaxations. As result, one of the few setups currently available for 2D photon echo spectroscopy was successfully built in our labs. Attempts of implementing other novel techniques, such as broadband time-resolved circular dichroism, were also done, although with less success. Pioneering the implementation of novel techniques is not always easy but we are confident in further improvements. The theoretical background necessary to understand the design of these novel ultrafast techniques and to grasp the physical meaning of their results is outlined in Chapter 1. Chapter 2 describes instead the experimental details of the optical setups and the analysis toolbox suitably developed for the data analysis and interpretation.

The second main aim was then to use these techniques to analyze the relaxation dynamics in systems characterized by different couplings with the environment and ascertain the role of fluctuations and vibrations in the possible presence of quantum mechanism of energy relaxation. Chapter 3 reports detailed experimental results for a molecular system (a porphyrin J-aggregate) in which the strong electronic coupling between the molecules guarantees a very weak coupling with the environment. Nevertheless, we found that coupling with vibrational states are instead crucial in the energy relaxation process. Chapter 4 treats the opposite case of a monomer (and the relative dimeric form) of a charged molecule strongly interacting with the environment and the surrounding solvent molecules. The characterization of the relaxation dynamics of these systems in different solvents allowed demonstrating a very peculiar influence of solvent molecules.

1 LIGHT-MOLECULES INTERACTION

Interaction between light and matter is one of the most important and extraordinary events happening in Nature. There are different physical models to describe this interaction: purely classical such as Drude's model[7] or Lorentz's model, purely quantum and semi-classical. The compromise between accuracy and clarity is to treat the molecule quantum mechanically with time-dependent perturbation theory but to consider light, the perturbation, as a purely classical oscillating electric field. This semi-classical approach can well explain many of the phenomena associated with absorption of light. Moreover, perturbation theory is an exceptional tool to describe even non-linear phenomena, for the capacity of describing in different orders of perturbation each interaction between electromagnetic field and molecules. This make it the fundamental tool used by molecular spectroscopists to study light-induced phenomena on molecules.

Quantum mechanics is essentially based on the description of the behavior of a system with a wavefunction. Wavefunction encloses all the possible information about the system. Wavefunction and its time evolution can be derived by solving the time-dependent Schrödinger equation [8]:

$$\mathcal{H}\Psi = i\hbar\frac{\partial\Psi}{\partial t} \tag{1}$$

where $\mathcal{H}$ is the Hamiltonian containing potential and kinetic energy of the system and Ψ is the wavefunction. If the Hamiltonian is independent of time, the equation can be rewritten in the form:

$$\mathcal{H}_0\Psi = E\Psi \tag{2}$$

where E is the energy of the system. This is called time independent Schrödinger equation and generally, its solutions are a set of eigenfunctions (or eigenstates) ψ_k with associated eigenenergies E_k. Eigenstates are orthonormal and form a complete set of functions. This means that it is possible to describe any possible wavefunction by a linear combination of them.

In the perturbation theory, the total Hamiltonian of a quantum system perturbed by a time-varying electromagnetic field, with the assumption of a relatively small perturbation, can be described by the sum of the Hamiltonian of the unperturbed system H_0, which is time independent, and the time dependent perturbation term H'(t):

$$\mathcal{H}(t) = \mathcal{H}_0 + \mathcal{H}'(t) \tag{3}$$

since the eigenstates of the H_0 form a complete set, is possible to describe the new solution of the perturbed system with a linear combination of the ψ_k:

$$\Psi(\mathrm{t}) = \sum_k C_k(t)\psi_k e^{\frac{-i(E_k)t}{\hbar}} \tag{4}$$

It is expected that an unperturbed system will be found in the lowest energy eigenstate *a* before light perturbation starts, so C_a=1 and $C_{k\neq a}$=0. When the light perturbation is activated, what happens is that the coefficients of excited states start to grow with a speed that follow this relation:

$$\frac{\partial C_{k\neq a}}{\partial t} = -\left(\frac{i}{\hbar}\right)\langle\psi_{k\neq a}|\mathcal{H}'|\psi_a\rangle e^{\frac{-i(E_{k\neq a}-E_a)t}{\hbar}} \tag{5}$$

Essentially, light induces transitions between quantum state of molecules.

However, this model describes time evolution of a single system knowing its initial state. To describe an ensemble it is better to use the density matrix formalism.

It is possible to include all the time dependence of the wavefunction in new coefficients c_k:

$$\Psi(\mathrm{t}) = \sum_k c_k(t)\psi_k = \sum_k C_k(t)\psi_k e^{\frac{-i(E_k)t}{\hbar}} \tag{6}$$

The expectation value of any dynamic property of the quantum system can be found with the expression:

$$\langle A(t)\rangle = \langle \Psi(\mathrm{t})|\tilde{A}|\Psi(\mathrm{t})\rangle = \sum_k \sum_l c_k^* c_l \, A_{kl} \tag{7}$$

Thus, all the time dependence of the system resides in the array of products of the coefficients. It is convenient to define a matrix ρ with elements:

$$\rho_{kl}(t) = \; c_k^*(t) c_l(t) \tag{8}$$

The great advantage of using density matrix is that it can separate coherences from populations. In fact, its diagonal elements are equal to the probability of finding the system in state *k* at time *t*:

$$\overline{\rho_{kk}}(t) = \; |C_k^*(t)|^2 \tag{9}$$

Whereas the off-diagonal elements are coherences between states:

$$\overline{\rho_{kl}}(t) = \; C_k^*(t) C_l(t) e^{\frac{-i(E_k - E_l)t}{\hbar}} \tag{10}$$

Essentially, it can elegantly distinguish the cases in which the populations are equally distributed in 2 states statistically:

$$\rho = \begin{pmatrix} \frac{1}{2} & 0 \\ 0 & \frac{1}{2} \end{pmatrix}$$

from coherent superpositions of the two states:

$$\rho = \begin{pmatrix} \frac{1}{2} & \frac{1}{2} \\ \frac{1}{2} & \frac{1}{2} \end{pmatrix}$$

1.1 PERTURBATIVE EXPANSION

To better describe the time evolution of a quantum system perturbed by pulses of light, it is better to move to the interaction picture, where the time evolution operator describes the time dependence of the system[9]:

$$U_0(t,t_0) = e^{\frac{-iH_0(t-t_0)}{\hbar}} \tag{11}$$

The new wavefunctions in the interaction picture can be expressed as:

$$|\psi(t)\rangle = U_0(t,t_0)|\psi_I(t)\rangle \tag{12}$$

where $\psi(t)$ is the wavefunction of the full Hamiltonian H(t), whereas $U_0(t,t_0)$ is the time evolution operator with respect to the system Hamiltonian H_0 only. Hence, the time dependence of $\psi_I(t)$ describes the time evolution of the wavefunction caused by the difference between H(t) and H_0, that, from equation 3, is the electromagnetic perturbation H'(t).

The great advantage of this approach is that it is possible to rewrite the Schrödinger equation as:

$$\frac{\partial|\psi_I(t)\rangle}{\partial t} = -\frac{i}{\hbar}\mathcal{H}'(t)|\psi_I(t)\rangle \tag{13}$$

where the Hamiltonian operator is now only the perturbation of light.

In case of multiple interactions, as in the case of multiple laser pulses, it is useful to integrate this equation defining different time intervals, each one representing time delay between interactions:

$$\begin{aligned}|\psi_I(t)\rangle &= |\psi_I(t_0)\rangle - \frac{i}{\hbar}\int_{t_0}^{t}\mathcal{H}_I'(t)|\psi_I(t)\rangle = \\ &|\psi_I(t_0)\rangle \\ &+\sum_{n=1}^{\infty}\left(-\frac{i}{\hbar}\right)^n\int_{t_0}^{t}d\tau_n\int_{t_0}^{\tau_n}d\tau_{n-1}\dots\int_{t_0}^{\tau_2}d\tau_1\ \mathcal{H}_I'(\tau_n)\,\mathcal{H}_I'(\tau_{n-1})\dots\mathcal{H}_I'(\tau_1)\,|\psi_I(t_0)\rangle\end{aligned} \tag{14}$$

and going back to the Schrödinger picture:

$$
\begin{aligned}
&|\psi(t)\rangle \\
&= \left|\psi^0(t)\right\rangle + \sum_{n=1}^{\infty}\left(-\frac{i}{\hbar}\right)^n \int_{t_0}^{t} d\tau_n \int_{t_0}^{\tau_n} d\tau_{n-1} \dots \int_{t_0}^{\tau_2} d\tau_1 \\
&\times\ U_0(\tau_n, t_0)\mathcal{H}_I{}'(\tau_n)\, U_0(\tau_n, \tau_{n-1})\, \mathcal{H}_I{}'(\tau_{n-1}) \dots\ U_0(\tau_1, t_0)\mathcal{H}_I{}'(\tau_1)\, \left|\psi_I(t_0)\right\rangle
\end{aligned}
\tag{15}
$$

The same treatment can be done for the density matrix that is, as anticipated, more suitable for the description of ensembles. Moreover, substituting the perturbation Hamiltonian with the explicit form describing the dipolar interaction between the electric field and the dipole moment $\mathcal{H}_I{}'(t) = -E(t)\mu_I(t)$, we obtain:

$$
\begin{aligned}
\rho(t) = \rho^0(t) + \sum_{n=1}^{\infty}\left(-\frac{i}{\hbar}\right)^n \int_{t_0}^{t} d\tau_n \int_{t_0}^{\tau_n} d\tau_{n-1} \dots \int_{t_0}^{\tau_2} d\tau_1\, E(\tau_n)E(\tau_{n-1}) \dots E(\tau_1) \\
\times\ U_0(t, -\infty)[\mu_I(\tau_n)[\mu_I(\tau_{n-1}) \dots [\mu_I(\tau_1), \rho(-\infty)] \dots]]\ U_0{}^{\dagger}(t, -\infty)
\end{aligned}
\tag{16}
$$

Equation 16 shows an expansion at nth order of the density matrix. Each order of expansion corresponds to a perturbation at a specific time of the electromagnetic field by dipole interaction. This is incredibly useful in ultrafast spectroscopy, when the system is excited by ultrashort pulses, as described in the next section.

1.2 POLARIZATION AND SPECTROSCOPY

Most of ultrafast spectroscopies typically measure an induced macroscopic polarization generated in the material as a response of light perturbation.

For a weak electric field, the polarization depends linearly on the strength of the electric field:

$$P = \varepsilon_0 \chi^{(1)} E \tag{17}$$

where $\chi^{(1)}$ is the linear optical susceptibility and ε_0 the vacuum dielectric constant.

However, dealing with ultrafast pulses and intense electric fields, non-linear effects become non-negligible and therefore the polarization has to be described as a power expansion of the electric field:

$$P = \varepsilon_0 (\chi^{(1)} E + \chi^{(2)} EE + \chi^{(3)} EEE + \cdots) \tag{18}$$

where $\chi^{(n)}$ are the n^{th} order optical susceptibilities. The electric field is a vector, thus the linear and nonlinear susceptibilities are tensors. In media with inversion symmetry, such as isotropic systems like solutions, even-order susceptibilities vanish. Therefore, for most media the lowest nonlinear order is the 3rd-order.

Macroscopic polarization can be written also in term of expectation value of the dipole operator on the density matrix:

$$P(t) = \langle \mu \rho(t) \rangle \tag{19}$$

For example, in a 2 level system:

$$\rho = \begin{pmatrix} \rho_{11} & \rho_{12} \\ \rho_{21} & \rho_{22} \end{pmatrix} \qquad \mu = \begin{pmatrix} 0 & \mu_{12} \\ \mu_{21} & 0 \end{pmatrix} \tag{20}$$

and the polarization equals to:

$$P(t) = \langle \begin{pmatrix} 0 & \mu_{12} \\ \mu_{21} & 0 \end{pmatrix} \begin{pmatrix} \rho_{11} & \rho_{12} \\ \rho_{21} & \rho_{22} \end{pmatrix} \rangle = \mu_{12}\rho_{21} + \mu_{21}\rho_{12} \tag{21}$$

What comes from equation 21 is that only off-diagonal elements of the density matrix generate macroscopic polarization and thus can emit light.

If we substitute the expansion of density matrix in equation 16 into equation 19 and explicit the electric field E, it becomes evident how the orders of expansion of the density matrix correspond to the increasing orders of the nonlinear polarization in equation 18, so that

$$\begin{aligned} P^{(n)}(t) &= \langle \mu\rho^{(n)}(t) \rangle \\ &= \left(-\frac{i}{\hbar}\right)^n \int_{t_0}^{t} d\tau_n \int_{t_0}^{\tau_n} d\tau_{n-1} \dots \int_{t_0}^{\tau_2} d\tau_1 \, E(\tau_n)E(\tau_{n-1}) \dots E(\tau_1) \\ &\times \langle \mu(t)[\mu(\tau_n)[\mu(\tau_{n-1}) \dots [\mu(\tau_1), \rho(-\infty)] \dots]] \rangle \end{aligned} \tag{22}$$

Now, it is possible to replace all the absolute times τ with time intervals t fixing the time of the first interaction τ_1=0. In these conditions, the polarization takes the form:

$$\begin{aligned} P^{(n)}(t) = \left(-\frac{i}{\hbar}\right)^n \int_0^{\infty} dt_n \int_0^{\infty} dt_{n-1} \dots \int_{t_0}^{\tau_2} dt_1 \, E(t - t_n)E(t - t_n - t_{n-1}) \dots E(t - t_n \\ - t_{n-1} \dots - t_1) \times S^{(n)}(t_n, t_{n-1}, \dots, t_1) \end{aligned} \tag{23}$$

where $S^{(n)}$ is the nth order optical response function:

$$S^{(n)}(t_n, t_{n-1}, \dots, t_1) = \left(-\frac{i}{\hbar}\right)^n \langle \mu(t_n + \cdots t_1)[\mu(t_{n-1} + \cdots t_1) \dots [\mu(0), \rho(-\infty)] \dots] \rangle \tag{24}$$

The nonlinear polarization induced in the sample is then given by the convolution of the various optical fields with this response function. It is important to notice the role of the last interaction compared to the previous interactions: the interactions at all the other times generate a non-equilibrium density matrix whose off-diagonal elements at time (t_n+…t_1) emit an electric field, while the last interaction is not part of the commutator and acts only as a “probe”.

The response function is a sum of many interactions acting both on the left side (ket) and right side (bra) of the density matrix [9]–[11]. A pictorial and easy way to represent all these interactions is by the schematic double-sided Feynman diagrams. The time evolution of the bra and ket is represented by two vertical lines. Interactions with the perturbation are represented by diagonal arrows pointing in or out the time lines. Each one represents absorption or emission of radiation, respectively. The sum of all possible combinations gives the total n^{th} response function.

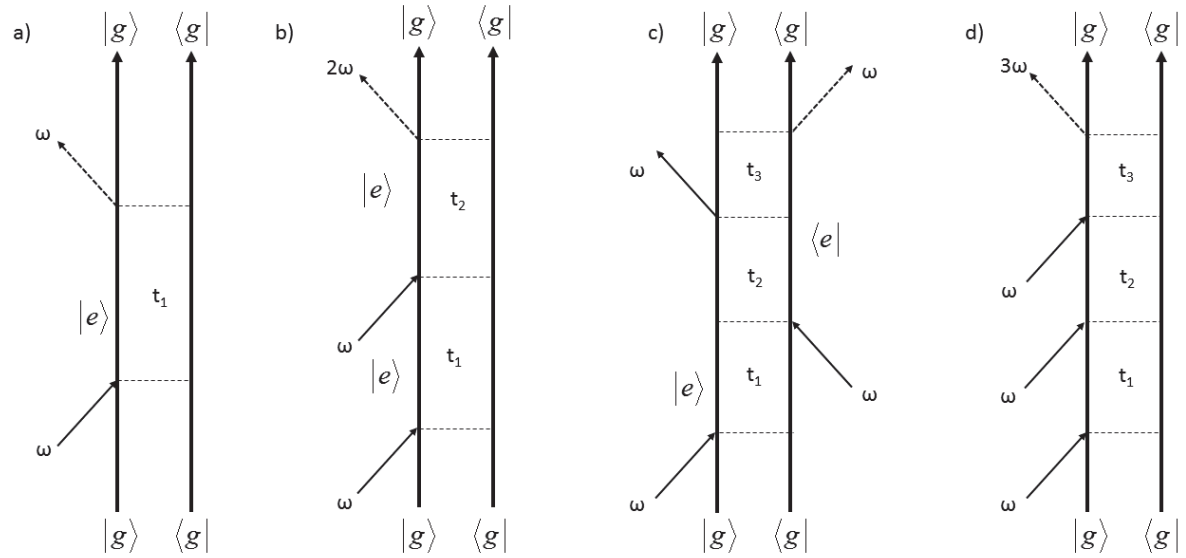

Figure 1 Examples of double-sided Feynman diagrams at different orders. a) linear absorption (n=1); b) second harmonic generation (n=2); c) stimulated emission (n=3) and d) third harmonic generation (n=3). Intervals between interactions are defined as t_n.

Each Feynman diagram represents a Feynman path, which is a virtual path through real or virtual states coupled at each perturbation by the perturbation ω. Figure 1 reports some example of Feynman diagram for the first (n=1), second (n=2) and third (n=3) order of perturbation.

If the aim is to study the evolution of excited states, the minimum number of necessary interactions is three. In fact, first, two pulses are needed to interact on the opposite sides of the Feynman diagram to generate a pure excited state $|e\rangle\langle e|$ (see figure 1, panel c). Then, a third interaction is necessary to stimulate the signal.

The total third order signal is the sum of 864 terms, which are essentially the permutations of all possible Feynman paths [9]. Extracting information from signals with this great number of contributions could be difficult. It is however possible to select only some group of terms through suitable experimental conditions:

- Time ordering
- Phase matching
- Rotating wave approximation.

A detailed explanation of how the choice of time ordering, phase matching, etc. can effectively remove some contribution to the final signal can be found in [10]. For the purpose of this thesis is however worthy to highlight that a careful design of the experiment is crucial to achieve the desired signal. Within the experimental conditions, only 4 terms (and their c.c.) survive. The third order response function could be written as sum of these 4 terms:

$$S^{(3)} = \sum_{n=1}^{4} R_n \tag{25}$$

where each R_n corresponds to a Feynman path (figure 2).

To follow the excited state, we want to stimulate Feynman paths that generate the pure excited state $|e\rangle\langle e|$ with the first two interactions and, with the third interaction, make the system to emit the third order signal in the same frequency range of the perturbation. This process is called stimulated emission (SE) and correspond to R_1 and R_2 Feynman paths. These are ideal terms to study the evolution of the excited state along t_2 time interval. There is no experimental conditions that allow separating R_1 and R_2 from R_3 and R_4 Feynman paths, which correspond to ground state bleaching (GSB) process. In GSB terms the ground state and not the excited state evolves during t_2. However, it is possible by phase matching conditions to separate R_2 and R_3 from R_1 and R_4. These configurations are called rephasing and non-rephasing and collect the signal in the phase matching direction $k_s=-k_1+k_2+k_3$ and $k_s=k_1-k_2+k_3$, respectively.

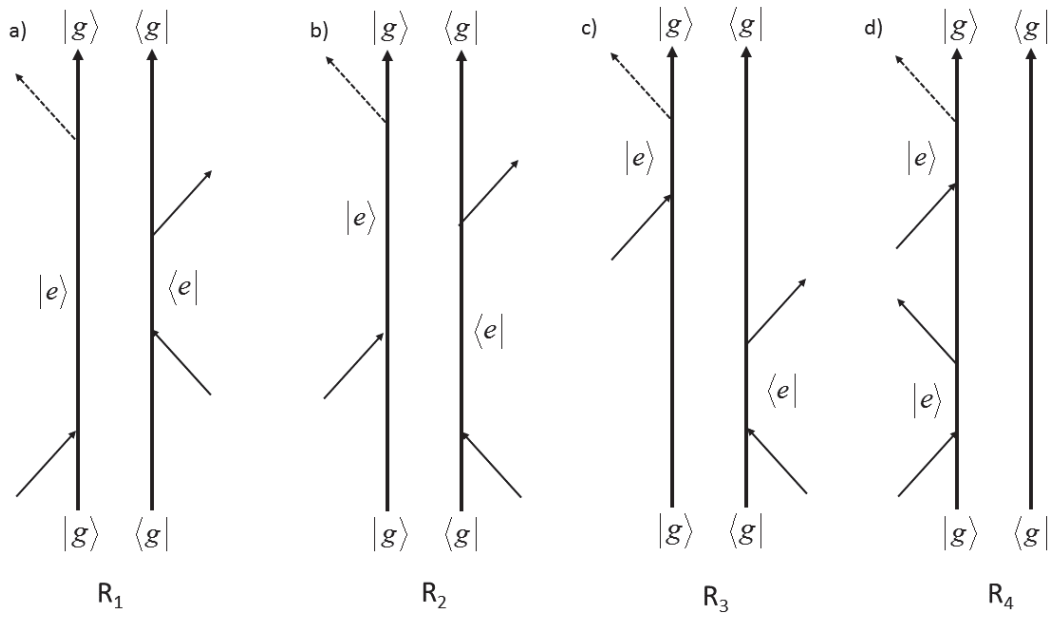

Figure 2 Feynman diagrams corresponding to different Feynman paths contributing to third order response. a) and b) correspond to R_1 and R_2 two stimulated emission paths, while c) and d) correspond to R_3 and R_4, ground state bleaching paths. SE and GSB can be distinguished based on the state evolving during t_2: the excited state in the former while the ground state in the latter.

However, they are not the only contributions to the signal. In fact, we have excluded all the terms where the last interaction generates population in the excited state. Two examples are reported in figure 3 panel a and b. Moreover, also contributions of excited state absorption (ESA) were neglected (figure 3 panel c). The ESA terms contribute to the signal only if states at double of the energy of the laser are present (2*e*).

A third experimental configuration that could be useful for studying excited states is called double quantum (2Q or 2Q2D) and appears along $k_s=k_1+k_2-k_3$. In the terms that contribute to this configuration the system never reaches a pure state (figure 3 panel d). Instead, a coherence between the ground state and a state with twice the energy of the laser is generated. This configuration can highlight any energetic correlation between the excited state *e* and the possible doubly excited state 2*e*.

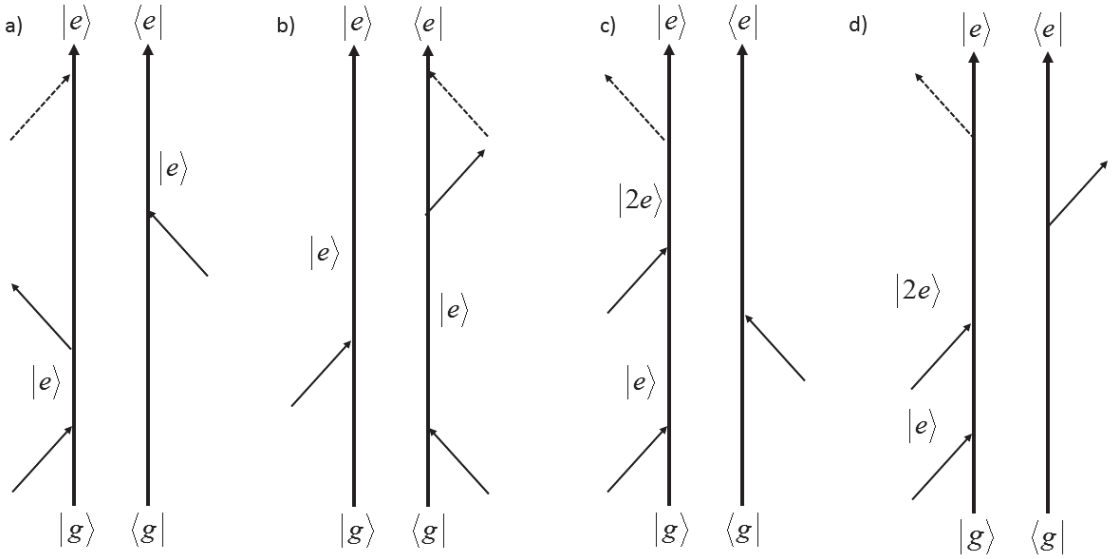

Figure 3 a) and b) show two Feynman paths that end in the excited state $|e\rangle\langle e|$. c) represents a path responsible of ESA contribution and d) a 2Q diagram.

1.3 RELAXATION AND LINE SHAPE

In the previous section, we demonstrated that radiation is generated by coherence between states. Thus, only off diagonal elements of the density matrix contribute to the emission of radiation. An isolated system with two states put in coherence by a laser pulse, will oscillate continuously between the two states and it will generate a radiation with a frequency matching the energy gap between the states. However, spectroscopy usually deals with macroscopic polarization, generated by a great number of individual systems that form an ensemble. Each individual system is surrounded by a slightly different environment that acts differently on them. Because of dynamic or static differences between frequencies and phases of the oscillation of each system, the macroscopic oscillation that generates the radiation is eventually damped.

To better understand this behavior it is convenient to follow the example of the absorption spectrum. The linear absorption spectrum A(ω) is proportional to the to the electric field emitted by the off diagonal coherences that are in turn proportional to the first order polarization induced on the system. It is possible to demonstrate that the absorption spectrum is proportional to the Fourier transform of the time evolution of the correlation function of dipole moment [9]

$$A(\omega) \propto Re \int_0^\infty dt\, e^{-i\omega t} \langle \mu(t)\mu(0)\rho(-\infty)\rangle = \quad Re \quad \int_0^\infty dt\, e^{-i\omega t} \langle \mu_{ab}(t)\mu_{ba}(0)\rho_{aa}\rangle \qquad (26)$$

Equation 26 shows the case in which radiation is in resonance with the energy gap of states *a* and *b* of the system. Figure 4 displays examples of correlation functions of dipole moment and the relative FT in different conditions that will be now described.

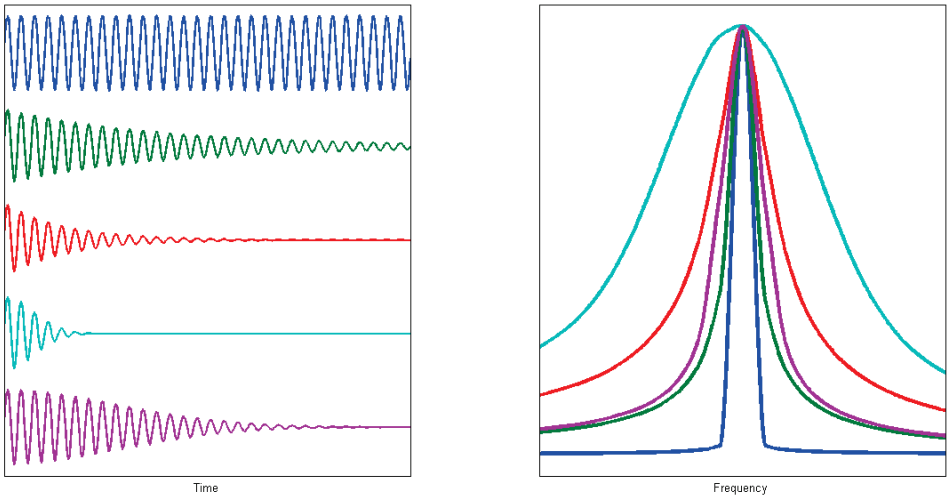

Figure 4 The left panel shows dipole moment correlation functions characterized by different relaxation conditions with the corresponding Fourier spectrum in the right panel. Blue line represents the case of no relaxation. Green and red lines represent the case of homogeneous relaxation with long and short correlation time, respectively. Cyan and purple lines represent the inhomogeneous case with short and long correlation times, respectively. The longer is the correlation time, the narrower is the correspondent spectrum. Moreover, inhomogeneous cases show gaussian shaped spectra, whereas homogeneous cases are chracterized by lorentzian shapes.

Without any interaction, the off diagonal elements in the density matrix generated by the pulse never decay and the system oscillates indefinitely at ω_{ab}. In this case, the absorption spectrum will be described by a delta function:

$$A(\omega) \propto Re \int_0^\infty dt\, e^{-i\omega t} e^{i\omega_{ab} t} = 2\pi\delta(\omega_{ab} - \omega) \tag{27}$$

This case is represented by the blue line in figure 4. However, in real systems, the interaction of each molecule with other molecules, with the environment, vibrations etc. will induce the decay of

coherences. Specifically, if we have an ensemble of molecules with different environments, ω_{ab} will be different for each molecule. This 'static' disorder usually generates a Gaussian distribution of ω_{ab}. Moreover, ω_{ab} of a single system can dynamically fluctuate for the various and singular interactions of each molecule. Thus ω_{ab} becomes time dependent and in these conditions the absorption is described by:

$$A(\omega) \propto Re \int_0^\infty dt\, e^{-i\omega t} e^{i\int_0^t d\tau\, \omega_{ab}(\tau)} \tag{28}$$

It is convenient to separate $\omega_{ab}(t)$ in a time averaged frequency $\overline{\omega_{ab}}$ and the time dependent deviation from it $\delta\omega_{ab}(t)$

$$\omega_{ab}(t) = \overline{\omega_{ab}} + \delta\omega_{ab}(t) \tag{29}$$

Obtaining

$$A(\omega) \propto Re \int_0^\infty dt\, e^{-i\omega t} e^{i\overline{\omega_{ab}}t} e^{i\int_0^t d\tau\, \delta\omega_{ab}(\tau)} \tag{30}$$

With the aim of solving the integral $\int_0^t d\tau\ \delta\omega_{ab}(\tau)$ at the exponential, $\delta\omega_{ab}(\tau)$ is expanded in power series. This is called cumulant expansion[10]. After suitable approximations, it allows the definition of the spectral lineshape $g(t)$ that is by definition the correlation function of $d\omega$

$$g(t) = \int_0^t \int_0^{\tau'} d\tau' d\tau'' \langle d\omega(\tau'') d\omega(0)\rangle \tag{31}$$

We can then rewrite the absorption spectrum as

$$A(\omega) \propto Re \int_0^\infty dt\, e^{-i\omega t} e^{i\overline{\omega_{ab}}t} e^{-g(t)} \tag{32}$$

The simplest approach to write explicitly *g(t)* is to express the correlation function $\langle d\omega(t)d\omega(0)\rangle$ in terms of Δ, the amplitude of deviation $d\omega$ from $\overline{\omega_{ab}}$, and τ_c, a time constant describing the correlation time:

$$\langle d\omega(t)d\omega(0)\rangle = \Delta^2 e^{-\frac{t}{\tau_c}} \tag{33}$$

then $g(t)$ becomes:

$$g(t) = \Delta^2\tau_c^2\left[e^{-\frac{t}{\tau_c}} + \frac{t}{\tau_c} - 1\right] \tag{34}$$

that is called Kubo line shape[12], [13]. This is a very important result because it can describe all the possible mechanisms of broadening. For example, long correlation time well describes static or inhomogeneous broadening, i.e. when different molecules have different transition frequencies due to their different environments but they do not fluctuate. In this case:

$$g(t) = \frac{\Delta^2 t^2}{2} \tag{35}$$

$$A(\omega) \propto Re\int_0^\infty dt\, e^{-i\omega t}e^{i\overline{\omega_{ab}}t}e^{\frac{\Delta^2 t^2}{2}} \tag{36}$$

that corresponds to a Gaussian function centered in $\overline{\omega_{ab}}$ and with width Δ. In other words, the absorption spectrum follows the distribution of energies of the molecules of the ensemble. This case is described by cyan and purple lines in figure 4.

On the other hand, a short correlation time means that fluctuations in frequency and phase are rapid. For example, a molecule changes rapidly its instantaneous frequency in the whole range Δ. This is the homogeneous limit. In this case:

$$g(t) = \Delta^2\tau_c t = \frac{t}{T_2} = \Gamma t \tag{37}$$

where $\Delta^2\tau_c = \frac{1}{T_2} = \Gamma$ is the decay constant of the exponential that 'damps' the oscillation between *a* and *b*. The resulting absorption spectrum is

$$A(\omega) \propto Re \int_0^\infty dt\, e^{-i\omega t} e^{i\overline{\omega_{ab}}t} e^{-\Gamma t} = \frac{2\Gamma}{(\omega - \overline{\omega_{ab}}) + \Gamma^2} \tag{38}$$

that is a Lorentzian function centered on ω_{ab}. Γ is the decay constant that includes contributions of both decay of the excited state $\frac{1}{2T_1}$ and pure dephasing $\frac{1}{T_2{}^*}$. The first contribution stands for the loss of coherence due to loss of population in the excited state. The second is due to the randomization and distribution of ω_{ab}. These cases are represented by green and red lines in figure 4.

There is also another process, called spectral diffusion. In this case, the fluctuations of ω_{ab} within Δ have typical times longer than the oscillation period, but they are not fixed as in the case of inhomogeneous broadening. This generates a Voigt profile that is essentially the convolution of a Lorentzian with a Gaussian function.

The treatment outlined above for the description of linear signals can be generalized for higher-order signals and the line shape function *g(t)* can be used for the calculation of the response function of any order of polarization. For example, we report the case of R_2 Feynman path, which is part of the total third order response function.

$$\begin{aligned} R_2(t_1, t_2, t_3) &= \langle \mu(t_1 + t_2 + t_3)\mu(t_1)\rho(-\infty)\mu(0)\mu(t_1 + t_2)\rangle \\ &= -\left(\frac{i}{\hbar}\right)^3 \mu^4 e^{-i\omega(t_3 - t_1)} e^{-g(t_1)+g(t_2)-g(t_3)-g(t_1+t_2)-g(t_2+t_3)+g(t_1+t_2+t_3)} \end{aligned} \tag{39}$$

The third order polarization is described more in detail in the section 1.5.

Other theoretical models can be used to describe *g(t)* in different ways to be able to describe for example the temperature dependence of *g(t)*. In Brownian oscillator model, the phenomenological amplitude Δ of the fluctuations is replaced by a more meaningful displacement on the nuclear potential surface

induced by the temperature. Other models include spectral density of the solvent or quantum coupling with the vibrations as quickly outlined in the next section.

1.4 CONTRIBUTION OF VIBRONIC COUPLING IN THE LINE SHAPE FUNCTION

Molecules consist of electrons and nuclei reciprocally interacting, whose overall behavior is described by Schrödinger equation. However, it is not possible to calculate exact solutions of Schrödinger equation for these kind of systems and it becomes thus necessary to make approximations. The main approach to solve this issue is called adiabatic approximation (AA). AA makes use of a time-scale separation between fast and slow degrees of freedom assuming that the motion of electrons is much faster than nuclei due to their large difference in mass. This means that electrons adapt very rapidly to any change in nuclear geometry. There are three main levels in adiabatic approximation: crude adiabatic (CA), Born-Oppenheimer approximation (BO) and Born-Huang approximation (BH). Independently on the approximation used, the important common characteristic of the AA is the possibility to express the total wavefunction as a product of vibrational and electronic wavefunctions and thus the total energy as sum of electronic and vibrational ones:

$$\Psi = \psi_{el}(q, Q)\chi_{vib}(Q) \qquad \mathrm{E} = E_{el} + E_{vib} \tag{40}$$

where q are the electronic coordinates and Q the nuclear ones. Vibrational wavefunctions are dependent only on nuclear coordinates. Electrons affect the vibrational wavefunctions only by generating the potential surface in which nuclei are free to move. The electronic wavefunction is instead dependent on both electronic and vibrational coordinates. The difference between the three aforementioned approaches lies exactly on the description of potential surface in which nuclei move. The simplest approach, CA, consists in calculating electronic wavefunctions and energies at the equilibrium nuclear coordinates Q_0. The vibrational wavefunctions are then calculated for each electronic state in an arbitrary potential surface.

On the contrary, in BO and BH approximations, the potential surface in which nuclei can move comes from the calculation of the electronic energy. In other words, the potential surface is built calculating the energy of each electronic state along Q coordinates. An exhaustive description of such couplings and approximations is not in the interest of this thesis but could be found in [14], [15].

Within adiabatic approximation, we want to focalize on how vibronic coupling can influence the electronic transitions and the relative line shape functions treated in previous sections. Applying dipole moment operator between vibronic wavefunctions in different electronic states, we obtain

$$M(Q) = \langle g_i(q,Q)|\mu(q)|e_j(q,Q)\rangle \tag{41}$$

where g_i and e_j identifies the vibronic wavefunctions in the electronic states g and e and with vibrational states i and j. It is convenient to remove the moment dependence on nuclear coordinates Q. The simplest method is to expand the moment around the equilibrium coordinates Q_0.

$$M_{g_i,e_j} = \langle g(q,Q_0)|\mu(q)|e(q,Q_0)\rangle\langle i_g(Q)|j_e(Q)\rangle + \left(\frac{\delta M(Q)}{\delta Q}\right)_0 \langle i_g(Q)|Q|j_f(Q)\rangle + \cdots \tag{42}$$

The truncation at the first term of this expansion leads to the Frank-Condon approximation and physically means that nuclei do not move during electronic transition. This is often a good approximation. In this expression, it is possible to notice that the intensity of the transition between two vibronic states is proportional to the integrals between vibrational wavefunction in the two different electronic states $\langle i_g(Q)|j_e(Q)\rangle$, called Condon factors. If we assume that the potential curves in the two electronic states have the same shape, the only parameter that determines the Condon factors is the displacement or shift along the nuclear coordinates between them.

Now we want to calculate the spectral line shape $g(t)$ in case of vibronic transitions. The model used is represented in figure 5 panel a with two electronic states g and , described by harmonic potentials, and a vibrational mode with frequency ν coupled to them. Initially, only g_0 is populated.

It is possible to demonstrate that in these conditions, $g(t)$ can be written as [16]:

$$g(t) = -D\left(e^{-i\nu t} - 1\right) \tag{43}$$

where D is the displacement between the minima of the two potential curves and ν is the frequency of the vibration.

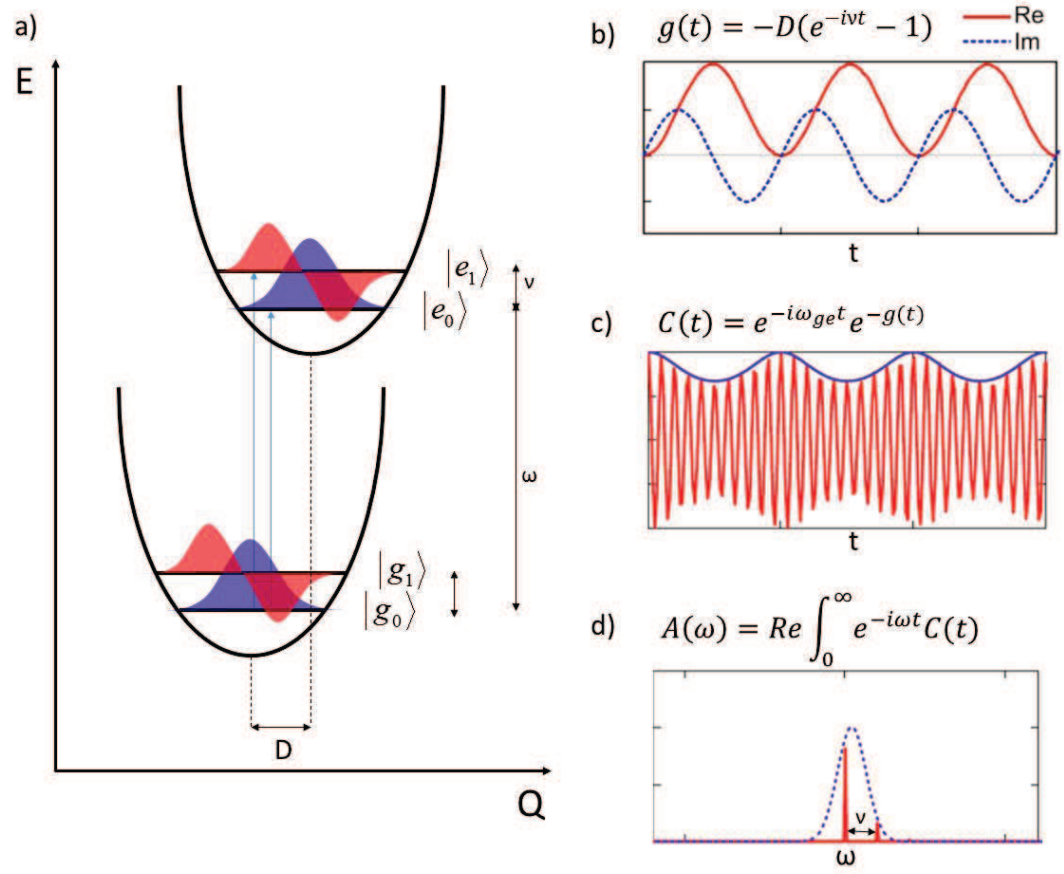

Figure 5 a) Vibrational states lying in the ground and excited electronic potential curves. The displacement D make the transition toward the excited state to end in different vibronic states. b) The time evolution of line shape $g(t)$. c) The time dependence of the correlation function of the dipole moment $C(t)$. d) Absorption spectrum $A(\omega)$ coming from the FT of $C(t)$. The modulation of $C(t)$induced by $g(t)$ generate a new peak at $\omega + \nu$. Insets b,c and d are adapted from Tokmakoff's lessons slides.

Panels b, c and d of figure 5 show the time dependence of $g(t)$, the time dependence of the correlation function of the dipole moment, and the correspondent absorption spectrum, respectively. $g(t)$ oscillates with frequency ν and thus modulates the intensity of the electronic transition. A new peak with frequency $\omega + \nu$ therefore appears in the resulting absorption spectrum. If $D = 0$ only one vibrational state is excited because only $\langle 0_g(Q)|0_e(Q)\rangle$is not vanishing. Moreover, $g(t) = 0$ and this means that electronic transition is not modulated in time.

The case illustrated in figure 5 is just a simple example to show how the vibronic coupling contributes to the optical response. A similar approach could be applied to the description of the time resolved

spectra treated in this thesis. Despite the complexity of the treatment, the important message is that the coupling between electronic and vibrational states can be included in the description of $g(t)$, which in turns enters in the expression of the response function (like for example in equation 39) of any order and may give rise to oscillations in the time-resolved signals (figure 5 c).

1.5 THIRD-ORDER POLARIZATION AND 2D SIGNAL

As stated in section 1.2, third order polarization is the most informative signal for excited states. The best way to understand this process is to follow systematically from a pictorial point of view, what happens at the density matrix level when laser pulses interact with the sample.

As example, we consider a 3 level system with ground state *g*, and two excited states *e* and *f*. We assume that at equilibrium conditions, before the interaction with the field, only *g* is populated: $\rho_{gg} = 1; \rho_{ee} = \rho_{ff} = \rho_{ge} = \rho_{gf} = \rho_{ef} = \rho_{eg} = \rho_{fg} = \rho_{fe} = 0$. The laser spectrum is broad enough to excite simultaneously both *e* and *f* states.

When the first pulse reaches the sample, it generates a coherence between the ground state and each of the two excited states. In the density matrix picture, it promotes the population in the diagonal element : ρ_{gg} to the off-diagonal elements that represent the coherences. Figure 6 shows schematically this process and the two Feynman diagrams that represent the two interactions giving rise to the coherences. Also interactions to the left part of the Feynman diagram that promotes ket states contribute to the signal. For simplicity, in next figures only R_2 Feynman path is reported, representing the SE term of the rephasing signal.

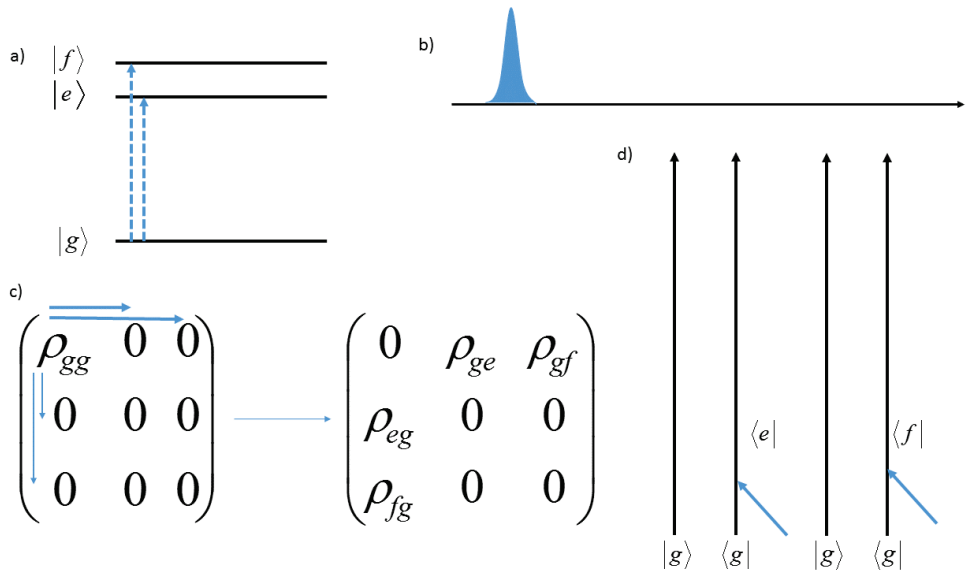

Figure 6 a) shows the interaction with the first pulse in the energy levels picture. Dashed lines represent the interaction with the bra, i.e. the right part of the Feynman diagram d). b) shows the time arrival of the first pulse. c) shows the variations in the density matrix induced by the interaction. Bold lines represent changes induced by R_2 path, taken as example.

Once $|g\rangle\langle e|$ and $|g\rangle\langle f|$ coherences are generated, they start to dephase during the first time interval t_1 as explained in section 1.3. Room temperature typically makes the coherences to dephase quickly. Thus, the second laser pulse has to reach the sample before the coherences between excited states and ground state are completely damped. The second laser pulse can interact with both right and left side of Feynman diagram. In the case of R_2 path, it interacts with the left side. In both examples, it promotes the ket from *g* to *f*. In the first case, it generates a coherence, but this time between the two excited state$|e\rangle\langle f|$. This contribution is an oscillatory component of the total signal, which oscillates during the time interval t_2 with a frequency proportional to the energy difference between the two states *e* and *f* until the coherence dephases completely. In the second case, it generates a pure state $|f\rangle\langle f|$ that is free to evolve during the second time interval t_2. Summarizing, pure excited states and/or the coherences between the excited states evolve along t_2.

Other contributions not shown in figure 7 are those interacting with the right side. In this case, the pulse sends the ket back to the ground state, which "evolves" during t_2. If, for example, a fourth state is present at about twice the energy of *e* or *f*, the second pulse could excite again the bra generating a coherence between the ground state and this additional state. In this case, the coherence oscillates at frequency double with respect to that of the laser. This is the case of double quantum 2D experiment that will be treated later.

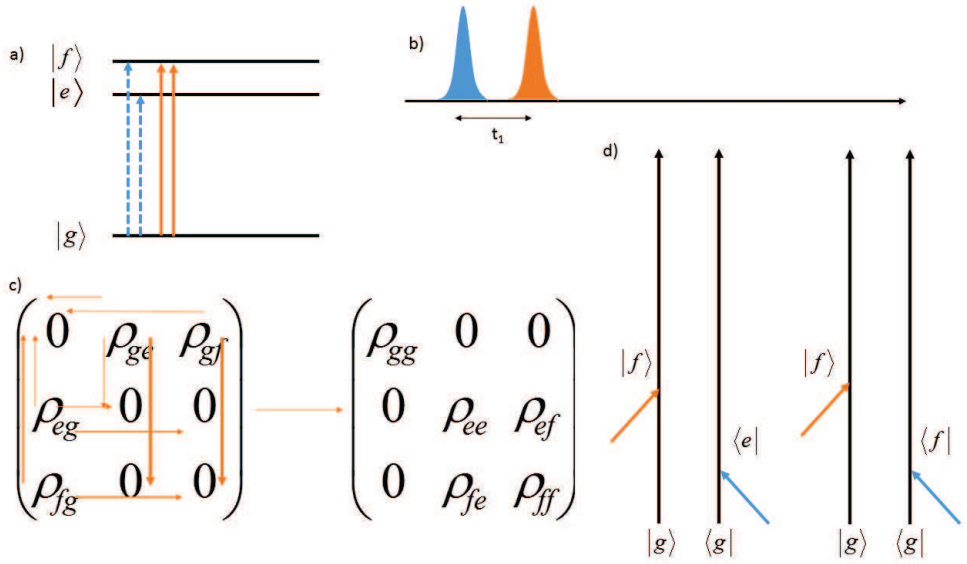

Figure 7 a) shows the interaction with the second pulse in the energy levels picture. Solid lines represent the interaction with the ket, i.e. the left part of the Feynman diagram d). b) shows the time arrival of the second pulse. c) shows the variations in the density matrix induced by the interaction. Bold lines represent changes induced by R_2 path, taken as example.

After t_2, the third pulse reaches the sample generating again coherences between the excited states and the ground one. In the example reported in figure 8, the third pulse sends the bra to the ground state. Then, the coherence between *g* and *e* in the first case and between *g* and *f* in the second will dephase emitting light (the signal).

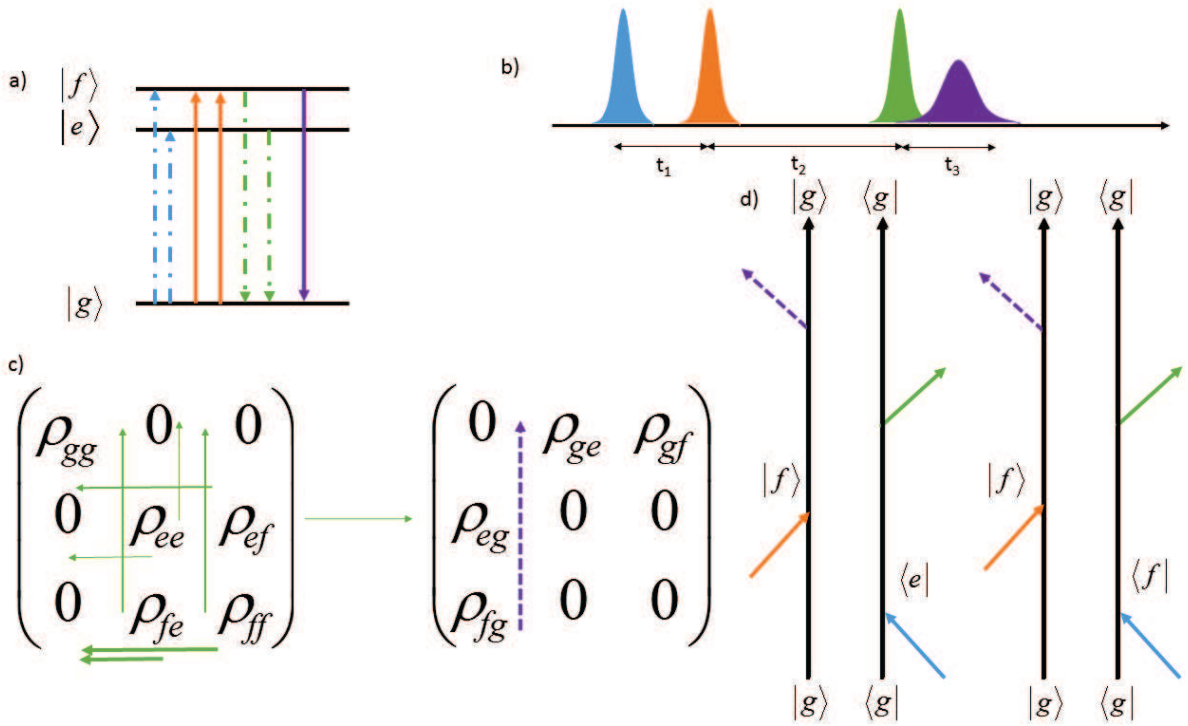

Figure 8 a) shows the interaction with the third pulse in the energy levels picture. Solid and dashed lines represent the interaction with ket and the bra, i.e. the left and the right part of the Feynman diagram d) respectively. b) shows the time arrival of the third pulse. c) shows the variations in the density matrix induced by the interaction. Bold lines represent changes induced by R_2 path, taken as example.

The signal corresponding to R_2 Feynman path is emitted in the direction $k_s=-k_1+k_2+k_3$ that is the phase matching condition for the rephasing signal. However, as explained in section 1.2, in the same direction other Feynman diagrams contribute to the total signal such as R_3 and ESA terms.

The total signal as a function of the three time intervals t_1, t_2 and t_3 is difficult to interpret and visualize. On contrary, it is really convenient to transform the signal as a function of ω_1 and ω_3 by Fourier transforming along t_1 and t_3:

$$S(t_1, t_2, t_3) \rightarrow S(\omega_1, t_2, \omega_3) \tag{44}$$

The new signal has a more meaningful form. The two time intervals where coherences between ground and excited states evolve are expressed in the frequency domain. Thus, it is possible to correlate the intensities of such coherences with their frequencies or energies. It is then possible to build 2D maps where x and y axes correspond respectively to ω_1 and ω_3, where intensities of signals of different terms and different states are displayed as peaks at different coordinates. An example of rephasing map of the system treated above is reported in figure 9. In the figure it is also shown where and how the various peaks appear, highlighting the difference between homogeneous and inhomogeneous broadening. Furthermore, crosspeaks, due to SE scheme, indicate coherences between state *e* and *f*. Finally, the negative ESA peak denotes the presence of higher states.

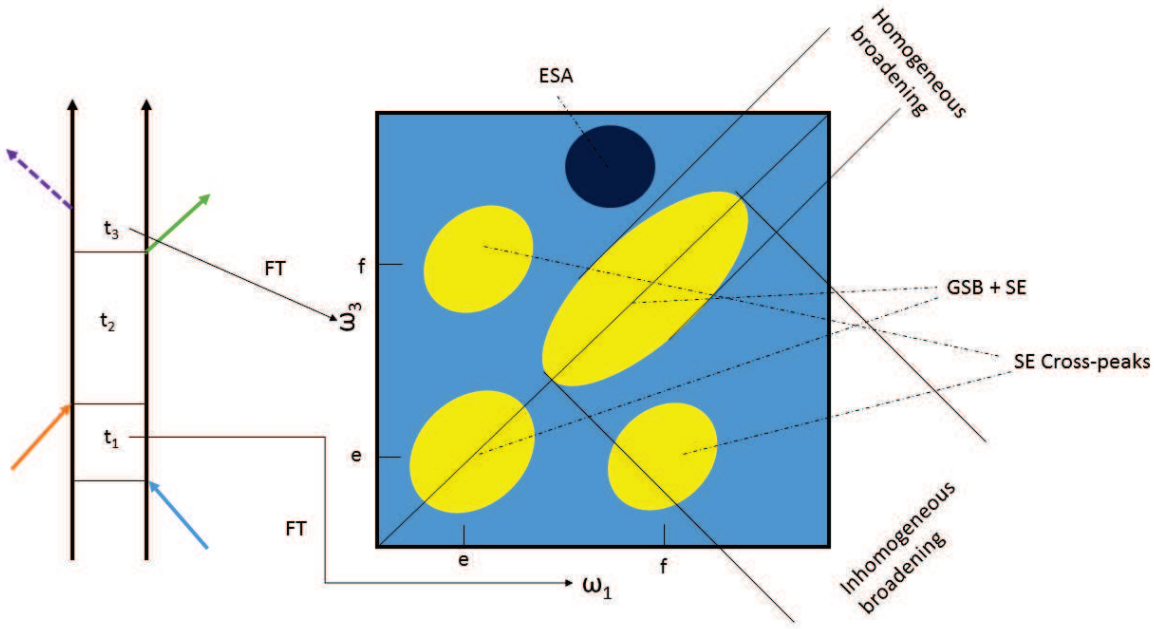

Figure 9 Typical structure of a 2D map. The signal is fourier transformed along time interval t_1 and t_3. The new dependence on ω_1 and ω_3 is conveniently visualized in the 2D map with these frequencies reported as x and y axes, respectively. The signal appears in the map as positive (GSB and SE) or negative (ESA) peaks. Coordinates of peaks are related to the energies of the states involved in the third order signal, in this case e and f. The shape of peaks can reveal and distinguish homogeneous and inhomogeneous broadening. Crosspeaks reveal the presence of coherences between state e and f.

The complete third order signal can be visualized as a set of 2D maps evolving along time t_2. Evolution of 2D maps along t_2 is related to the evolution of ground state (R_3 or GSB) and excited states (R_2 or SE). The peaks due to Feynman paths where during t_2 a pure states ($|f\rangle\langle f|$ or $|e\rangle\langle e|$) evolves, decay with

the dynamic of the corresponding state. Thus, studying the time properties of peaks is informative of dynamics of states. On contrary, the peaks due to Feynman paths where coherences ($|f\rangle\langle e|$ or $|e\rangle\langle f|$) evolve during t_2, have an oscillatory behavior. In particular, coherences' peaks (i.e. crosspeaks of figure 9) oscillate with a frequency proportional to the energy gap of the two states along t_2, as long as the coherence survives. An extensive explanation of the importance and behavior of coherences is reported in the next section.

Figure 10, adapted from [17],shows in more general terms the Feynman paths associated to each experimental configuration: rephasing, non-rephasing and 2Q2D. In the case of non-rephasing, the transformation of axes is the same of rephasing one. The difference is the phase matching conditions that select the R_1 (SE) and R_4 (GSB) Feynman paths instead of R_2 and R_3.

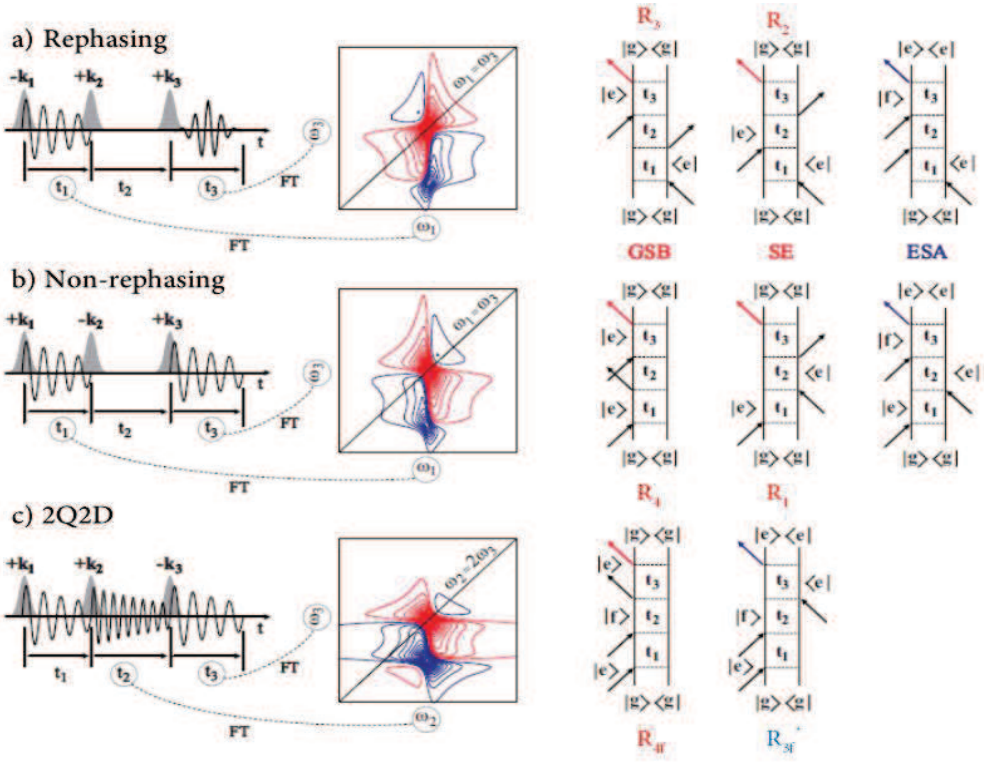

Figure 10. Building the 3rd order signal for all the experimental configurations. a) rephasing, b) non-rephasing and c) 2Q2D.

For what concerns the 2Q scheme, only two Feynman diagrams contribute to the spectrum. The double quantum signal is relevant only when the system has a state at energy twice the laser energy. This could

be the case of systems with double excitation allowed, such as quantum dots, aggregates and so on. This experiment intends to investigate the coherence between the ground and the doubly excited state possibly evolving during t_2.

$$S_{2Q}(t_1, t_2, t_3) \rightarrow S_{2Q}(t_1, \omega_2, \omega_3) \tag{45}$$

Since in this particular scheme, in none of the three time intervals there is a pure state evolving, it is possible and convenient to fix $t_1 = 0$. The double quantum signal is then meaningful when represented by a map depending on ω_2 and ω_3 [17].

1.5.1 Vibrational and electronic coherences

In rephasing and non-rephasing signals, it is expected to find many oscillations along t_2. In principle, all states that can be excited simultaneously by the first two laser interactions generate coherences and thus oscillations along t_2. Practically, a femtosecond laser pulse used for 2D spectroscopy could have a spectral bandwidth in the order of thousands of cm^{-1}. This means that several electronic transitions could be excited simultaneously. Moreover, working with organic dyes, the first two laser pulses can promote coherences between all the vibrational states coupled with the electronic transitions. In fact, vibrational transitions of organic dyes typically have frequencies in the range 400-3000 cm^{-1}. In particular, vibrational transitions at about 1400 cm^{-1} due to stretching C=C are often strongly coupled to electronic transitions[11].

All possible vibrational and electronic coherences thus generate a complex oscillating pattern along t_2. This makes the analysis of oscillations very complex. With the aim of making the interpretation of signal clearer, it is convenient to perform a preliminary analysis of the Feynman paths involved, preferably knowing the states of the system.

As example, below we treat two simplified systems representative of common real cases: (i) the case of one vibration coupled with both the excited and the ground state; (ii) the case of the coherence between two electronic states.

The first case is well described by Turner[18]. In figure 11, only Feynman diagrams contributing to oscillations along t_2 in the rephasing and non-rephasing case are illustrated. In these examples, all ESA contributions are neglected even though they could be relevant if states at higher energy are present. It is possible to notice that in the rephasing map the oscillations are expected along coordinates distributed in a "chair-like" manner. Non-rephasing maps differ only for one point. In the rephrasing map there are oscillations in the point with coordinate (ω+ν ; ω-ν) and no oscillations in the point (ω+ν ; ω+ν); the opposite for the non-rephasing map. In general, if more than one vibration is coupled with the electronic transition, it generates oscillations with frequency ν_x at coordinates $\omega \pm \nu_x$. Moreover, this example neglects the case in which the vibrations at the electronic ground state are populated before the first perturbation. This is always true if the vibration has energy higher than k_BT (≈200 cm^{-1} at room temperature). However, if the vibrational frequency is in the order of k_BT, we have to take into account also Feynman paths starting from $|g_1\rangle\langle g_1|$, giving rise to oscillations also at positions with the exciting frequency equal to ω-ν.

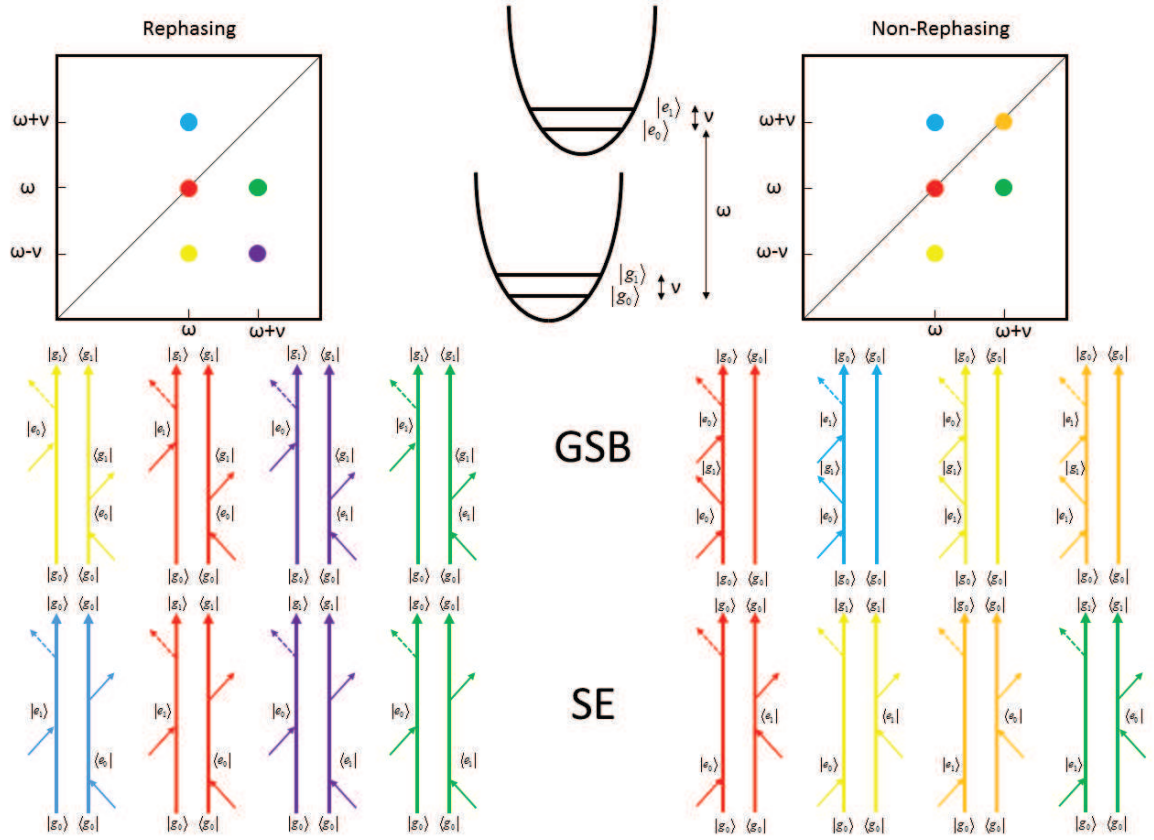

Figure 11 The positions in rephasing (left) and non-rephasing (right) maps of the oscillating vibrational coherences represented by the correspondent GSB and SE Feynman paths. The vibration is coupled equally with both the ground and the excited states as shown by the schematic model.

A different scheme is generated when the coherence evolving along t_2 is due to the superposition of two electronic states instead than vibrational states. The following example shows the case of a homodimer, described by two excitonic states, α and β, but it is valid for any pair of coupled electronic states excited simultaneously by the laser. Differently from the previous case, here there is a great difference between rephasing and non-rephasing maps. In fact, in the rephasing map we have oscillations with frequency ω_β-ω_α at off-diagonal positions. On contrary, in the non-rephasing map the coherence oscillates at diagonal positions. This characteristic is fundamental to recognize electronic coherences and distinguish them from the vibrational ones.

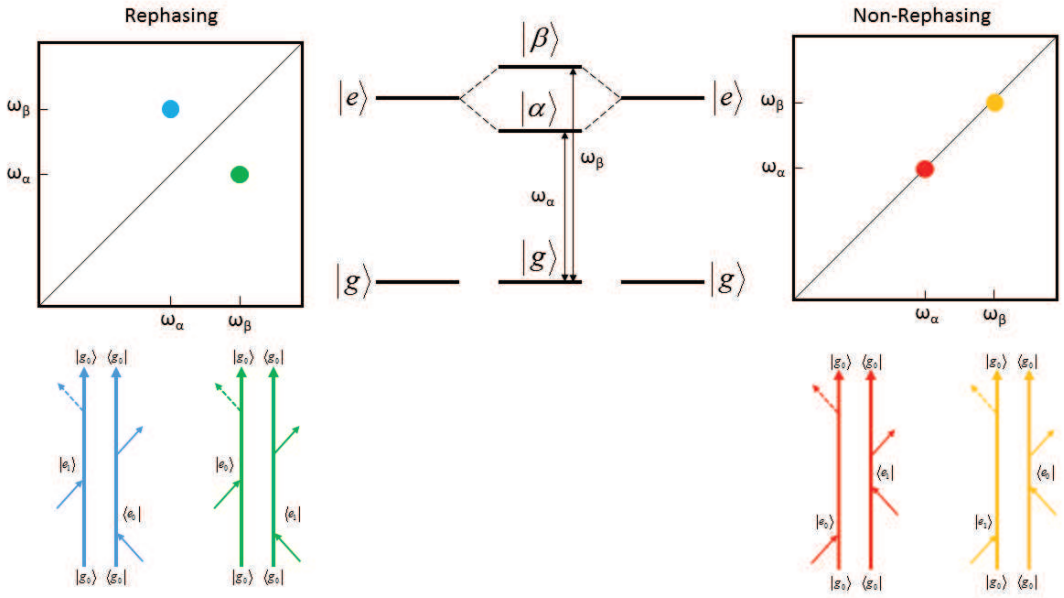

Figure 12 The positions in rephasing (left) and non-rephasing (right) maps of the oscillating electronic coherences represented by SE Feynman paths. The model used is a homodymer system (see section 1.5).

The dephasing of electronic coherences is strongly dependent on temperature. At room temperature they typically last for tens of fs, depending on the linewidth of the transitions and thus on the coupling with environment and vibrations. On the other hand, vibrational coherences last longer than electronic coherences and they can survive for picoseconds. This is because vibrational wavefunctions and energies are much less influenced by inhomogeneity and fluctuation with respect to electronic ones.

Besides these two limit examples, vibrations and electronic transitions may be coupled and give rise to situations characterized by oscillation schemes intermediate between the one of Figure 11 and 12. Indeed, recent theoretical models seem to demonstrate that the coupling between vibrational frequencies and electronic transitions may explain the extraordinary long-lived coherences experimentally detected [19], [6].

1.6 CHIRALITY

Besides the optical properties related to the dipole moment treated until now, there are other minor effects that are actually more sensitive to excited state properties. In previous sections, we assumed that the perturbation was simply the interaction between the electric field and the dipole moment:

$$\mathcal{H}'(t) = -E(t)\tilde{\mu} \tag{46}$$

This approximation is generally valid since the dipolar interaction is the greatest effect [11]. However, in some case, the symmetry of the wavefunctions involved in the transition cancel out this interaction, but the transition is still measurable. The absorption in these cases may result from quadrupole, octupole, or higher order terms previously neglected in using the dipole operator. In other cases, it can be traced to interactions with the magnetic component of the field B(t). In addition, coupled interactions involving both the electric E(t) and magnetic B(t) component can cause the dipole strength of a transition to be different for left- and right-circularly polarized light. This is the definition of circular dichroism (CD). The listed effects are order of magnitude less intense with respect to the dipole interaction but they can be very informative of the system.

To treat the effects of the magnetic component, it is necessary to include the time dependent magnetic field in the Hamiltonian of the perturbation.

$$\mathcal{H}'(t) = -E(t)\tilde{\mu} - B(t)\tilde{m} \tag{47}$$

$$\tilde{m} = \frac{e}{2m_e c}(r \times \tilde{p} + g_e S) \tag{48}$$

where e and m_e are the electron charge and mass, c is the speed of light, r is the position of the electron, $\tilde{p}$ is the linear momentum operator, g_e is the electron g-factor (2.00232), S is the angular momentum associated with the electron spin [11].

CD is related to the rotational strength $\mathfrak{R}_{ba}$ of the transition. For example, if light induces a transition from state *a* to *b,* the rotational strength could be calculated by the Rosenfeld equation [20]:

$$\mathfrak{R}_{ba} = -Im\langle e|\tilde{m}|g\rangle \cdot \langle e|\tilde{\mu}|g\rangle = -Im(\boldsymbol{m_{eg}} \cdot \boldsymbol{\mu_{eg}}) \tag{49}$$

The rotational strength is 0 when electric and magnetic transitions are perpendicular. This is the case for most of non chiral molecules. For example a planar molecule must have the electric dipole moment on the molecular plane while the magnetic perpendicular to it. However, if the molecule or the molecular assembly is chiral, they are no more perpendicular.

Here, the effect of this interaction on simple chiral molecule is skipped [21], focusing the attention on CD of multichromophoric systems. To this aim, it is necessary to introduce the concept of exciton in molecular systems. When two or more molecules are close enough and their dipole moments are non-perpendicular, the optical properties of the whole system cannot be simply described by the sum of their properties [11]. In particular, for the case of a homodimer, the interaction between two molecules generates new excitonic transitions expressed as the combination of monomeric transitions. If each monomer is described by states *g* and *e,* in the dimer new excitonic states α and β will be generated (figure 13, panel a). Excitons are the bases for the description of excitation migration in multichromophoric systems.

The rotational strength in this case includes 3 terms

$$\mathfrak{R}_{mon} = -\left(\frac{1}{2}\right) Im\left(m_{eg(1)} \cdot \mu_{eg(1)} + m_{eg(1)} \cdot \mu_{eg(1)}\right) \tag{50}$$

$$\mathfrak{R}_{e-m} = \pm\left(\frac{1}{2}\right) Im(m_{eg(1)} \cdot \mu_{eg(2)} + m_{eg(2)} \cdot \mu_{eg(1)}) \tag{51}$$

$$\mathfrak{R}_{ex} = \pm\left(\frac{\pi}{2\lambda_{eg}}\right)(R_2 - R_1) \cdot \left(\mu_{eg(1)} \times \mu_{eg(2)}\right) \tag{52}$$

where λ_{eg} is the wavelength of the optical transition of the monomer and $(R_2 - R_1)$ is the distance between the two molecules. The last term dominates over the other two since it depends only on the

electric dipole moment transitions that are, as anticipated, much more intense with respect to the magnetic ones. Then equation 52 can be rewritten as

$$\Re_{ex} = \pm\left(\frac{\pi}{2\lambda_{eg}}\right)|R_{21}| \cdot D_{eg} sin\theta cos\varphi \tag{53}$$

where $|R_{21}|$ is the distance between centers of the two molecules, D_{eg} is the dipole strength of the monomer and θ and φ are the angles between the electric and magnetic dipole moments. This term generates two bands of opposite sign in the CD spectrum, centered on the energy of the new excitonic states. Figure 13 panel b, reports the comparison between the absorption spectrum of the monomer, and the absorption and CD spectrum of the dimer. It is easily noticeable that the excitonic coupling is much more recognizable in the CD spectrum than in the absorption spectrum that remains very similar to the monomer's one.

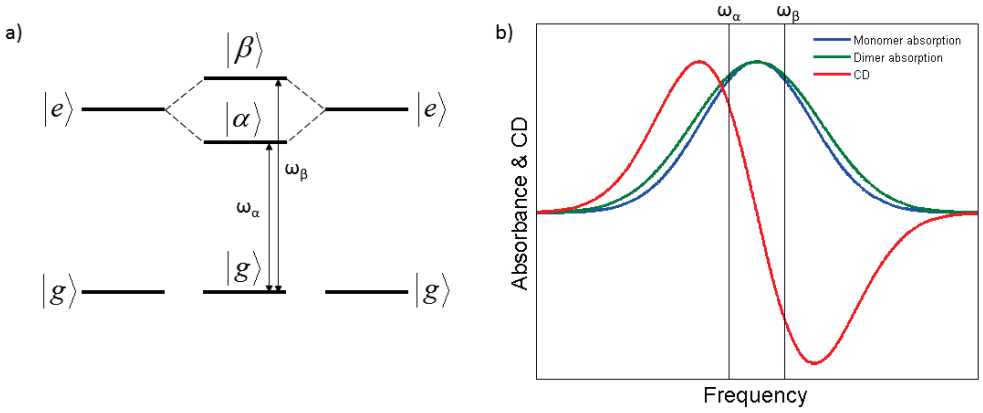

Figure 13 The model for excitonic interaction in a homodimer a) with the corresponding absorption and CD spectra b).

Moreover, following equation 53, CD spectrum can provide information not only about excitonic coupling but also about dipole strength, distance between the molecules and especially about angles between the dipoles. It is then informative about the geometry and the conformation of the multichromophoric system.

2 EXPERIMENTAL TECHNIQUES

2.1 STANDARD SPECTROSCOPIC METHODS

Spectroscopy is the study of the interaction between electromagnetic radiation and matter. The aim of spectroscopy is to discover the properties of a selected material or molecule through their response when perturbed by electromagnetic radiation.

The investigation of each optical property requires an appropriate optical setup. Absorption spectroscopy, as well as emission and circular dichroism spectroscopies, are nowadays based on standard and commercial instrumentation. On the contrary, advanced ultrafast spectroscopies needs specific homemade setups.

2.1.1 Linear absorption and emission

The most common and frequently used optical spectroscopy is the absorption spectroscopy. It is a linear spectroscopy that measures the intensity of light absorbed by a sample. It scans a range of wavelengths, selected by a monochromator, providing for each one the absorbance, defined as minus the logarithm of the ratio between the intensity of the light before and after the sample [11]:

$$A(\omega) = -\log\left(\frac{I(\omega)}{I_0(\omega)}\right) = \varepsilon(\omega) l C \tag{54}$$

where I and I_0 are the intensity of light detected with or without the sample. The absorbance is linearly related to the optical path l and the concentration of the sample C through the molecular extinction coefficient $\varepsilon(\omega)$. Absorption spectroscopy is useful for identifying the nature of the samples, determining at which wavelengths they absorb and to have a control on sample concentration. In our lab, we made use of a Varian Cary 5 spectrometer.

Another standard spectroscopy is emission spectroscopy. It measures the intensity of light emitted by a sample when excited. It can measure both emission spectra, when wavelength of excitation is fixed

and the wavelength of emitted light is scanned, and excitation spectra, when the wavelength of excitation is scanned. This spectroscopy is useful to study, for example, excited states emission and energy transfer yield. Furthermore, in some cases it can replace absorption spectroscopy when more sensitivity is necessary. The instrument used in this thesis is a FluoroMax by Jobin Yvon.

2.1.2 Time-resolved fluorescence

To study deeper the excited state, it is possible to measure the fluorescence lifetime following the decay of the intensity of fluorescence after the excitation of the sample. This can be done exciting the sample with a pulsed light source, such as a laser or a pulsed nanoled, and following the intensity of the fluorescence with an ultrafast photodiode. However, one of the most diffused and informative methods to measure fluorescence lifetimes is based on single photon counting technology (TCSPC) [22]–[25]. In our lab, there are two TCSPC setups with two different time resolutions. The first is an optional of the FluoroMax, where excitation lamp and detector are replaced by a pulsed nanoled source and a single-photon detector, respectively. This apparatus has a resolution of about 1.5 ns and can measures decays up to ms time range. In the second setup, the sample is excited by a frequency-doubled femtosecond Ti:Sapphire laser (exc=370-490 nm) and the detection is performed through an avalanche photodiode. In this case a time resolution of about 150 ps can be reached but only 12.5 ns after photoexcitation can be investigated.

2.1.3 Circular dichroism

Circular dichroism spectroscopy is a little more complicated than linear absorption because CD signal, as anticipated in Chapter 1, is 3-4 orders of magnitude less intense than the absorption signal. To measure it, the light of a lamp is alternately prepared to be left- and right- circular polarized by means of a Pockels cell. This modulation is made at a specific frequency so that a lock-in amplifier linked to the photomultiplier tube can detect only the differential CD effect. In our labs, CD spectra were measured with a Jasco J-710.

2.1.4 Pump-probe

Pump Probe spectroscopy has been the main tool to study third order nonlinear signals since the invention of ultrafast lasers. Although 'closed-box' commercial instruments are now available, home-made setups are necessary to achieve specific performances.

A pump-probe experiment is based on the measurement of the variations of the intensity of a probe pulse passing through a sample when excited or not by an ultrafast laser pulse. The variation of intensity is then converted into differential absorbance ΔA, whose dependence on the frequency of the probe (ω) provides the so-called transient absorption spectra:

$$\Delta A(\omega) = -\log \frac{I_{Pumped}(\omega)}{I_{Unpumped}(\omega)} \tag{55}$$

These transient absorption spectra are collected at increasing time delay between the pump and the probe obtaining a matrix dependent on frequency and delay: $\Delta A(\omega, t_{delay})$. ΔA is proportional to the third order signal, in which pump pulse provides the first two dipole interactions. Precisely because of this, pump probe does not allow reducing the number of relevant Feynman paths as for 2DES. However, in past decades many progresses were made for the analysis of the decay of the pump probe signal [26], making it a useful tool for excited states dynamics studies. Pump-probe setups are very versatile instruments, and different versions and improvements of pump probe are found in literature [27][28], [29]. Our laboratories are equipped with a homemade pump probe setup described in figure 14. The pump probe setup was also used as a base for the time resolved circular dichroism set up described in the next section.

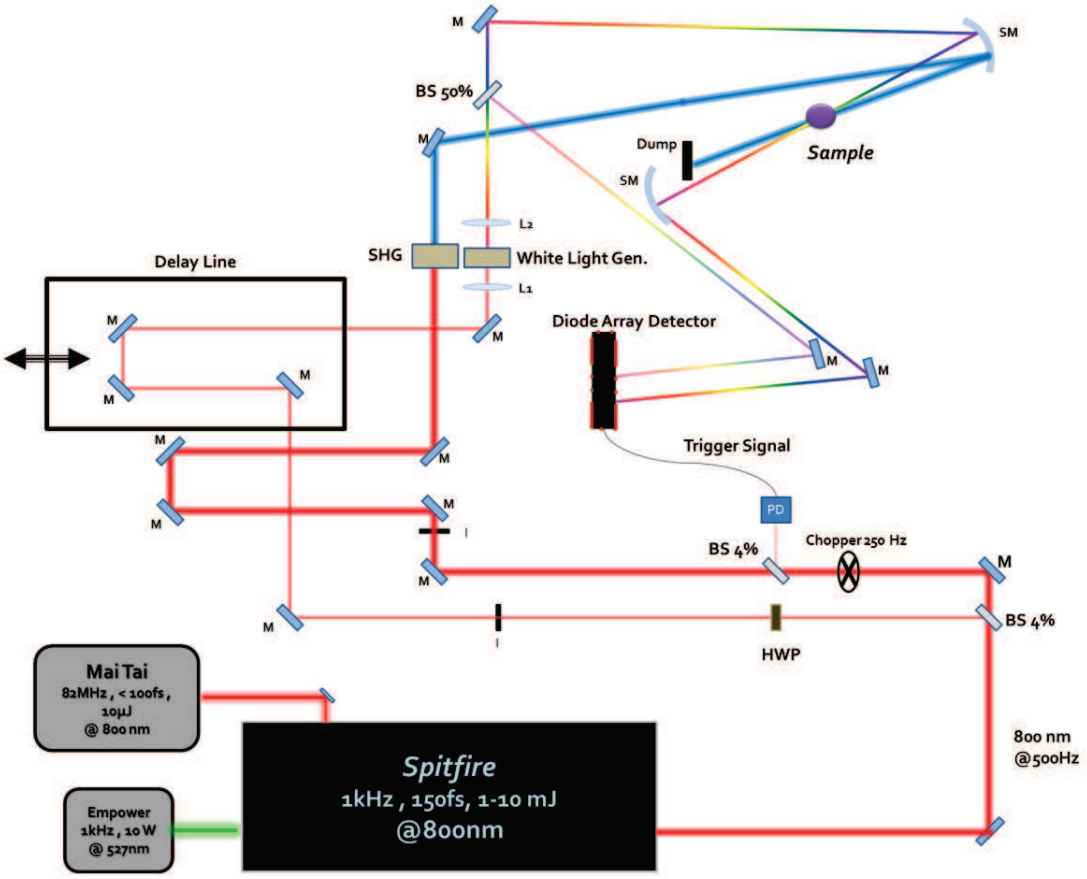

Figure 14 Pump probe setup built in our lab. A Ti:sapphire amplified laser system (Spitfire) generates a pulse train of highly energetic pulses (800nm, 0.8mJ per pulse, 150 fs time durationa, 1 KHz repetition rate). The output beam is splitted in two beams, used prepare a pump and a probe beam. Pump beam repetition rate is halved to 500 Hz, by means of a chopper, and its frequency is doubled to 400nm by means of second harmonic generation (SHG). On the other side, probe beam pulses are converted to white light pulses exploiting super-continuum white light generation (SWLG) in a sapphire crystal. The two beams are aligned to spatially overlap exactly on the sample. Time delay between the two pulses is controlled by a retroreflector mounted on a translation stage. White light transmission spectrum is recorded by means of a detector composed of a diffractive grating and a CCD diode array.The difference between transmittance spectrum with and without pump constitutes the final transient absorption spectrum.

2.2 TIME RESOLVED CIRCULAR DICHROISM

In section 1.6, we analyzed the reasons why circular dichroism effects are such a powerful tool for studying excited states of multichromophoric systems. In particular, the ability to be sensitive to geometry and conformation changes makes them particularly attractive for spectroscopists. In particular, achieving a time resolved version of CD (TRCD) would open to new possibilities in the study of excited state because it could be informative of conformational and geometrical changes triggered by photoexcitation. As example of the potential ability of this technique, let's consider again the case of the homodimer shown in figure 13 of Chapter 1. The system is formed by the ground state and two excitonic states α and β. A non-polarized spectroscopy such as pump probe can follow in time the relaxation of the excitation from β to the lower excited state α and then to the ground state *g*. However, it is completely blind to any geometrical change happening when excitation is present. If during the excitation the angle between the directions of the two dipole moments changes, it would be visible only by a transient CD spectrum. This technique becomes fundamental since dynamical geometrical changes could influence excited state dynamics and in particular energy transfer. Energy transfer process is related to the dipole-dipole interaction that is strongly dependent on the angle between the two dipoles [3]. Moreover, recent theoretical models affirm that conformational oscillations could activate coherences between electronic states helping quantum coherent energy transfer processes [19].

The aim of TRCD is to measure the difference of the CD signal (ΔCD) of a sample when excited or not by a pump pulse. It makes use of two laser pulses, one acting as a pump and the other as probe. Effectively, it is analogous of ΔA in the conventional pump probe spectroscopy.

$$\Delta CD = CD_{pumped} - CD_{unpumped} \tag{56}$$

Our experimental approach is based on that proposed by Hache[30], who used a Babinet-Soleil compensator (BS) to measure difference in the ellipticity of the probe pulse. We also tried to improve it with a broadband detection. As for pump probe, ΔCD spectra are measured at increasing time delay between the pump and the probe to obtain a matrix of $\Delta CD(\omega, t)$ dependent on both frequency (or wavelength) and time delay.

To understand how it is possible to obtain the ΔCD signal, it is useful to analyze the polarization of the laser light at each step of the setup. To do this we treat the electric field of laser using Jones matrices. Jones matrices are useful because they can describe the retardation of the orthogonal component of the electric field of a coherent radiation. Each optical element has a corresponding matrix that acts on the electric field.

It is then possible to follow in figure 15 each step in the setup. Let us assume that the incident electric field is linearly polarized along x.

$$E_{in} = E_0 \begin{pmatrix} 1 \\ 0 \end{pmatrix} \tag{57}$$

Then it goes through the sample that, if chiral, acts on the field as described by the matrix:

$$M_{sample} = \begin{pmatrix} \cosh\left(\frac{\eta}{4} + i\frac{\delta}{2}\right) & -i\sinh\left(\frac{\eta}{4} + i\frac{\delta}{2}\right) \\ i\sinh\left(\frac{\eta}{4} + i\frac{\delta}{2}\right) & \cosh\left(\frac{\eta}{4} + i\frac{\delta}{2}\right) \end{pmatrix} \tag{58}$$

with circular dichroism $\eta = \Delta CD = (\alpha_L - \alpha_R)L$ and optical rotation (OR) $\delta = 2\pi\frac{n_L - n_R}{\lambda}L$ where α and n are the absorption coefficient and refractive index of left $_L$ and right $_R$ circular polarized light, respectively. L is the optical path.

To analyze the electric field out of the sample, a convenient method is to use BS coupled to a polarizer, called analyzer. The BS is oriented at 45° with respect to the x and y axes and its Jones matrix is

$$M_{BS} = \begin{pmatrix} \cos X & i\sin X \\ i\sin X & \cos X \end{pmatrix} \tag{59}$$

where 2X is defined as the retardation induced by the BS.

The analyzer is simply a linear polarizer and its Jones matrix depends on the angle ε between y and the axis of polarizer.

$$M_{Analiyzer} = \begin{pmatrix} sin^2\varepsilon & cos\varepsilon\, sin\varepsilon \\ cos\varepsilon\, sin\varepsilon & cos^2\varepsilon \end{pmatrix} \tag{60}$$

The electric field after all these polarization optics is then

$$E_{out} = M_{Analyzer} M_{BS} M_{sample} E_{in} \approx E_0 e^{-\alpha L/2} \begin{pmatrix} 0 \\ i\left(X + \frac{\eta}{4}\right) + \left(\varepsilon - \frac{\delta}{2}\right) \end{pmatrix} \tag{61}$$

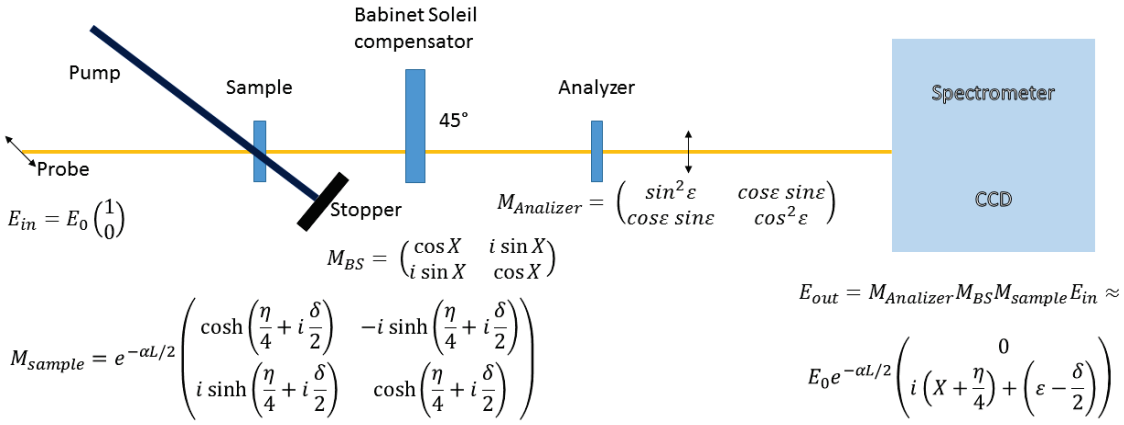

Figure 15 TRCD setup. It is based on the same setup for Pump Probe spectroscopy. Pump reaches the sample and is then stopped. Probe pulse passes through the sample and its ellipticity is measured by the babinet soleil compensator, placed with the main axis oriented at 45° with respect of the initial polarization of light, and a polarizer that allows passing only light polarized perpendicular with respect to the initial one. A Jones matrix can be associated at each step in the set up. It describes the effect induced on the polarization of laser light.

The final intensity for each wavelength can be then easily calculated:

$$I(\lambda) = e^{-\alpha(\lambda)L}\left[\left(X(\lambda) + \frac{\eta(\lambda)}{4}\right)^2 + \left(\varepsilon(\lambda) - \frac{\delta(\lambda)}{2}\right)^2\right] \tag{62}$$

This setup offers incredible capacities. We made use of a visible supercontinuum probe pulse and for each wavelength detected by the CCD, it is possible to measure both ORD and CD. In fact, it is sufficient to scan BS retardations or rotate the ε angle until a minimum of intensity is found. In our setup, ε is kept fixed since we are interested only in the absorptive part. Thus, to measure CD it is sufficient to

scan X retardation while measuring intensity with the CCD. This is done alternately for pumped and unpumped sample such as in pump probe spectroscopy. ΔCD is then proportional to the difference between the minima of the intensity of pumped and unpumped sample along the X retardation axis.

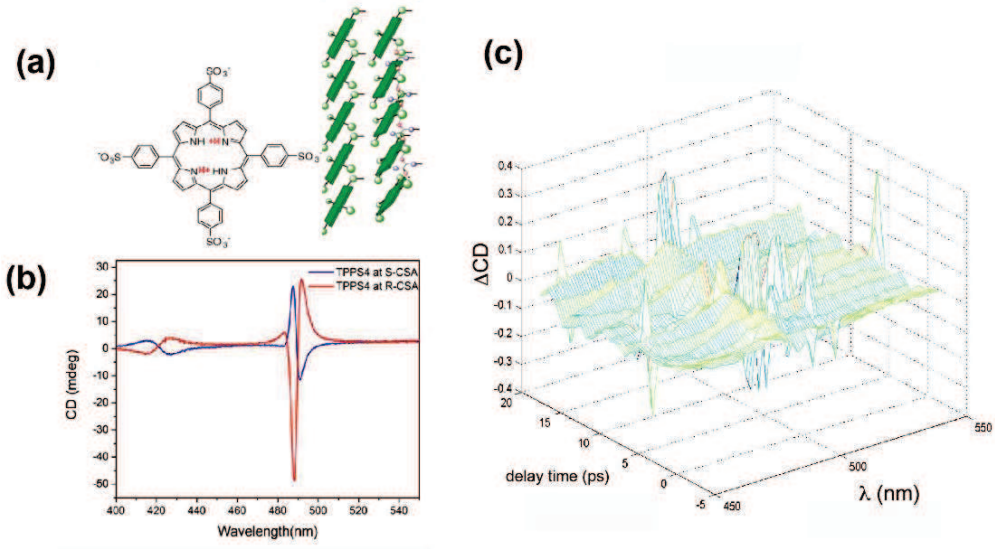

Figure 16 a) Structure and spatial arrangement of TPPS J-aggregates used as benchmark fro the new TRCD technique. b) CD spectra of the two samples prepared with R- and S-camphorsulforic acids. c) the first ΔCD matrix dependent on time and wavelength. Spectra have some features but no meaningful time behavior could be found.

However, results obtained with this setup were not encouraging. We tested our setup on TPPS aggregates prepared with acids with opposite chirality, R- and S-camphorsulforic acids. The structure and linear CD spectra of samples are shown in panels a and b of figure 16. The two samples had great CD signals. However, when TRCD measures were performed, the resulting transient spectra were very noisy (figure 16 panel c), not reproducible and it was not possible to follow any meaningful time dependence. A meaningful and correct time independent ΔCD spectrum comes out after very long measurement and the average of many dataset, but this make this setup useless for realistic experiments.

The construction of a working TRCD setup is a very challenging task, not yet fully achieved. There are very few experimental examples of working setups in literature, and in particular no one in the visible range (to our knowledge, the setup described in figure 15 is the only TRCD apparatus working in this spectral range). Thus, it was not possible to compare our results with others and find out new solutions to improve our experiment. Moreover, there are no samples exploitable as standard for the calibration

of ΔCD in the visible range. Chiral TPPS aggregate have been selected for their high CD signal but it was verified that having a great steady state CD signal does not necessary lead to a significant ΔCD signal. Currently we are collaborating with a theory group in UCL London, leaded by Prof. A. Olaya-Castro, who is simulating from the theoretical point of view the expected ΔCD signal for an excitonic dimer. We hope that the results of the simulations will help us identifying new experimental solutions to improve the sensitivity of our setup.

2.3 2DES SPECTROSCOPY

As stated in section 1.2, third order polarization is the most informative signal for excited state dynamics. 2D Electronic spectroscopy (2DES) is the ultimate spectroscopy to study third order signals. Differently from other third order techniques, 2DES can achieve the complete control of the times in which each interaction happens making it the most complete tool for third order nonlinear spectroscopy. However, the optical setup necessary for the measurements (figure 17) is much more complex than other third other spectroscopies such as pump and probe.

2DES is based on the interaction of three ultrafast laser pulses with a sample, usually a solution. The experiment consists in measuring the third order signal as a function of the time delays between pulses in order to obtain the third order polarization. In the following sections, each step necessary to the realization of the experiment is systematically described.

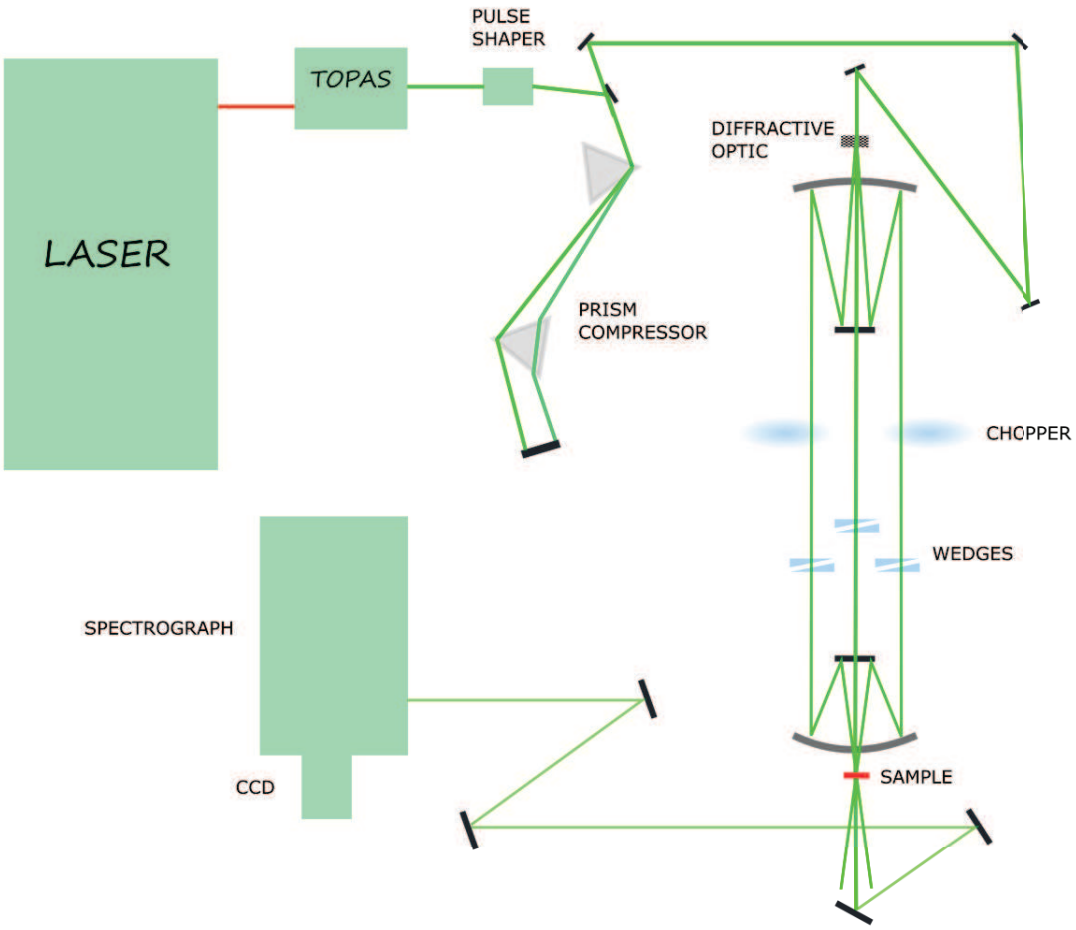

Figure 17 The 2DES schematic setup.

2.3.1 Laser source

Laser pulses used for 2D experiment are generated by a Coherent® Libra laser system. Libra is a one-box Ti:Sapphire based amplifier with integrated oscillator and pump lasers. A rough scheme of the laser system is shown in figure 18.

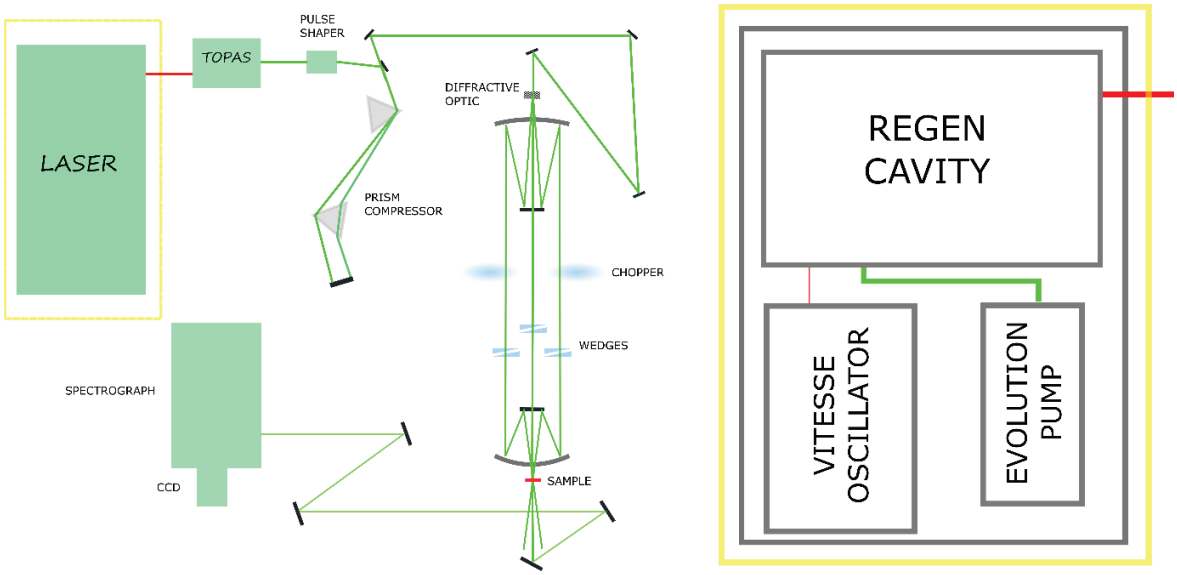

Figure 18 The 2DES schematic setup: detail of the laser sources. Laser source is an amplified Ti:Sapphire laser that generates a pulse train composed of 0.8 mJ pulses at 3 KHz and 800 nm.

The Vitesse oscillator produces NIR pulses at 800 nm with a pulse duration of 100 fs and a bandwidth of 12 nm. It is composed by a pump laser (Verdi) that pump a Ti:Sapphire crystal generating ≈3.5 nJ pulses with 80 MHz of repetition rate used as seed for the Regen cavity. In order to avoid damaging the Ti:Sapphire rod in the Regen cavity with high peak power, the seed pulses are stretched with a grating stretcher before injection. Population inversion in Ti:Sapphire crystal of the amplifier is provided by Evolution, a Q-Switched doubled Nd:YLF laser, which generates 527 nm pulses. Using Pockels Cells, the amplified pulse is extracted from the Regen cavity and sent to a grating compressor to restore the 100 fs pulse duration. Finally, the pulses exit the laser box with a repetition rate of 3 KHz and an energy of 0.8 mJ [31].

2.3.2 Non-collinear optical parametric amplifier

The pulses coming from the laser box enter an automated noncollinear optical parametric amplifier (Topas White, Light Conversion®). About 1% of the incoming 800 nm pulse is focalized on a sapphire plate to produce white-light continuum. The white light beam is collimated with spherical mirrors and then sent into a phase shaper consisting of a diffraction grating, a spherical mirror, a folding mirror and a phase mask. The phase shaper controls the chirp of the white light pulse such that the desired

bandwidth fits under the pump pulse in the nonlinear crystal. By controlling the chirp, it is possible to narrow or broaden the bandwidth of the final amplified pulse.

Then, the white light pulse reaches the nonlinear crystal together with a pre-amplification pump beam. Successively, the pre-amplified beam is overlapped within the same non-linear crystal with the main pump beam. Both pre-amplification and main pump beam come from the second-harmonic of the 800 nm laser pulse. After the power-amplifier stage, the beam is collimated using a mirror telescope and finally exits the Topas White without compression of the pulse. Additional home-made compression stages and optics to control the chirp are implemented in the 2D setup in order to obtain transform-limited pulses.

2.3.3 Controlling wavelength and phases of the pulse: FROG spectroscopy

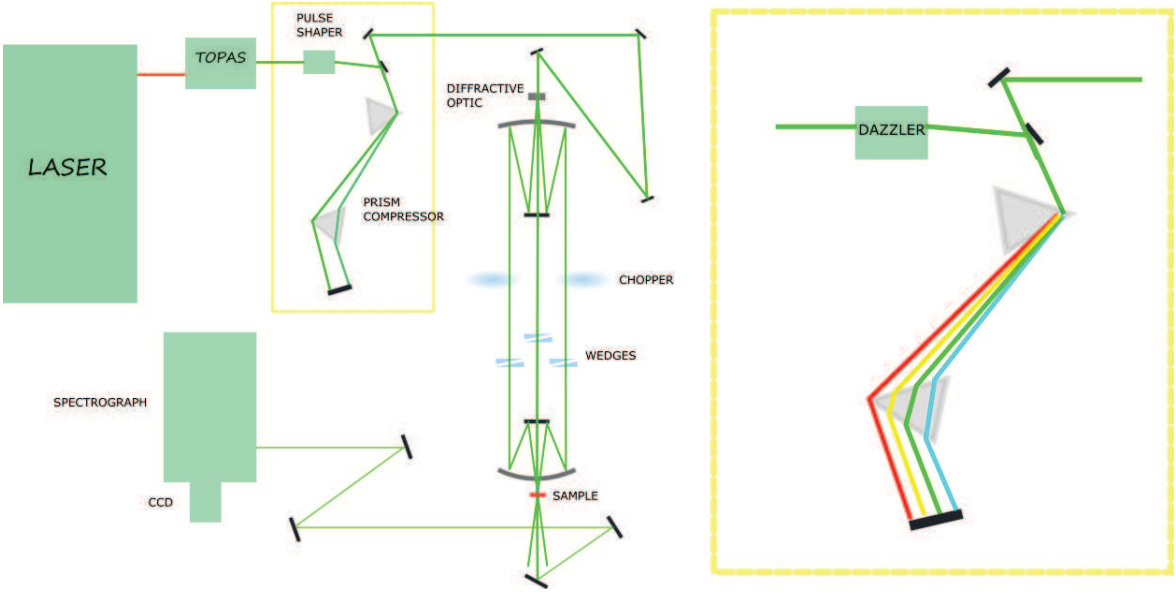

Figure 19 The 2DES schematic setup: detail of the compression stages. The output beam passes through the Dazzler pulse shaper, able to control phases of the each wavelength component in the pulse. For better performances, the pulse also passes through a prisms compressor to correct the linear chirp.

The time resolution of our experiment is directly related to pulse duration: the shorter the pulse, the better the resolution. The pulse duration is determined essentially by two factors: the bandwidth of the laser spectrum and the phases of its spectral components.

The width of the spectrum has a great influence deriving directly from the Heisenberg indeterminacy principle ($\Delta E^{*}\Delta t \geq \hbar/2$). The broader is the spectrum, the greater is the indeterminacy in the photon energy ΔE, and more information is obtained in the time domain.

For a given bandwidth, the shortest pulse possible is the pulse with all the wavelengths in phase: this is called transform-limited (TL) pulse. The electric field of the laser pulse can be expressed in the form:

$$E(\omega) = S(\omega) * e^{-i\omega_0 t + \varphi(\omega)} \tag{63}$$

where ω_0 is the center of the laser spectrum, $S(\omega)$ is the spectrum and $\varphi(\omega)$ the phase. A convenient way to express the frequency dependence of the phase is with an expansion of the phase around the center laser wavelength ω_0:

$$\varphi(\omega) = \varphi(\omega_0) + \frac{d\varphi}{d\omega}(\omega - \omega_0) + \frac{d^2\varphi}{d\omega^2}(\omega - \omega_0)^2 + \cdots \tag{64}$$

In fact, different orders describe different properties of the temporal profile of the pulse. The first order is simply related to the time arrival of the pulse. The second order describes the linear chirp, i.e. the linear drift of the phases of the frequency components present in the pulse. Odd and even higher orders describe respectively other asymmetric and symmetric phase distortions. TL pulse is achieved when second or higher order terms are zero.

When a broadband pulse passes through a transmissive optic, the different frequency components present in the pulse propagate with different speed in the medium and this lead to a chirped pulse that has longer time duration. This is because standard optical materials, like glass or fused silica, have the refractive index dependent on wavelength. Then, red light travels faster than the blue one when it passes through them. It is demonstrated that chirped pulses produce artifacts in 2D experiments[32] and thus it is crucial to be able to excite the sample with TL pulses.

To obtain a TL pulse at the sample position, it is necessary to have a complete control of the phase of each frequency component to correct all the possible distortions suffered by the pulse. This is achieved by two homemade stages: a prism compressor and a pulse shaper.

The prism compressor consists of a pair of transparent prisms and it is used to introduce a path-length difference for the red and blue spectral components of the laser pulse. Prisms are made of SF11, a material with a refractive index strongly wavelength dependent. Different wavelengths undergo different deflection angles in the first prism and therefore experience a different path length crossing the second prism. The chirp correction can be tuned adjusting the distance between the prisms. However, prism compression is useful to eliminate coarsely the linear chirp but it cannot correct easily the higher orders. This is because the correction depends directly on the wavelength dependence of the refractive index. For the same reason, prisms can even add higher order distortions to the pulse.

Therefore, prism compressor is helpful but a further control stage is necessary to achieve a fine-tuning and correction of phases. This is guaranteed by using an acousto-optic pulse shaper, called Dazzler.

The Dazzler provides a complete and easy control of the pulse phase[33]. The Dazzler is a small rectangular box (about 10x5x2 cm) containing a crystal and a piezoelectric device. The laser beam passes through the crystal and an acoustic wave, generated by the piezoelectric device, scatters each wavelength at a time controlled by the acoustic wave itself. The included software automatically generates an acoustic wave with a suitable form in order to impose the wanted phase at each frequency component in the pulse.

The measurement of the profile of the pulse is performed with the frequency resolved optical gating (FROG) technique [34]. FROG procedure reveals the frequency resolved autocorrelation of the pulse. In our case, it is possible to take advantage of the BOXCARS geometry (see next section) of our setup and perform FROG directly using the 2D setup replacing the sample with a non-zero third order material. Typically, a cuvette with a solvent such as CS_2 or DMSO is used. This guarantees to achieve identical properties of the pulse when both FROG and 2D measurement are performed. FROG works by scanning in time a pulse with respect to other two that arrive simultaneously and interact within the solvent. The third order signal is generated only when the all the three pulses are simultaneously present on the sample since solvent does not have transitions falling in the laser spectral range. Thanks to the

BOXCARS geometry, the third order signal generated propagates naturally along the same direction of the 2DES signal and can be collected by the CCD in the same detection geometry employed for the 2D setup.

In order to generate the best pulse, we adopt a procedure in which we iteratively modify the phase and we check the time duration of the pulse (figure 20) until the best conditions are found.

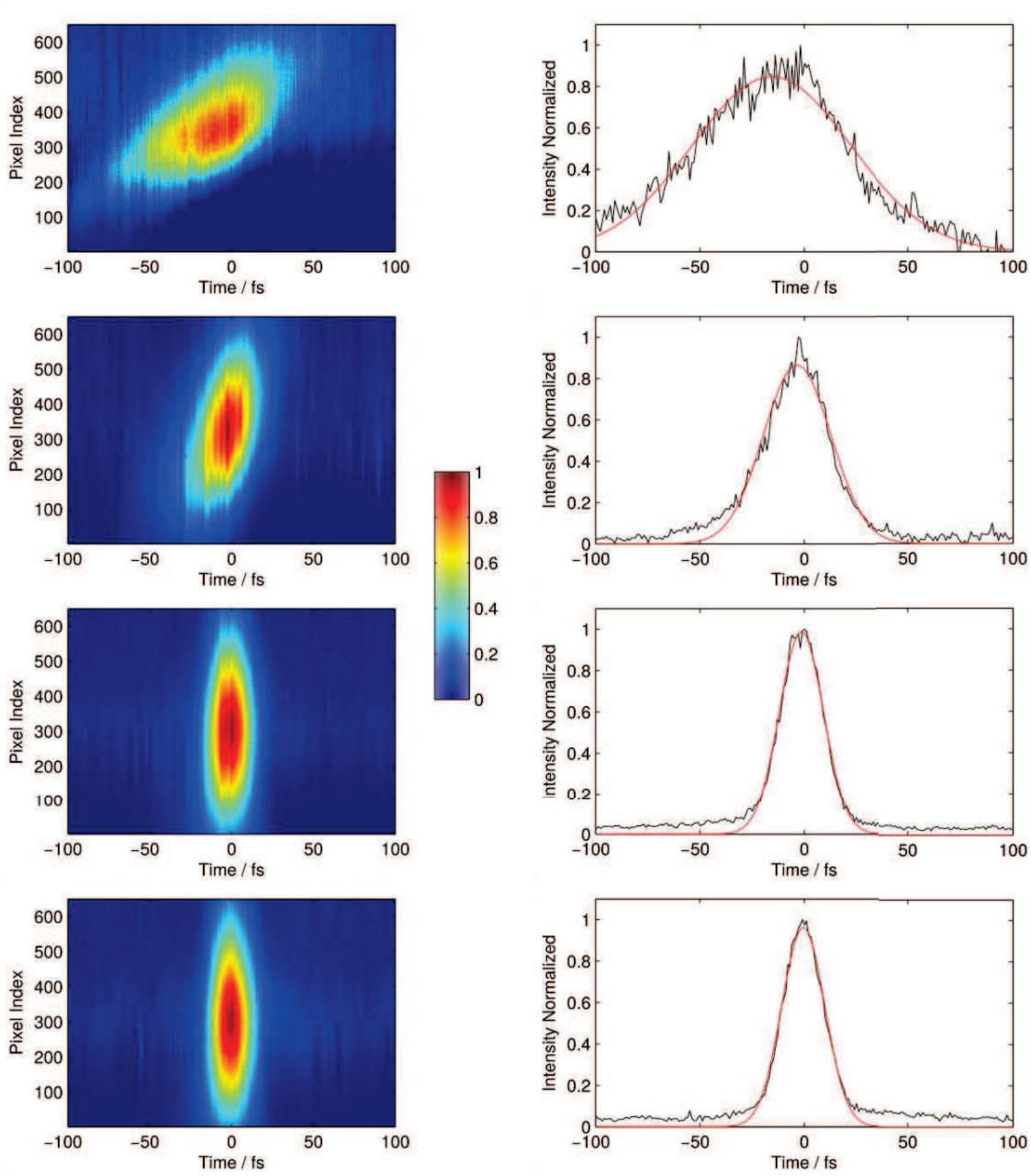

Figure 20. Optimization of the pulse with Dazzler Pulse shaper. On the left, FROG signals at increasing optimization level obtained by adjusting step by step the spectral phase with Dazzler. Graphics on the right are the correspondent integration over pixels and represent the temporal pulse duration.

2.3.4 BOXCARS geometry and Pulse's delay control

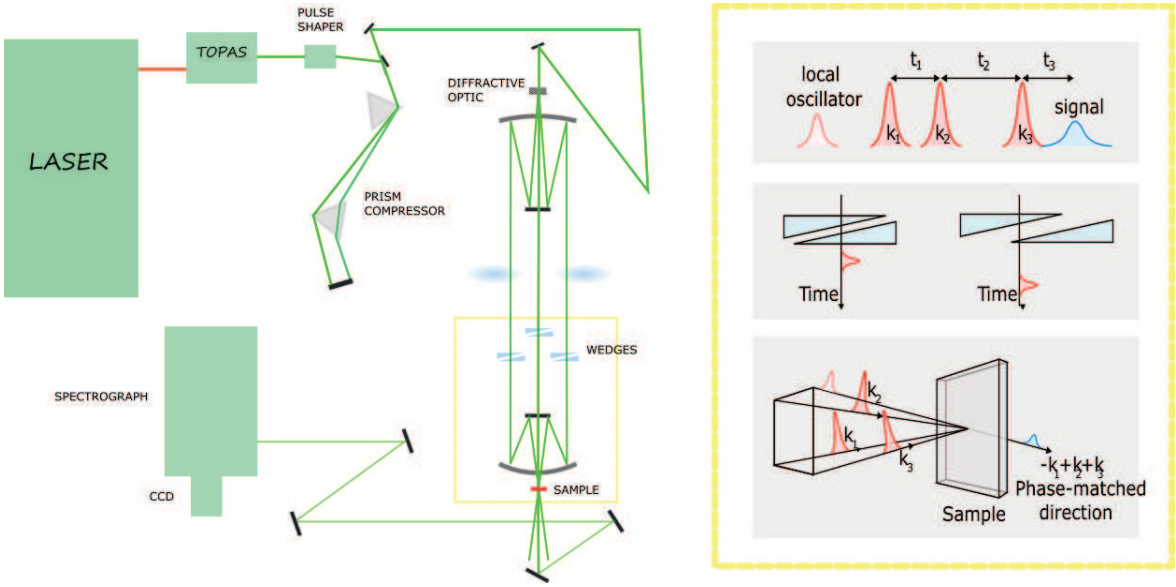

Figure 21 The 2DES schematic setup: detail of the phase matching geometry and pulse sequence control. Boxcars geometry is easily obtained by means of a diffractive optic and spherical mirrors. BOXCARS geometry guarantees that the desired third order signal is emitted in the same direction of the local oscillator. Time delay between pulses is achieved by moving a wedge with respect to the other, increasing or decreasing the path that the pulse travels in the glass.

2D measurements are based on the collection of third order signal. As explained in Chapter 1, only some contributions of the third order signal are desired. Phase Matching and time ordering of the pulses help selecting desired Feynman paths contributing to the signal.

BOXCARS geometry is an ideal geometry for a fully non collinear 2D setup. In this geometry, the three exciting pulses and a fourth pulse used for detection purposes, called Local Oscillator (LO), propagate parallel along the four vertices of a square and they are finally focalized on the sample (inset of figure 21).

All of the exciting beams possess a different wave vector (k_1,k_2,k_3) and the desired third order signal is generated in the direction of the fourth vertex following the same path of the LO that propagates in the same direction. Such square geometry is prepared using a diffractive optic that generates 4 identical replicas of the incoming beam. Inspired by the setup described by Nemeth et al.[35], appropriate optics are used to made the four beams to propagate collimated and parallel to each other before being

focalized at the sample position. Before reaching the sample, the LO is attenuated by a neutral density filter to made its intensity to be comparable to that of the third order signal.

Time delay between exciting pulses is generated and controlled by pairs of optical wedges (1°) inserted in each one of the three exciting pulses. One glass wedge from each pair is mounted onto a translation linear stage (Aerotech Ant95), which moves the wedge with respect to the other with nm accuracy adding or subtracting fused silica in the beam path. In this way the pulse is delayed without altering its direction (inset of figure 21). The time delay can be controlled with ~0.07 fs accuracy.

The geometry of our setup has several advantages with respect to other setups described in the literature [36], [37]. First of all, it has great long term and short term phase stability[35], absolutely necessary to obtain reliable 2D maps and to perform long experiments. Secondly, all the pulses walk almost the same path and traverse the same optics, leading to four identical pulses in the sample position. Finally, this geometry allows easily performing rephasing ($-k_1+k_2+k_3$), non-rephasing ($+k_1-k_2+k_3$) and double quantum ($+k_1+k_2-k_3$) experiments simply by changing the time ordering of the pulses.

2.3.5 Signal detection

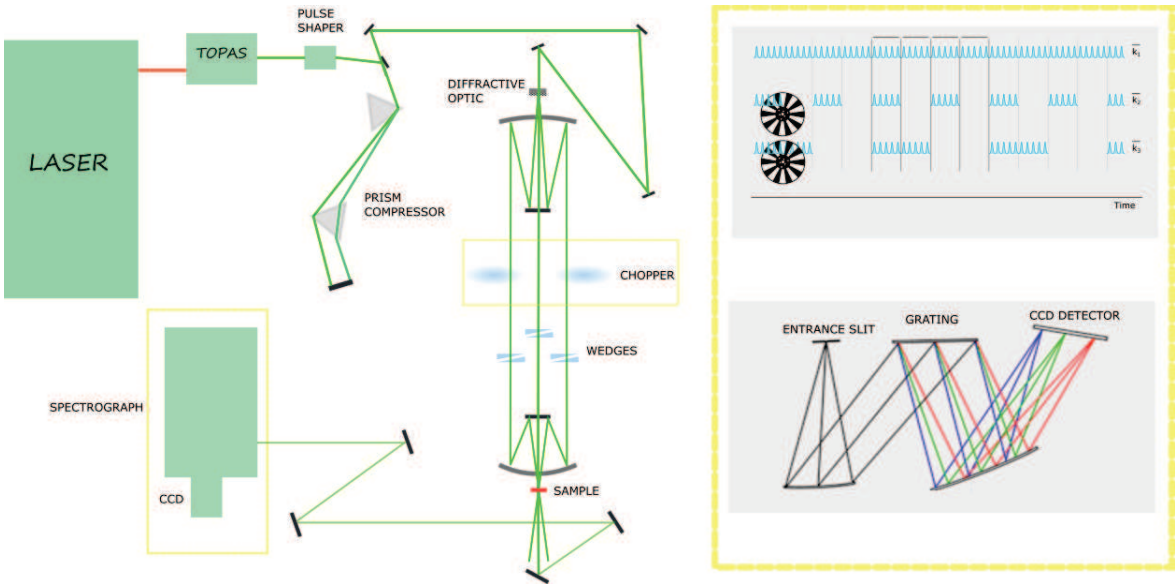

Figure 22 The 2DES schematic setup: detail of the detection apparatus. Signal-to-noise ratio in the detector is improved by the double modulation technique, obtained by chopping two excitation beams with two optical choppers. The third order signal is generated only when all excitation beams reach the sample, thus at frequencyes that are combinations of the two modulations. Signal is collected by a Czerny-Turner spectrograph that focalize different wavelength on a CCD detector.

The detection of the third order signal is a fundamental step to obtain meaningful 2D maps. A CCD (Andor Newton) coupled with a spectrograph (Andor Shamrock) is able to acquire spectra of the third order signal for each time delay between the interacting pulses, $S(t_1,t_2,\omega_3)$. CCD can only detect the intensity of the signal at different frequencies ($I_s(\omega_3)$) corresponding to the squared modulus of the electric field of the signal:

$$I_S = |E_s|^2 \tag{65}$$

The direct collection of the intensity of the third order signal is called homodyne detection. This detection scheme is not convenient in 2D setups, where heterodyne detection is instead used.

Heterodyne detection consists in acquiring the interference between the signal and an additional pulse, called Local Oscillator (LO) propagating in the same direction:

$$I_{S,LO} = |E_s + E_{LO}|^2 = |E_s|^2 + |E_{LO}|^2 + E_s{}^* E_{LO} + E_{LO}{}^* E_s \quad (66)$$

Heterodyne detection has two main advantages: (i) it guarantees a linear (instead than a quadratic) dependence of the recorded intensity on the signal field. This allows achieving a better signal-to-noise ratio; (ii) the complex electric field of the signal (S) can be retrieved. The complex electric field can then be separated into real (absorptive) and imaginary (dispersive) parts knowing the phase between LO and S. This 'phasing' procedure is explained later in Section 2.3.6.

To exploit the full potential of the heterodyne detection, LO is required to have an intensity similar to that of S and to propagate perfectly along the same direction. The BOXCARS geometry and a variable neutral density filter on the LO path provide the observance of these requirements.

The main disadvantage of heterodyne detection is the presence in the signal collected by the CCD of several unwanted contributions. The homodyne signal $|E_s|^2$ and the LO spectrum $|E_{LO}|^2$ need to be removed. Moreover, especially in highly scattering samples, also the contribution of scattered exciting pulses in the LO/S direction has to be removed. The complete set of contributions collected by the CCD is described by:

$$I_{CCD} = |E_1 + E_2 + E_3 + E_{LO} + E_S|^2 = E_1 E_1^* + E_1 E_2^* + E_1 E_3^* \ldots \quad (67)$$

and it is essentially the sum of the intensity of each pulse contribution in the CCD direction and all the interference terms between them.

Several methods can be used to remove the unwanted contributions, like time filtering and subtraction methods. Time filtering is applied after data collection. It can remove the interference between pulses when their time delays differ from the delay between S and LO and it will be described in details in the data analysis section (Section 2.3.6). The easiest and simplest method to remove most contributions directly during the signal acquisition is to use an automated shutter that alternatively blocks and unblocks the k_3 pulse. When k_3 beam path is blocked, the signal acquired by the CCD is

$$I_{CCD} = |E_1 + E_2 + E_{LO}|^2 = E_1 E_1^* + E_1 E_2^* + E_1 E_{LO}^* \ldots \quad (68)$$

and can be subtracted from the complete signal acquired with k_3 beam path unblocked (equation 67).

In the table 1, all contributions to the signal are illustrated, where the diagonal boxes represent the intensity of each signal pulse, while off diagonal boxes show the interferences between pairs of pulses. The main contribution is usually the intensity of LO that is removed in the subtraction.

Table 1. In red the contributions removed by the immediate subtraction of signal with k_3 beam path blocked, in green the desired contributions, in blue the components that cannot be removed with this procedure but that can be removed by subsequent time filtering.

	k_1	k_2	k_3	LO	S
k_1					
k_2					
k_3					
LO					
S					

The table shows that some of the unwanted contributions cannot be fully removed with this procedure (blue boxes) and thus further operations are needed. Moreover, subsequent acquisitions of spectra cannot remove laser intensity noise.

To solve this problem, Zigmantas proposed a "digital" double lock-in amplification for acquiring 2D spectra[38]. The lock-in amplification uses a modulation of the signal to remove all the non-modulated noise. The goal is to modulate the excitations in order to get only the signal at a specific combination of the modulated frequencies (inset in figure 22).

Our laser system works at a repetition rate of 3 KHz, so 3000 pulses reach the sample and the CCD per each second. The maximum operating frequency (f_{read}) of the CCD is about 1 KHz and it operates so it is simultaneously and continuously exposed and read, avoiding loss of pulses. In working conditions, the CCD generates a flow of 1000 spectra per second. The harmonic modulation is performed by two optical choppers positioned in the paths of pulse 1 and 3 (k_1 and k_3). These choppers modulate the two beams with different frequencies, set to be slower than $f_{read}/2$, that is the Nyquist limit. In our case,

frequencies are set at 400 Hz (f_{mod1}) and 100 Hz (f_{mod2}). When the CCD acquires, it continuously produces an endless series of spectra (intensity of 1024 CCD pixels) modulated by the frequency of the two modulating choppers. The interference between the third order signal and LO (when all laser pulses reach the sample) appears at frequency $f_{mod1} + f_{mod2}$ and $f_{mod1} - f_{mod2}$, so at 500 and 300 Hz.

Table 2. The frequencies of the contributions read by the CCD are represented in different colors. The method of acquisition allows extracting only the contributions at 300 Hz or 500 Hz (green), while 400 Hz (red), 100 Hz (yellow) and non-modulated (blue) contributions are removed.

	k_1	k_2	k_3	LO	S
k_1					
k_2					
k_3					
LO					
S					

The signal intensity for each pixel can be extracted by calculating the Fourier coefficients at a frequency that could be the sum or the difference of the two modulating frequencies.

$$I = Re\left(\sum_k N_k * e^{2\pi i * \frac{(f_{mod1} \pm f_{mod2})}{f_{read}} t + i\varphi}\right) \tag{69}$$

Here t is the time axis (index of consecutive spectra), N_k is the array of intensities detected by pixels of the CCD and φ is the phase offset between the signal modulation and the readout. From the practical point of view, we simply record a set of spectra, which range from 1000 to 2000 spectra for optimal results, and perform for each pixel the FFT along the time direction (t). Then, we extract the Fourier coefficient of, for example, the frequency 300 Hz ($f_{mod1} - f_{mod2}$) and reconstruct the spectra. Only the contributions that appear at 300 Hz are included in the coefficients' spectrum (green boxes in table 2). The remaining unwanted contributions could be easily removed via time filtering since the homodyne

signal $E_S E_S^*$ is intrinsically simultaneous and the time delay between k_1 and k_3 is always smaller than time delay between LO and the signal in our setup configuration.

In addition to noise suppression, the modulation technique virtually eliminates the contributions of slowly accumulating long-lived species due for example to thermal grating, long-lived triplet states or isomers, or permanent sample damage. This is achieved due to two effects – first, since only the relatively rapidly oscillating part of the signal (at the frequency f_{mod1} - f_{mod2}) is acquired, the amplitude of the oscillating signal component of slowly accumulating and slowly decaying species is significantly suppressed. Second, the signal is growing when the excitation is 'on' and decaying when the excitation is 'off', resulting in a phase shift between the excitation and the signal. As a result, the long-lived species produce mainly imaginary Fourier coefficients and, since we take only the real part of the coefficients, we remove also this contribution.

In figure 23, the double lock-in method is schematically elucidated.

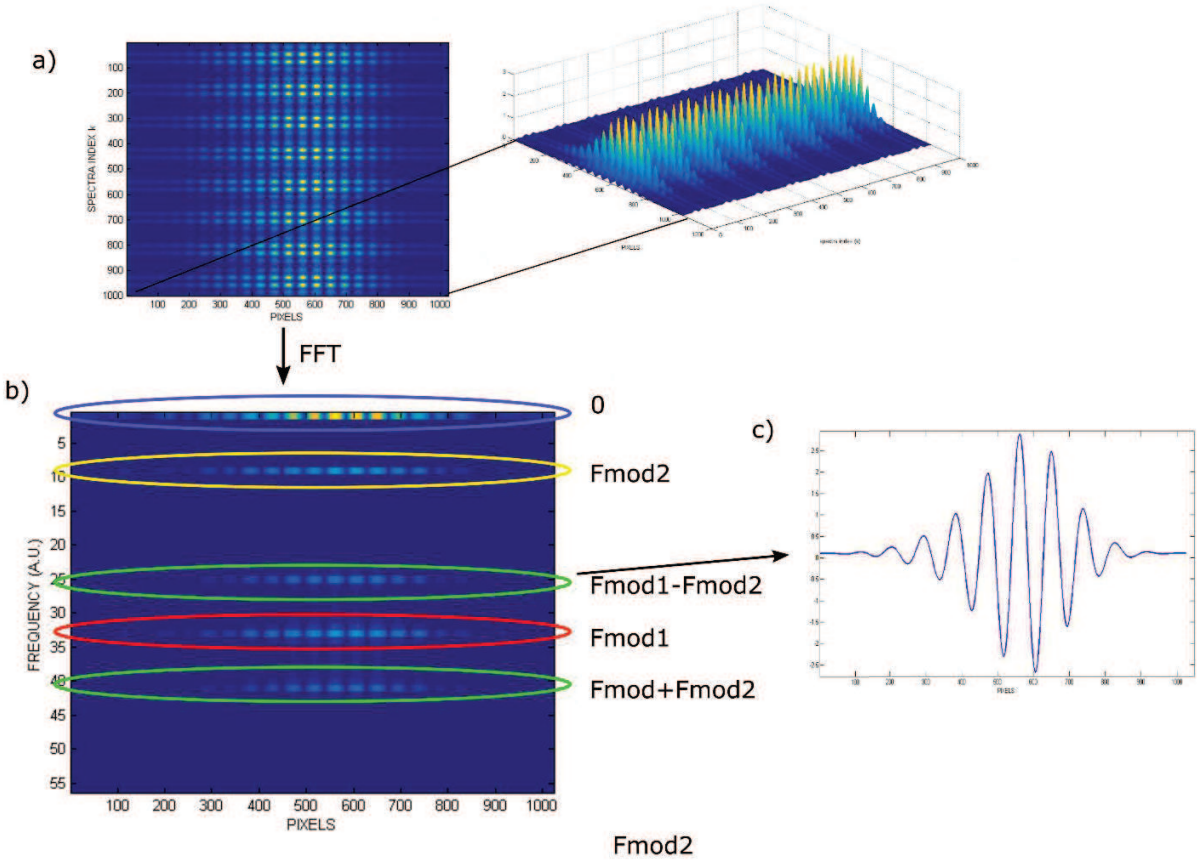

*Figure 23 a) Simulated experimental data matrix, where x axis values represent the pixels of the CCD while y axis is the index of consecutive spectra acquired. The two vertical modulations are clearly detectable in the 3d surface. b) the FFT along the spectra index of the data matrix (y axis). In this map, horizontal lines stand for the differently modulated contributions as shown in table 2. c) The extraction the real Fourier coefficients of the F_{mod1}-F_{mod2} contributions gives the final spectrum composed mainly by the desired contribution E_S*E_{LO}.*

A LabVIEW software manages the acquisition of all spectra at different time delays. In case of rephasing and non-rephasing spectra, it automatically saves a 3D matrix of the interference between the signal $S(t_1,t_2,\omega_3)$ and the LO.

2.3.6 Raw data analysis

It is necessary to retrieve the pure third order signal from the raw interference data. The procedure is shown schematically in figure 24. The signal collected by the CCD with the double lock-in acquisition explained above (green contributions) is in the form:

$$I_{CCD}(t_1, t_2, \omega_3) = I_S(t_1, t_2, \omega_3) + E_S(t_1, t_2, \omega_3)E_{LO}(\omega_3)^* e^{-i(\omega_3 t_{LO}+\varphi)} + c.c. \quad (70)$$

The aim is to isolate the third order signal, $E_s(t_1, t_2, \omega_3)$ from the total acquired signal. It is possible to remove all the residual scattering and homodyne contributions by a time filtering procedure. This is achieved through FT of the signal along ω_3 obtaining now a signal dependent on (t_1,t_2,t_3). At this point, only signal that is in a time delay close to t_S-t_{LO} is kept while all the rest is multiplied by 0. The clean signal can be re-obtained with an inverse fourier transform:

$$I_{CCD}(\tau, T, \omega_3) = E_S(\tau, T, \omega_3)E_{LO}(\omega_3)^* e^{-i(\omega_3(t_S - t_{LO})+\varphi)} + c.c. \quad (71)$$

Now, it is necessary to remove the time delay between LO and k_3 just multiplying the complex signal by $e^{-i(\omega_3(t_{LO}-t_{k_3}))}$ restoring the correct time origins.

E_{LO} is finally removed by dividing the signal by the square root of the spectrum of LO, independently collected: $E_{LO}(\omega_3) = \sqrt{I_{LO}(\omega_3)}$.

The last but not less important operation to achieve the correct absorptive part of the third order signal is the phasing procedure. In fact, we acquire a complex signal and its absorptive (real) part has to be discerned by its imaginary part, associated with refractive index phenomena. There are different methods to extract the real phase of the signal. The most widely used method exploits the projection slice theorem[39]. It is based on a minimization algorithm in which the integration of the 2D signal along ω_1 is subtracted from the pump probe spectrum [40].

Once the right phase is found, correct 2D maps can be found simply by FT along t_1.

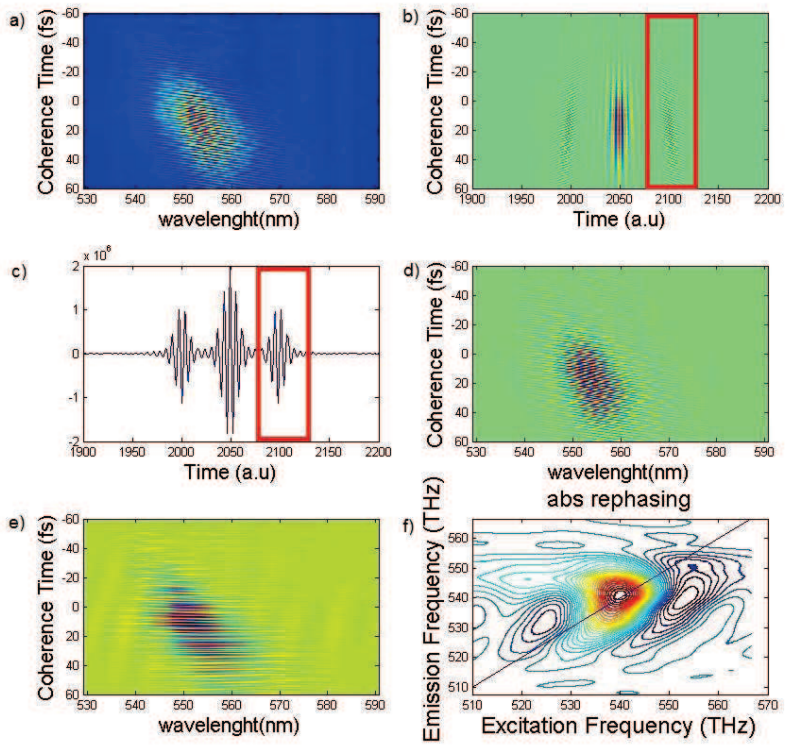

Figure 24. a) Raw data collected by CCD camera. b) Fourier transform of the wavelength axis from frequency-space to time-space. (c) A horizontal slice of b) at t_1 = 0 fs, the red rectangle is the selection of times used in the time filtering. (d) An inverse Fourier transform is performed on the horizontal dimension of the selected signal. (e) Signal is multiplied by $e^{i\omega t_{LO}}$, by phase factor and divided by $\sqrt{I_{LO}}$. (f) A Fourier transform is performed along t_1, thereby producing the final 2D ES spectrum.

2.3.7 2DES maps analysis

When all the corrections on the raw recorded signal are done, a 3D matrix of the third order signal is obtained as a function of ω_1, t_2 and ω_3. We thus have a set of maps at increasing values of population time t_2. The evolution of the 2D maps along t_2 provides lot of information about relaxation dynamics of the systems, the possible presence of transfer processes and the energy of the states involved in the transfer. Moreover, the ultrafast time resolution allows following the evolution of vibrational or electronic coherence at early times after photoexcitation. In order to extract this information a complex analysis toolbox was set up.

Let's focus first on the analysis of the decay of the signal along t_2, providing information about the time constants regulating the relaxation dynamics of the system. The analysis of decays in 2D signals is very similar to that of pump probe. The only difference is that here we are dealing with the decay of a 2D matrix of points instead than of a 1D spectrum. In literature, there are many examples of global target analysis also on 2D maps [41][42]. With this analysis, it is possible to isolate the contribution to the map coming from different species or states. Moreover, it is possible to follow energy flow through states. The possibility of spreading the information contents along two dimensions in a map instead of a 1D spectrum makes clearer the identification of the mechanisms of energy transfer. For example, if state *b* is initially excited by the laser and then relaxes through energy transfer to a different state *a*, we would detect a decreasing signal at the diagonal coordinates of state *b* and an increasing off-diagonal signal with coordinates (ω_a,ω_b) (figure 25).

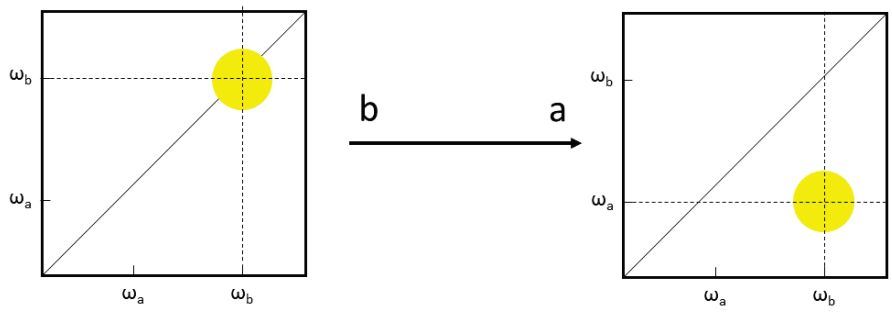

Figure 25 Example of 2D signal due to energy transfer. Initially b state is excited at ω_b and the signal is emitted at ω_b until the excitation is transferred to a, when the signal will be emitted at ω_a. Following the decay of the signal at (ω_b, ω_b) and the rising at (ω_b, ω_a) allows studying energy transfer dynamics.

The study of coherences can be important when studying quantum coherent energy transfer but also vibronic coupling and vibrational coherences. Section 1.5.1 describes how to recognize vibrational and electronic coherences, whereas now the tools used to characterize the coherences are explained.

The best way to isolate oscillations due to coherences from the decaying signal is to remove all the non-oscillating parts of the signal. This can be done at each point of the map by fitting the decay with a multi-exponential function and subtracting it from the experimental data. However, it is more physically meaningful to fit globally the decay of the map to find common time constants for all the

points of the map. Thus, even though only few points of the map are taken into account in the analysis, the dynamic behavior of the whole map is considered. For the global fitting procedure, the approach is that proposed by Van Stokkum called variable projection algorithm[26], [43].

Once the fitting function is subtracted from the experimental data, the oscillating residuals are analyzed with different methods to unravel frequencies and time properties of the associated coherences.

To determine the frequencies of oscillations, the first obvious method is to perform Fourier Transform along t_2. Repeating this procedure for each point of the 2D maps generates new frequency maps, also known as 'Fourier maps' [44]. In these maps the amplitude and phase distribution of each frequency component contributing to the beating is plotted in a 2D spectrum as a function of ω_1 and ω_3 frequencies like in 2D maps. This method is extensively used by many groups [45]. However, since the intensity of the signal in the map is dependent on the laser shape, often frequency maps appears distorted and with many artifacts. For this reason, we prefer to select points in the map that correspond to selected coherences and to study singularly their time traces.

An example of the exhaustive analysis that we usually perform on 2D data is shown in figure 26. On the residuals of the multi-exponential fitting, we first perform the conventional FT and the linear prediction z-transform (LPZ), a transform that enhances the resolution of FT when applied to decaying oscillating signals [46]. We also set up an additional analysis, based on time frequency transform (TFT) formalism, that allows us extracting a higher amount of information from oscillating traces.

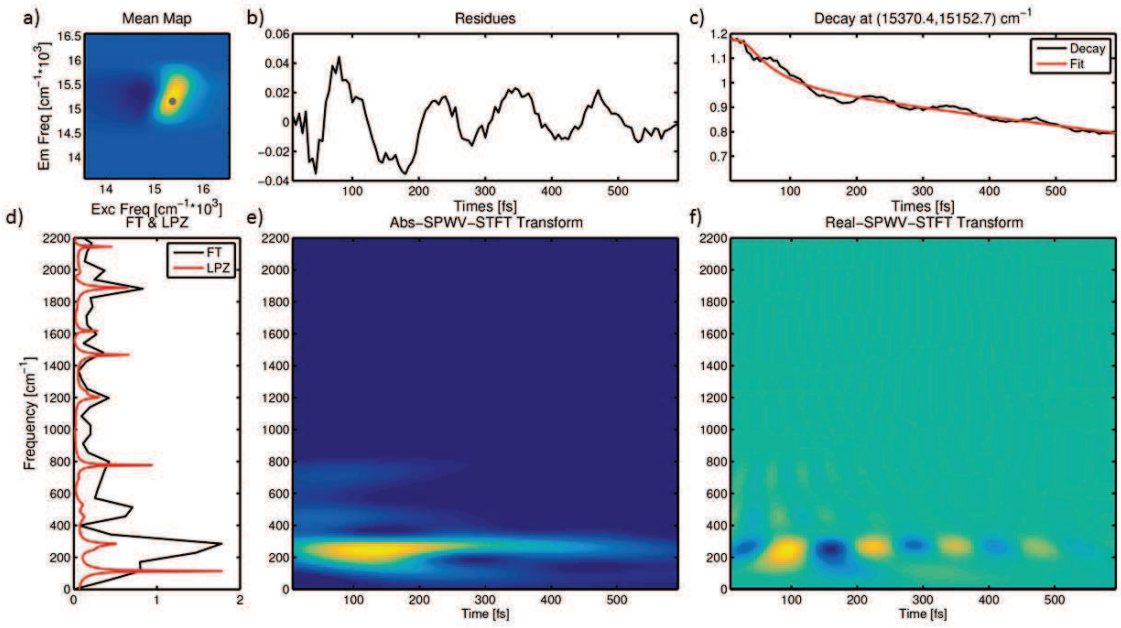

Figure 26 An example of the analysis performed on a single point of the 2D map. a) A point is selected in the map and the time trace at that coordinates is extracted. c) multi-exponential fitting is performed on the time trace. b) the fitting function is subtracted to the experimental trace to remove all non oscillating contributions. d) Fourier transform and LPZ transform are applied on oscillating residuals. e) and f) are absolute and real TFT maps, respectively. Absolute TFT map highlights the intensity changes of the oscillation. Real map allows to asssess also the phase of the oscillations.

Time frequency transforms are able to keep information in both frequency and time domains. Thus, it is possible to follow in time the intensity of the oscillations with a determined frequency. There is a variety of TFT approaches. The first TFT proposed to analyze the evolution of 2D spectra has been the Wavelet transform[47]. A further development of this analysis proposed in our lab comes from the use of bilinear transforms. Association of different bilinear transforms give rise to best performance transform exploited in this thesis [46]. A TFT map is generated applying TFT on the residuals. It shows in the y-axis the frequency of the oscillating components while in x-axis their time behavior. Absolute maps show only the intensity of the oscillation, whereas real maps can highlight also the relative phases. Summarizing, with these maps it is possible to distinguish efficiently oscillations at different frequencies and comparing their relative amplitude and phase. Moreover, it is possible to follow their intensity along the time axis.

3 EXPERIMENTAL RESULTS: TPPS J-AGGREGATES

3.1 LINEAR SPECTRA AND ELECTRONIC PROPERTIES OF TPPS J-AGGREGATES

The term aggregate is used to describe a collection of molecules that are generally self-assembled by electrostatic forces. First observation of aggregation of organic molecules was achieved independently by Jelley and Scheibe in 1936, when they observed that the electronic absorption spectra of certain cyanine dyes changed dramatically during the increase of the dye concentration [48], [49]. In fact, absorption spectrum changes is the most obvious evidence for aggregate formation.

Aggregates are classified in two types, H- and J-, depending on the angle between the transition dipole moments of the neighboring molecules. In particular, when the dipole moments of two neighboring molecules are head-to-tail oriented, the aggregate is called J- and has an absorption band red shifted with respect to the monomer, while when the dipole moments are head to head oriented, the aggregate is called H- and the absorption band is blue shifted. The new excited states of aggregates have characteristic of Frenkel exciton states with the excitation delocalized over many monomers thanks to the strong coupling between the optical transitions of the monomers themselves. The generated absorption band has a really sharp and Lorentzian shape. These properties could be explained by exchange narrowing effects[50].

The incredible optical and electrical properties of molecular aggregates has been extensively studied in the past years and they were found to be optimal candidates to various applications: sensor, two-photon absorption, photovoltaics and even quantum computing[51]. Moreover, porphyrin aggregates are often used as models for natural light harvesting antennas. In fact, porphyrin has structure and optical properties similar to those of chlorophyll, the dyes used by nature and the exciton in its aggregate has very similar behaviors to those of natural systems [52].

Tetra Sulphonated-phenyl porphine (TPPS) is an ideal molecule to artificially synthesize aggregates. In fact, it is sufficient to control the pH of an aqueous solution of TPPS to induce aggregation. In neutral solution, TPPS molecule (m-TPPS) carries four negative charges in the sulfonated groups (figure 27,

panel a). When pH goes under ≈5, the two iminic groups in the center of the molecule acquire two protons with their positive charges (figure 27, panel b). The protonation of the molecule leads to a structural change and introduces a change in the symmetry from C_{2v} to S_4 [53].

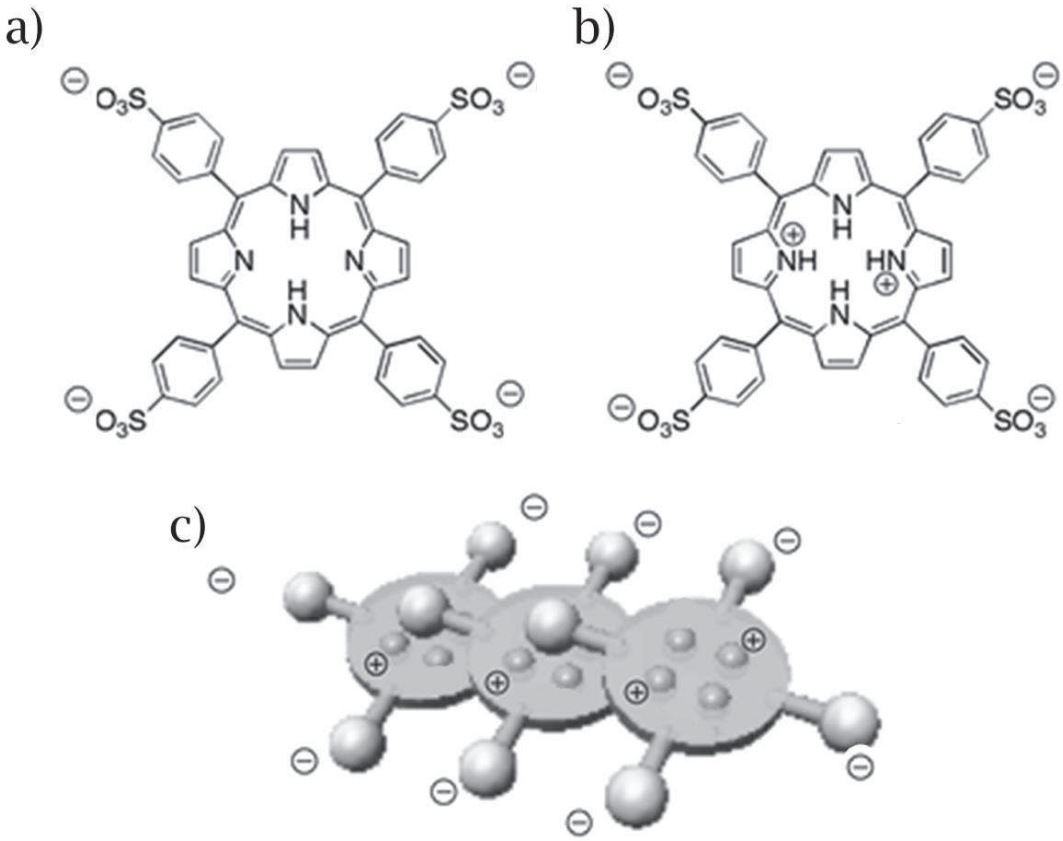

Figure 27 Structure of TPPS in aqueous solution at neutral pH (m-TPPS, a), in acidic environment (m-H_2TPPS, b) and a pictorial view of the aggregate structure (a-H_2TPPS, c).

The structural change could be seen in the absorption spectrum where the protonated TPPS (m-H_2TPPS) is characterized by a slight red shift of the B band from 412 nm to 434 nm and Q_x and Q_y bands become degenerate (Figure 28) with respect to TPPS free base.

These new geometry and charge distribution are ideal for the formation of aggregates. In fact, strong electrostatic intermolecular interactions between the negative charges at the edges and the positive

charges in the center favor the formation of a linear chain of porphyrins (a-H_2TPPS), schematically illustrated in panel c of figure 27.

Since porphyrins have two degenerate transition dipole moments perpendicular to each other, the formation of the aggregate leads to the appearance of both J- and H- bands. In particular, the B band of m-H_2TPPS generates a J-band at 490 nm with the transition dipole moments orientated along the linear chain of molecules and a weaker H-band at 422 nm with the transition dipole moments orientated perpendicular to the linear chain. Since the excitonic interaction is weaker in the case of the Q bands at 645 nm, only its J component is visible in the absorption spectrum and appears at 705 nm.

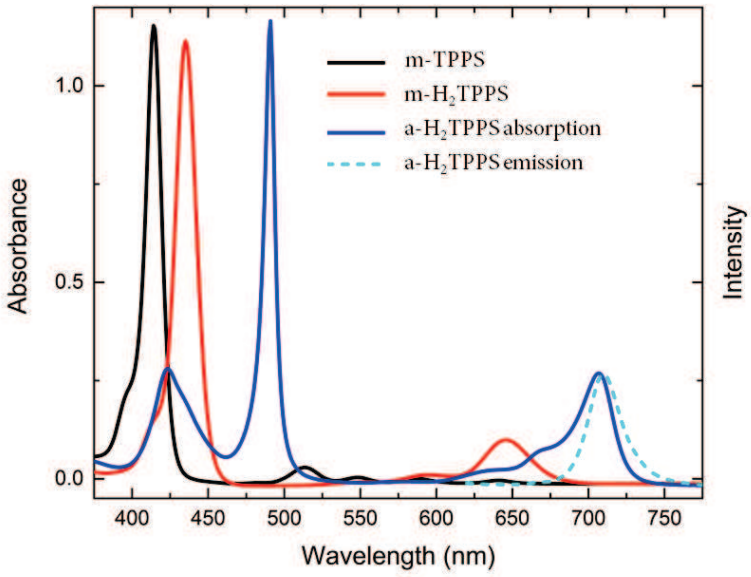

Figure 28 Absorption spectra of m-TPPS free base, protonated m-H_2TPPS and a-H_2TPPS J-aggregate in water. Cyan dashed line shows the aggregates emission.

As outlined before, the excitonic bands of aggregates are sharper than the monomer bands and they assume a more Lorentzian-like shape especially in the case of 490 nm J-band. This is due to the weak coupling with environment and vibrations and the strong electronic coupling between monomers. The reduced linewidth has been explained by an exchange narrowing effect [54]. The quickly moving exciton is subject only to an average inhomogeneity which is reduced by roughly a factor of $\sqrt{N_C}$ where

N_C is the number of coherently coupled molecules [55]. The weak interaction with environment and vibrations is also confirmed by the very small stokes shift between absorption and emission peaks (figure 28).

One of the easier way to describe excitonic bands formation was proposed by Scherer[54]: assuming that aggregates are linear and treating their electronic transitions assuming strong coupling between the monomers transitions, it is possible to write the one-exciton band with this formula:

$$|k> = \frac{2}{\sqrt{N+1}} \sum_{n=1}^{N} \sin\left(\frac{nk}{N+1}\right) |0_1 \dots 1_n \dots 0_N> \tag{72}$$

Where N is the number of monomers among which excitation is shared (estimated to be about 10 at room temperature for B band [54]), k is a quantum number, and n labels the molecule in the excited state. The excitonic state is a linear combination of all the monomer states in which one molecule is excited and the others are in the ground state. The energies of the new excitonic states are then

$$E_k = E_0 + 2J \cos\frac{\pi k}{N+1} \tag{73}$$

where E_0 is the energy of the monomeric state and J is the electronic coupling between monomers. The width of the excitonic band is then equal to $4J$ and the energy difference between excitonic states is dependent on J and the coherence length N. However, optical transitions are allowed only toward few excitonic states. In fact, it is possible also to calculate the transition probability between ground states and excitonic states as:

$$|M_k|^2 = \mu^2 \frac{2}{N+1} \frac{1-(-1)^k}{2} cot^2\left(\frac{k\pi}{2(N+1)}\right) \tag{74}$$

The quantum number k identifies the excitonic state. Its minimum value is 1. According with the equation 74, only transitions toward states characterized by odd values of k are allowed. In particular, only k =1 (k_1)[1] and k =3 (k_3) have non-negligible probability of transition (figure 29).

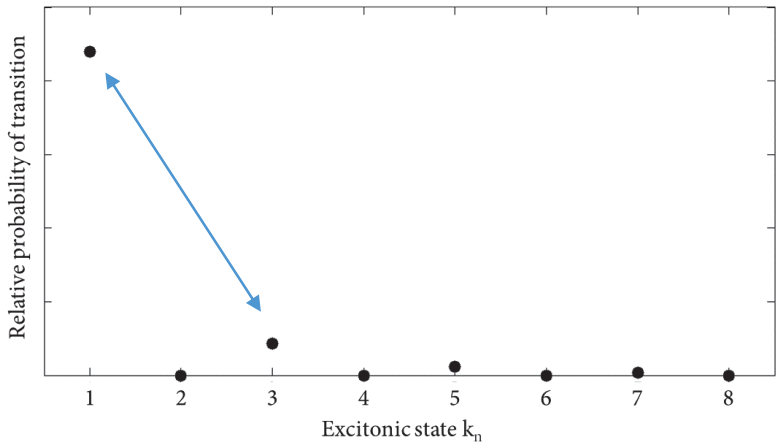

Figure 29 Probabilities of transition of the excitonic states of a linear aggregate. Only k_1 and k_3 have non-negligible values.

In case of intense light, the probability to excite more than one exciton in the same aggregate become non-negligible. Excitation of the second exciton obeys the Pauli Exclusion Principle, thus the lowest two-exciton state consists of one exciton occupying k_1 excitonic state and the other the k_2 excitonic state:

$$k_1 + k_2 >= \frac{2}{N+1} \sum_{n_2 > n_1 = 1}^{N} \left[\sin\left(\frac{n_1 k_1}{N+1}\right) \sin\left(\frac{n_2 k_2}{N+1}\right) - \sin\left(\frac{n_2 k_1}{N+1}\right) \sin\left(\frac{n_1 k_2}{N+1}\right) \right] |n_1 n_2 > \qquad (75)$$

[1] In this chapter, k_x identifies excitonic states and must not be confused with the momentum of pulses treated in previous chapters.

This is also the two-exciton state with the greatest probability of transition within the two-exciton band. Then, the energy difference between the most probable one exciton state (k_1) and the most probable two exciton state (k_1+k_2) is greater than that between the ground state and the one exciton state.

3.2 PRELIMINARY CHARACTERIZATION AND SELECTION OF THE BEST SAMPLE

3.2.1 Counterion effects on Aggregate's formation and optical properties

Recent work demonstrated that the method followed in the preparation of the aggregate is central in determining the kinetic of aggregates formation, their final geometry and optical properties. For example, it is possible to obtain in a controlled way linear or fractal assemblies suitably controlling the pH and the ionic strength of the solution [56][57], [58]. A strict control of the experimental conditions is thus necessary in order to obtain samples with reproducible properties. Recent evidences seemed to suggest that the nature of the counterion of the acid used in the acidification of the m-TPPS molecule to obtain m-H_2TPPS could be critical in terms of optical properties. A preliminary study of how the counterions present in the aqueous solution affect the formation and the properties of the TPPS aggregate was thus necessary. We tested the optical properties of J-aggregates prepared using a set of different acids chosen among the ones most frequently employed in the literature (H_2SO_4, $HClO_4$, HNO_3, HCl, HBr, and HI) by means of linear absorption and emission, time resolved fluorescence spectroscopy and pump probe. This preliminary characterization allowed the identification of the best preparation conditions in order to obtain the most stable and reproducible structures to be studied with 2D spectroscopy.

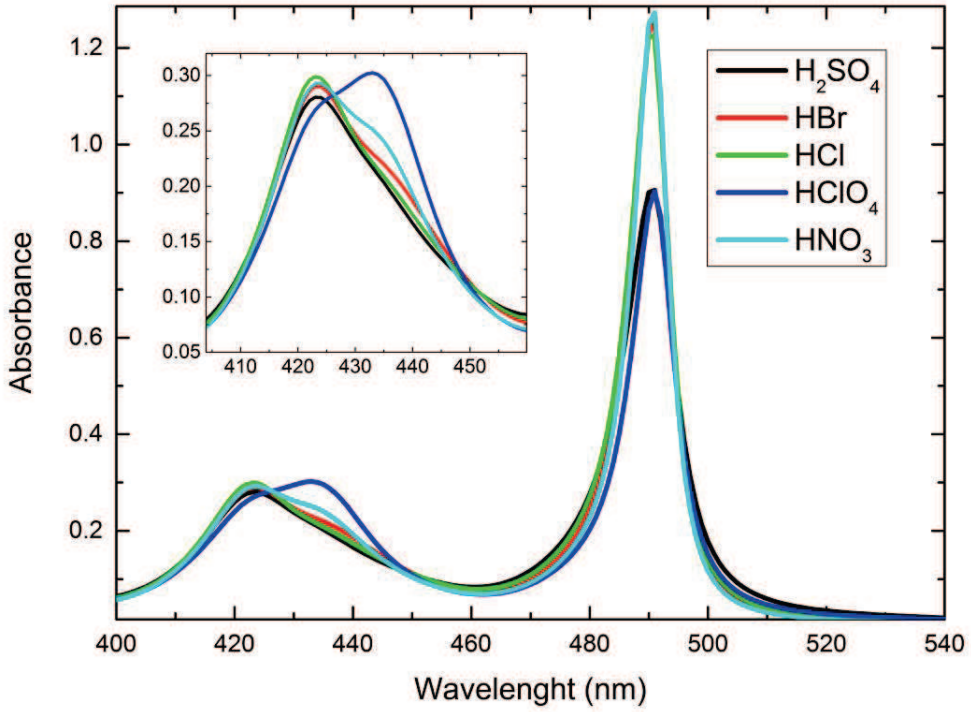

Figure 30 Comparison of absorption spectra of TPPS aggregates prepared with different acids. In the inset an enlargement of the region where the monomeric m-H_2TPPS contributes more.

The absorption spectra of J-aggregates prepared starting from different acids are shown in figure 30. All the other experimental conditions, such as the concentration of TPPS (30 μM) were left unchanged. The spectra do not show any striking difference. Modifications in the spectra are recorded only in the 434 nm region where the residual monomer absorbs (figure 30). This means that the use of different acids does not change the absorption properties of the aggregate but affects only the degree of aggregation. The ability to induce aggregation follows the series: H_2SO_4 > HCl > HBr > HNO_3 > HI > $HClO_4$.

Also emission spectroscopy does not highlight any difference as a function of the acid used. Fluorescence spectra of different solutions are indeed superimposed when normalized (figure 31).

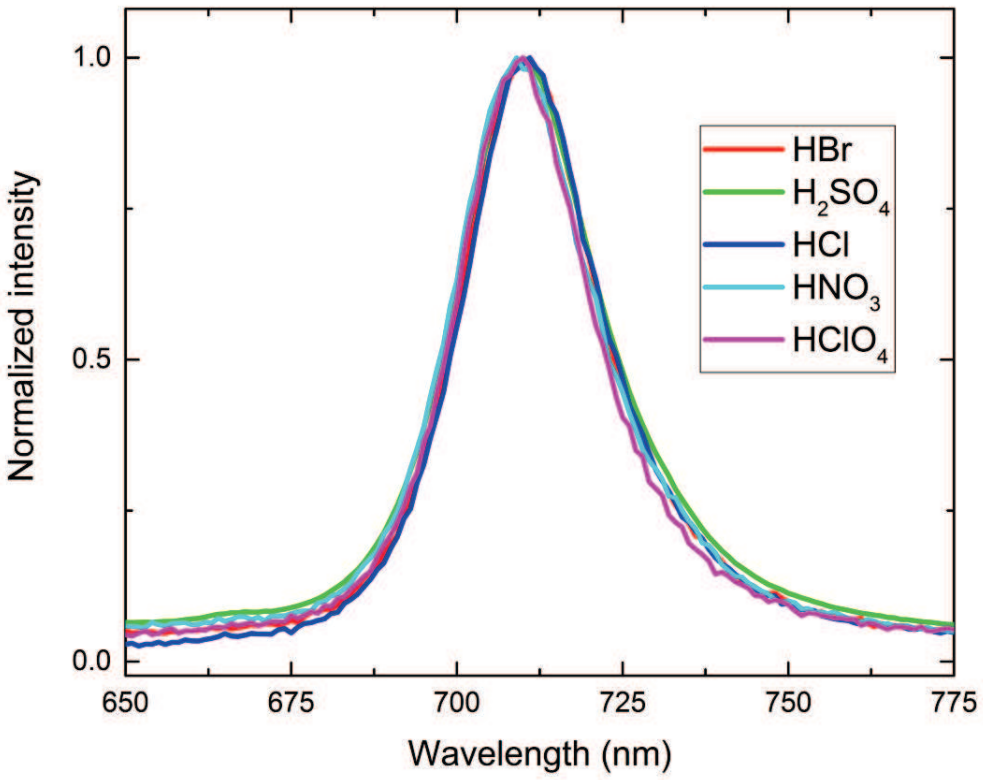

Figure 31 Normalized emission spectra of differently prepared TPPS J-aggregates excited at 490 nm. No differences can be highlighted as a function of the acid used in the preparation.

Therefore, linear absorption and emission spectroscopies do not highlight any differences in the aggregate's optical and electronic properties once the aggregate is formed. Different acids lead only to different kinetics and yields in the formation of the aggregate.

However, more information can be obtained applying time resolved spectroscopies, able to assess the possible influence of different acids in the dynamics of the excited states. The aggregates prepared with different acids were thus studied by means of time-resolved fluorescence spectroscopy.

Fluorescence lifetime was measured on all solutions with TCSPC method using a 150 fs frequency doubled Ti:Sapphire laser (420 nm) as exciting source. The time resolution of the experiment is about 100 ps. The detection apparatus does not allow performing frequency-resolved measures since it

integrates the signal emitted at all wavelengths. The detection wavelength could be roughly selected only with suitable combinations of long- and short-pass filters.

In any case, it was not possible to separate the contributions of residual monomer and of the aggregate species from the overall fluorescence signal since they emit in the same spectral range. Moreover, the fluorescence quantum yield of the monomer is at least one order of magnitude higher than the one of the aggregate [51], [54]; therefore, even a small amount of residual monomer in the aggregate solution could generate a strong fluorescence signal.

For this reason, the fluorescence decays shown in figure 32 were fitted with bi-exponential functions where the short time τ_1 could be associated to the decay of the aggregate while the longer time τ_2 to the decay of the monomer. Previous studies in the literature demonstrated indeed that the fluorescence lifetime of m-H_2TPPS monomer is in the order of few nanoseconds, whereas upon aggregation the lifetime is shortened to hundreds of picoseconds.

Table 3 Time constants of biexponential fitting of fluorescence decays.

	τ_1(ns)	τ_2(ns)
H_2SO_4	0.324	3.428
HCl	0.32	2.938
HNO_3	0.337	3.529
$HClO_4$	0.363	3.657
HBr	0.349	0.826
HI	~0.3	0.376

The parameters reported in table 3 confirm that the decay time of the aggregates does not show any dependence on the acid within the experimental error. For all the samples the decay time is found to be about 320-360 ps. The slight differences are attributable to instrument sensitivity and experimental errors. There are instead clear differences in the decay times of the monomer samples acidified with

different acids, mainly attributable to the quenching effect of halides. In fact, the only samples characterized by a lifetime far from the literature value of 3.5 ns, are those related to the solutions of HCl, HBr and HI (for which a lifetime of 2.94 ns, 0.83 ns and 0.375 ns was found, respectively).

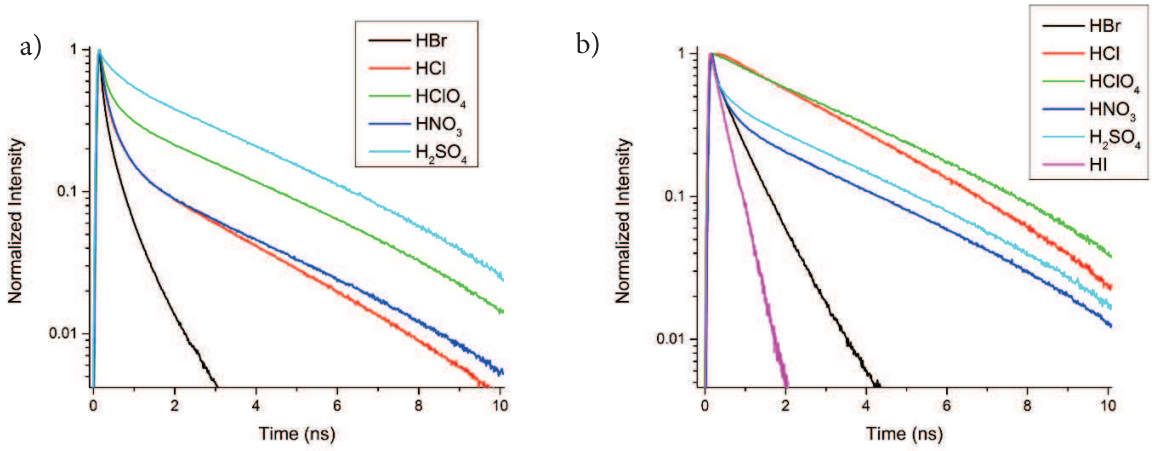

Figure 32 a) Normalized fluorescence lifetime of solutions of a-H2TPPS prepared with different acids collected at aggregates emission wavelength. It is possible to notice the initial decay due to aggregate fluorescence and then the longer decay of residual monomer. b) same spectra collected at the monomer emission wavelength. Different slopes means different decay constants.

To confirm that the two time constants determined in the fitting correspond to the monomer and aggregate species, Fluorescence lifetime imaging (FLIM) were performed on solution of TPPS aggregate deposited on glass. Aggregates can reach size in the order of micrometers and tend to precipitate on the glass. In this way, they can be distinguished from the rest of solution where the intense fluorescence of monomer stands out.

The FLIM images are obtained with the same apparatus used for time-resolved measurements. The coupling of the TCSPC detection system to a confocal microscope allows achieving not only time resolution but also space resolution. It is thus possible to record the fluorescence decay in different positions of the sample and draw spatial maps of fluorescence decay by assigning to each pixel of the detector a decay curve. If, as in our case, there are two decay times, they can be associated to different

colors and the intensity of the color is proportional to the amplitude of the exponential. Briefly, a pixel mono-colored means that in that position there is the presence only of the species characterized by that decay time.

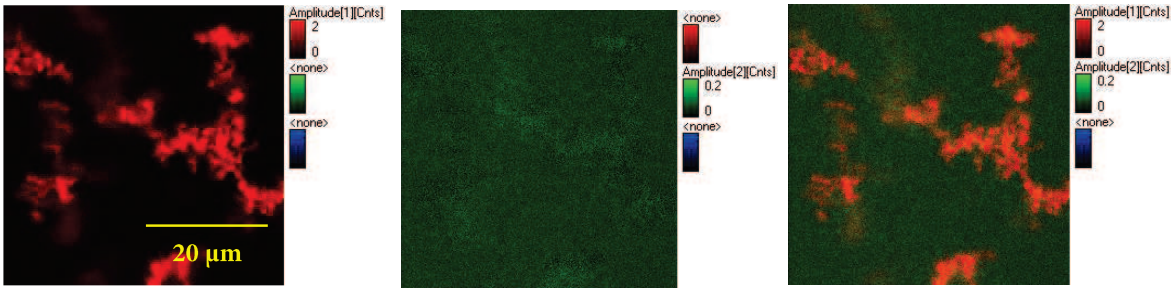

Figure 33 FLIM images of TPPS in H_2SO_4 solution. Red: amplitude of the short time constant (0.324 ns). Green: amplitude of the long time constant (3.428 ns).

FLIM images (figure 33) show the formation of big aggregates (tens of microns). In all cases, the amplitudes of the longer times are uniformly distributed throughout the image and therefore they are attributable to the residual monomer in solution (green). On the other hand, the amplitude of the short time constant is relevant only where an aggregate is present (red).

The reduction of lifetime of the monomer for HCl, HBr and HI solutions was quite unexpected. It is reasoning that the reduction of lifetime is due to quenching of fluorescence generated by the halides present in solution. There are two kinds of quenching: static and dynamic. In the static case the quenching takes place only when the halide forms a complex with the monomer instead in the dynamic one the quenching happens only when monomer and halide collides each other. The efficiency of the two typologies of quenching depends differently on the concentration of the quencher. For this reason an acid concentration dependent analysis was performed.

The lifetimes are influenced only by the dynamic quenching and follow the equation:

$$\frac{\tau_0}{\tau} = 1 + k_D[Q] \tag{76}$$

where τ_0 is the lifetime in absence of quencher, k_D is the speed constant for dynamic quenching and [Q] is the concentration of the quencher. Thus, the reduction of lifetime is surely due to dynamic quenching.

To assess the possible presence of static quenching, fluorescence intensity has to be measured:

$$\frac{F_0}{F} = 1 + k_D[Q] + K_S[Q] + k_D K_S[Q]^2 \tag{77}$$

where F_0 is the fluorescence intensity in absence of quencher, K_S is the equilibrium constant:

$$K_S = \frac{[TPPS - Q]}{[TPPS][Q]} \tag{78}$$

The comparison between static and dynamics quenching mechanism was studied on a solution of aggregate obtained using HBr. We prepared a series of solution with the same concentration of TPPS (4.1 μM) and increasing concentration of the Br^- counterion. Results are represented in figure 34. Panels a and b show the reduction of fluorescence lifetime and fluorescence intensity, respectively, for increasing values of quencher concentration.

k_D was calculated with a linear fit of the τ_0/τ curve based on equation 76 and is equal to 6.5. The F_0/F curve is practically superimposed to the lifetime curve, making difficult the identification of a possible static contribution (equation 77). Simulations performed imposing different values of K_S (green, cyan and magenta lines in the panel c of figure 34 allow verifying that only very low values of K_s can justify the linear behavior of the F_0/F curve. Consequently, with a concentration of hydrobromic acid of 0.5 M, we can estimate that the percentage of TPPS "complexed" and statically quenched by is less than 5%. The contributions of static quenching in this system are thus negligible. Hence, counterions do not “complex” the charge porphyrins.

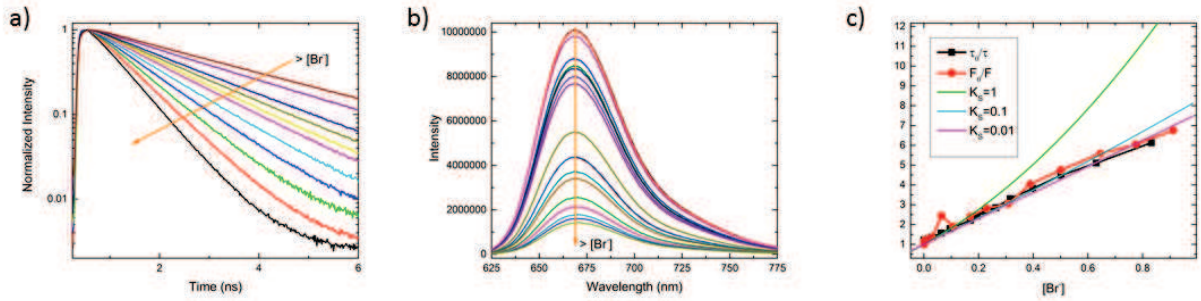

Figure 34 Fluorescence lifetime a) and intensity b) decreasing as afunction of increasing quencher concentration. c) shows the linear dependence of both $\frac{\tau_0}{\tau}$ *and* $\frac{F_0}{F}$ *on the concentrantion of quencher. Three simulated curves are shown in the same figure to compare the dependence in case of the static quenching with 3 different values of Ks.*

The preliminary characterization of the dynamic properties of the aggregate species was completed with pump probe measurements. Pump probe measurement were performed with the optical setup presented in section 2.1.

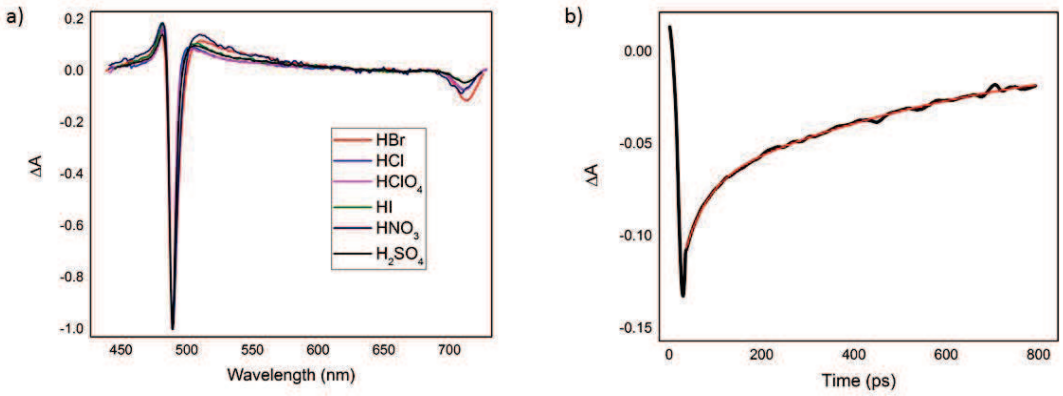

Figure 35 a)Pump probe spectra of aggregates prepared with different acids at t=0. b) Experimental decay trace of the sample prepared with H_2SO_4 *(black) and the correspondent three-exponential fit (red).*

Also in this case the main dynamical properties of the aggregate seem not to be particularly influenced by the nature of counterion (figure 35). Figure 35 panel a shows normalized spectra of TPPS aggregates

in various acids extracted at t=0. The differences between them are minimal and can be attributed to experimental issues. The same for the time dependence. All time traces could be fitted with three-exponential functions reporting the same values of time constants. Panel b of figure 35 displays the decay trace at 490 nm of the H_2TPPS aggregate prepared with H_2SO_4. Besides the expected 300 ps time constant measured previously with the fluorescence lifetime technique, a 50 ps and a >2 ns time constants were found. The former is attributed at excited states and vibrational relaxations, whereas the latter was quite unexpected. In fact, no time constants longer than the lifetime of the fluorescent state would be expected unless considering the presence of lower energies dark states. The presence of such component can be attributed to the formation of long-lived species in solution, such as triplet states, radical pairs, or other photodegradation products. Assessing the nature of these species is of crucial importance since the accumulation of long-live species may lead to artifacts or signal drifts in the 2D spectroscopy measurements. Since most of these possible ling-lived species are characterized by the presence of paramagnetic properties, their nature was investigated by means of electronic paramagnetic resonance techniques (EPR).

3.2.2 Electronic paramagnetic resonance reveals triplets and charge states on TPPS aggregates

EPR experiments were performed in collaboration with Dr. M. Albertini of the EPR group at University of Padova leaded by Prof. D. Carbonera.

EPR techniques are able to study all the paramagnetic species present in the sample. An interesting version of this spectroscopy (time-resolved EPR, TR-EPR) can study the paramagnetic species generated after the excitation of the sample with a light pulse. Thus, it is absolutely indicated to study triplet and charged states generated after the interaction with laser pulses. To have a full picture, we compare triplet states generated by laser excitation in m-TPPS, m-H_2TPPS and in a-H_2TPPS.

As shown in previous section, the aggregation process causes dramatic reduction of the lifetime of the singlet excited state S_1[54]. Time resolved fluorescence measurements performed on the TPPS aggregates at room temperature reveal a lifetime of the first excited singlet state of about 300 ps, which is about ten times shorter than that obtained for the monomeric acidified H_2TPPS. Owing this fast time constant, the triplet state population process via inter system crossing (ISC) is expected to be strongly

suppressed, and indeed the photophysical behavior of a-H_2TPPS has always been attributed only to singlet states. However, it will be demonstrated that triplet state is generated also in aggregates.

The line shape of the EPR spectrum is characterized by zero field splitting parameters. In particular, the parameter D could be extracted from the width of the TR-EPR spectrum and it is particularly useful for characterization of the system. In fact, it is associated to the spatial extent and shape of the triplet spin wavefunction according to equation:

$$D = \frac{3}{4}\left(\frac{\mu_0}{4\pi}\right)(g_e\beta_e)^2 \langle \frac{r^2 - 3z^2}{r^5} \rangle \tag{79}$$

where μ_0 is the vacuum permeability, g_e is the free electron g factor, β_e is the Bohr magneton, r is the distance between the two interacting spins centers, z is the same distance between the spins projected onto the z-principal axis of the zfs tensor. D value is as higher as the two electron in the triplet wavefunction are closer.

The TR-EPR spectrum of the photoexcited triplet state m-TPPS randomly oriented in a water/methanol matrix at 130K together with the corresponding spectral simulation is reported in figure 36 (black spectrum). The spectrum shows the same polarization pattern EAEAEA (in which E stand for an emission and A stands for an absorption signal) and almost the same *zero-field splitting* (zfs) parameters D and E of the more known free base tetra phenyl porphyrin (TPP) [59] reflecting similar geometrical arrangement of zfs tensors and nearly identical intersystem crossing (ISC) kinetic. From the simulation, the value of D parameter is 420 Gauss.

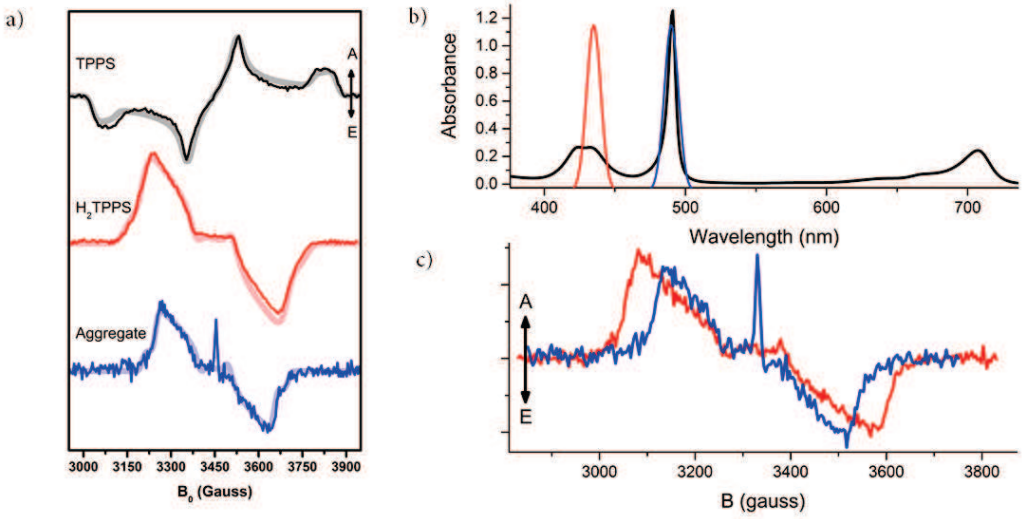

Figure 36 a) TR-EPR spectra of m-TPPS (black), m-H_2TPPS (red) and a-H_2TPPS (blue). In panel b) the laser excitation wavelength used to record TR-EPR spectra of monomer (red) and aggregate (blue) is shown. Panel c) reports the corresponding spectra of the monomer (red) and aggregate (blue).

A completely different spectrum, characterized by the peculiar AAEAEE polarization pattern and a new set of zfs parameters, is obtained when the same TPPS solution is acidified with a H_2SO_4, as reported in figure 36 panel a (red spectrum). As already introduced, in this case the protonation is expected to take place at the two iminic sites with a consequent saddle-like distortion of the tetrapyrrolic macrocycle. The large alteration in the photoexcited TR-EPR spectrum reveals that changes take place in the matrix elements of the ISC process responsible for the anisotropic population of the three spin sublevels. This change leads to different kinetics of the population of triplet spin sublevels with respect to m-TPPS and consequently to a different polarization scheme in the TR-EPR spectrum. The value of D parameter is here 309 Gauss.

The photoexcited TR-EPR spectrum of a frozen concentrated aqueous solution of a-H_2TPPS is reported as the blue spectrum in figure 36. In this case, the polarization pattern is the same AAEAEE as obtained for the m-H_2TPPS species, thus suggesting that the aggregation process does not alter the mechanism of triplet state population. The change in the field position of the EPR canonical transitions indicates that the zfs parameters shifted, with a clear reduction of the D parameter that is now 250 Gauss. The

spectrum appears with a significant lower signal to noise ratio mainly because of the poor quality of the aqueous matrix which causes large light scattering. Moreover, the fast quenching characterizing the S_1 singlet state of aggregated TPPS reduces the global triplet yield.

Photoexcited TR-EPR investigation has been performed also on a mixed sample containing both the m-H_2TPPS and the a-H_2TPPS species by selecting the appropriate laser excitation wavelength by means of an OPO module. Actually, three resolved absorption bands characterize the region of the UV-Vis spectrum below the 500 nm of the mixed sample as expected: the 420 nm and the 490 nm bands attributed to the a-H_2TPPS while the 434 nm band to the m-H_2TPPS. The photoexcited TR-EPR spectra obtained by selectively exciting the m-H_2TPPS at 434 nm and the a-H_2TPPS at 490 nm are identical to that reported in figure 36 a for the pure constituents of the mixed sample (figure 36 b,c).

The reduction of the D parameters from 420 to 309 Gauss observed upon acidification can be associated to the distortion of the spatial wavefunction away from the planarity, which causes an increase of the projection of the inter-spin distance onto the *z*-principal axis.

On contrary, the reduction of the D parameters from 309 to 250 Gauss when aggregation takes place is directly connected to the increase of the extension of the triplet state spatial wavefunction according to equation 79. This effect has been already reported for dimeric free base TPPS in an investigation study of cation induced aggregation[59]. The large delocalization of the triplet state leads to the possibility of populating a long-living trapped electronic states characterized by a charge separation either in singlet and triplet spin multiplicity.

Interestingly, a polarized radical species characterized by a net absorptive EPR signal and an AE polarization pattern appears only in the TR-EPR spectrum of a-H_2TPPS (figure 37). This signal can be tentatively attributed to a charge separation taking place along the aggregate.

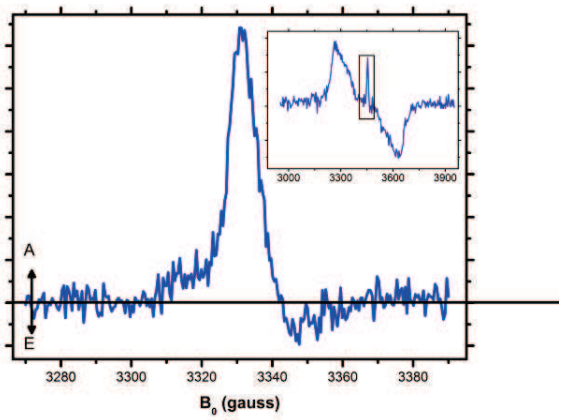

Figure 37 Zoom of the signal attributed to a radical species present in the aggregate spectrum.

Understanding the nature of this charge separation needs further studies. However, this study demonstrates, first of all, that triplet state are generated also in TPPS aggregates and that it is delocalized along the monomers. Then, charge separation takes place only in aggregates and charge radical generated seems to be stable at least at low temperature.

3.3 2D MEASURES ON J BAND

In the previous section, we demonstrate that solutions of a-H_2TPPS prepared with H_2SO_4 suffer fewer influences with respect to solutions with other acids. In fact, H_2SO_4 guarantees the highest aggregation yields and HSO_4^- does not seem to interfere with optical properties of a-H_2TPPS.

We focalized our attention on the 490 nm region where there is the presence of excitonic band with the highest excitonic coupling [54]. The sharp and intense J-band at 490 nm generated from the B band of the H_2TPPS can be assigned to the transition from the ground state to the first excitonic state k_1. Moreover, it presents also a slight asymmetry with a kind of "shoulder" at higher energies due probably to the transition towards the k_3 excitonic state. In agreement with equation 73, the energy of excitonic state k_3 at room temperature should be in the order of hundreds of cm^{-1} above k_1. In next section, it will be demonstrate to be precisely 400 cm^{-1} above k_1 from 2Q2D measurement. This few levels simple model is then suitable to describe the absorption spectrum.

The model can be completed considering the Resonant Raman spectrum, showing a strong enhancement especially of two low frequency vibrational modes, evidence of vibronic coupling with the electronic transition. Off-resonance Raman spectrum of the aggregate performed at 514 nm highlights the frequencies of the vibrational modes of the aggregates. There are peaks at 244, 319, ≈700, ≈1000, ≈1200 and ≈1500 cm^{-1} (figure 38). The normalized resonant Raman spectrum (488 nm) is superimposed showing that the modes at lower frequency are generally enhanced. In particular, the enhancement is particularly noticeable for the two transitions at 244 and 319 cm^{-1}. This two modes are assigned respectively to out-of-plane ruffling and doming and the enhancement could be explained by a sort of collectivization of movement[51].

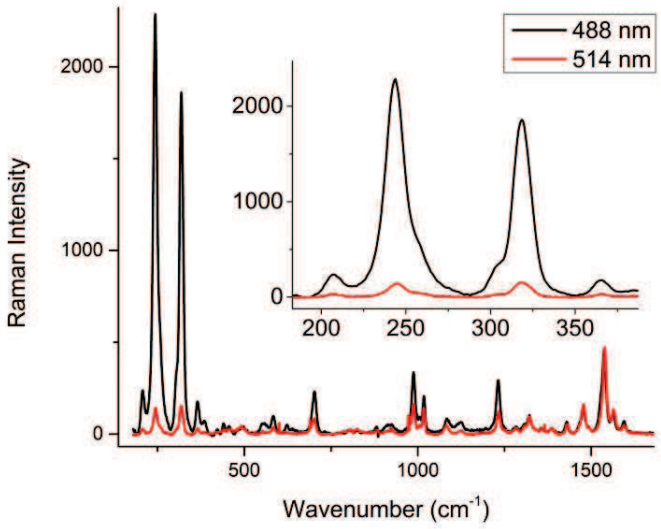

Figure 38 Resonant(black) and non resonant(red) raman spectra of TPPS J-aggregate. When raman spectra is performed with 488 nm laser there is a great enhancement of 244 and 319 cm^{-1} peaks.

It is then expected to find a contribution of these vibronic transitions also in the absorption spectrum. They are not clearly detectable because they have really low frequency (244 and 319 cm^{-1} are included in the linewidth of the electronic transition that is ≈500 cm^{-1}) but they could be part of the high energy shoulder together with the k_3 transition. The scheme of energies levels emerging from all these observations is depicted in figure 39.

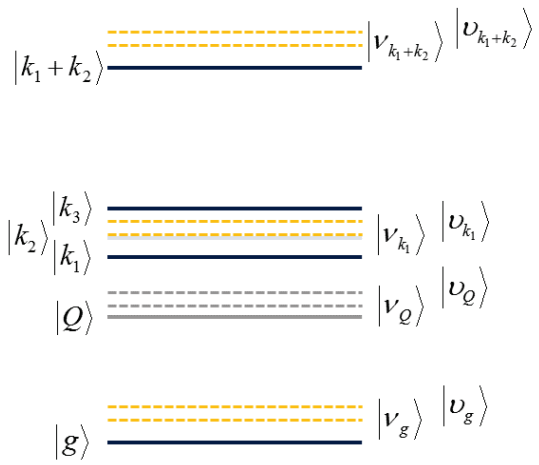

Figure 39 Schematic view of the energy levels of the TPPS aggregates. Vibrational states ν (244 cm^{-1}) and υ (319 cm^{-1}) more strongly coupled with the electronic transitions are represented by orange lines. One-exciton band comprises k_1, k_2 and k_3 excitonic states. Transitions from ground state toward k_2 are forbidden. The lowest energy state $k_1 + k_2$ of the two exciton band it is also represented.

In aggregates of TPPS, the excitonic band with the highest excitonic coupling is that at 490 nm. 2DES studies on this band could be important to have a clearer view on how excitonic coupling modulates the relaxation dynamics within the band. This is not an easy task given the ultrafast nature of the involved processes, often making impossible their clear characterization with conventional techniques. Moreover the presence in the one-exciton band of several states very close in energy, most of which are dark in conventional optical spectroscopies, complicates even more this task. 2DES is particularly suited for this aim, given the flexibility of the experimental conditions and the ensuing possibility of reconstructing with great accuracy frequency and time information.

With the aim of unraveling the complex structure and dynamics of this band, both rephasing and non-rephasing maps have thus been collected. Moreover, double quantum (2Q) spectroscopy was also performed to have the most complete set of data and assess the positions of dark higher energy states.

Samples have been prepared by dissolving the TPPS powder in water and adding H_2SO_4 until pH=1. The concentration of TPPS was adjusted to reach 0.4 of absorbance at 490 nm in 1 mm path cells. Oxygen was removed from solutions by bubbling nitrogen. Then, the measurements were performed as described in Chapter 2.

3.3.1 Double Quantum 2D measurements (2Q2D)

Double quantum measurement can help finding excitonic energies. Double quantum technique is described in Chapter 2 and essentially investigates the coherence between the ground state and states at about twice the energy of the laser frequency. In other words, a 2Q2D will provide a non-negligible signal only when the system has a higher energy state at about twice the energy of the first resonant transition. For this reason, it is particularly useful to characterize high energy states. In the case of TPPS J-aggregate, it correlates the energy of a doubly excited state with the energy of emission from a single excited state. Double excitation is easily achievable in TPPS J- aggregate because of the particular one- and two-exciton band structure described before. In particular, while for the first excitation the main transition is from *g* toward k_1 state, the second excitation starting from k_1 can only reach the state with $|k_1 + k_2>$ because of selection rules [51]. The frequency of oscillation after double excitation is the sum of the frequencies of k_1 and k_2. In the double sides Feynman diagram framework, the only two allowed pathways are represented in figure 40 panel a, b. The first pathway (red) generates a positive signal with frequency $\omega(k_1\text{-}g)$ instead the second one generates a negative signal with frequency $\omega(k_2\text{-}k_1)$. Assuming that the energies of the states do not change when doubly excited, the distance between the positive and the negative peaks in the 2Q2D map identifies exactly the energy difference between state k_1 and k_2 (figure 40 panel c). Using equations 73 it is then possible to extrapolate the energy of state k_3 that is about 400 cm^{-1} higher than k_1. The 2D2Q map has thus been crucial for the correct identification of the

energies of the first three states of the one-exciton band, employed for the interpretation of the overall aggregate dynamics.

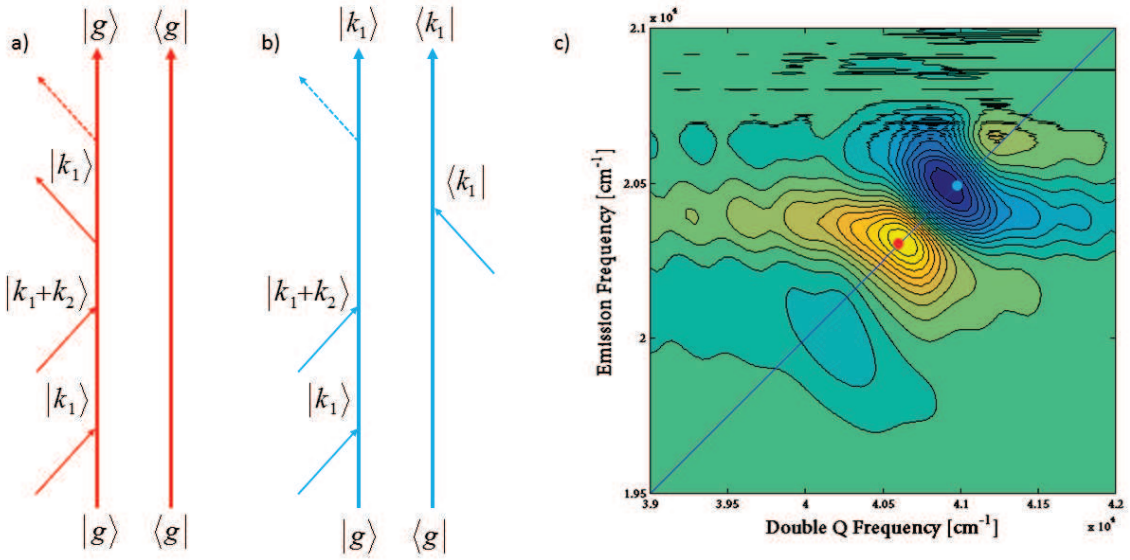

Figure 40 a) and b) represent the positive and the negative Feynman paths that contribute to 2Q signal, respectively. c) the double quantum signal with highlighted frequencies of (k1-g) and (k2-k1).

3.3.2 Rephasing and non-rephasing 2D measurements

In 2D rephasing and non-rephasing measurements, the laser band has been tuned in order to be superimposed with the J-band at 490 nm so to be able to excite all the allowed states of the one-exciton band.

In the previous sections, we have already discussed the structure of the 490 nm band showing that, despite its narrow bandwidth, several states contribute to the overall optical response: the band comprises at least three one-exciton states (k_1, k_2, and k_3) (one of which (k_2) dark in optical absorption) and at least two vibrational sublevels at 244 and 319 cm^{-1}, labeled ν and υ , respectively, above the

vibrational ground state. The laser band is broad enough to excite coherent superpositions of all these states: electronic coherences (for example between k_1 and k_3 states), vibrational coherences in the ground state or vibronic coherences within the one-exciton band. Now, given the broadening effect at room temperature and the close proximity of the energy of investigated levels, we expect that in 2D spectra the spectral features corresponding to the different electronic, vibrational or vibronic coherences are superimposed.

Indeed, the rephasing maps shown in figure 41 are characterized by a positive signal mainly distributed on the diagonal, especially at early times. Two negative peaks due to ESA are present in off diagonal regions. As t_2 increases, the signal decays and starts to broaden. Furthermore, the lowest negative peak becomes more intense than the upper one, leading to a slight shift of the main positive band toward higher energies.

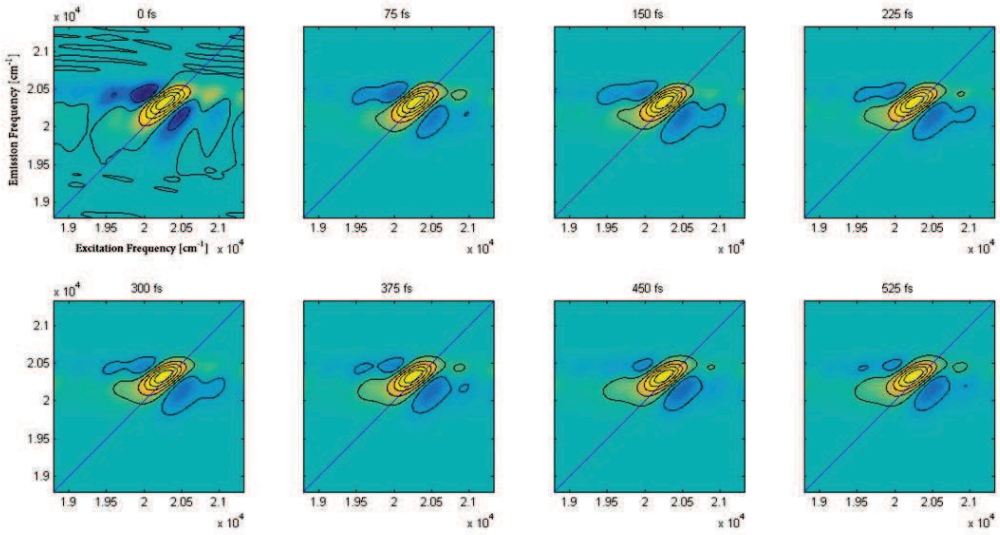

Figure 41 Evolution of the real part of the rephasing maps.

The non-rephasing maps (figure 42) have, as expected, a different shape with respect to the rephasing ones. They present a positive signal oriented perpendicularly to the diagonal and the two negative peaks along the diagonal. Again, as t_2 increases, the signal decays and broadens.

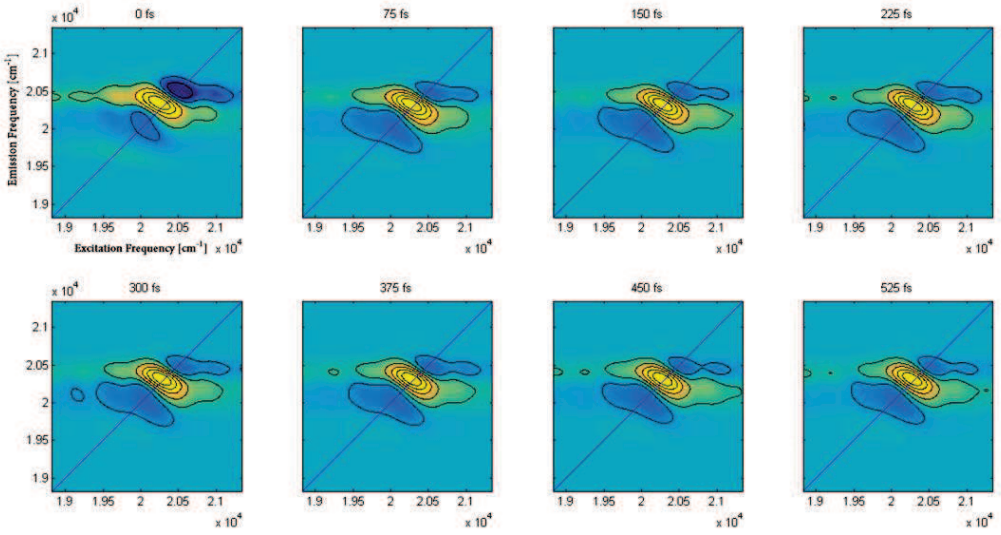

Figure 42 Evolution of the real part of the non-rephasing maps.

In both rephasing and non-rephasing maps the main central positive signal is located at 20300 cm^{-1}, corresponding to the frequency of the transition between the ground state and the excitonic state k_1, as found in the absorption spectrum. We can thus attribute this peak to GSB and SE involving this transition. The negative signals can instead be attributed to excited state absorption from k_1 to states of the two-exciton band falling at about twice the energy of the g-k_1 transition.

The main peak however includes also subtle signatures of the coherent superpositions prepared by the exciting laser. To study the dynamics of such coherences, it is useful to extract the evolution of the signal along t_2 in selected points of the map, where superpositions of different states contribute. The positions at which different coherences should contribute more are estimated based on the energy level model

depicted in figure 43 and on the careful selection of relevant Feynman diagrams as described in Chapter 1.

For example, the time trace extracted at point with coordinates (20300 cm^{-1}, 20544 cm^{-1}) should show mainly the evolution of the coherence between k_1 and $k_1 + \nu$, where ν is the state lying at 244 cm^{-1} above or below k_1. We thus look at positions 244 and 319 cm^{-1} far from the k_1 transition to search for the vibrational coherences and at positions 400 cm^{-1} far from the k_1 transition for the electronic k_1-k_3 coherence. Only k_1-k_3 excitonic coherence is taken into account because the transition to k_2 is not allowed.

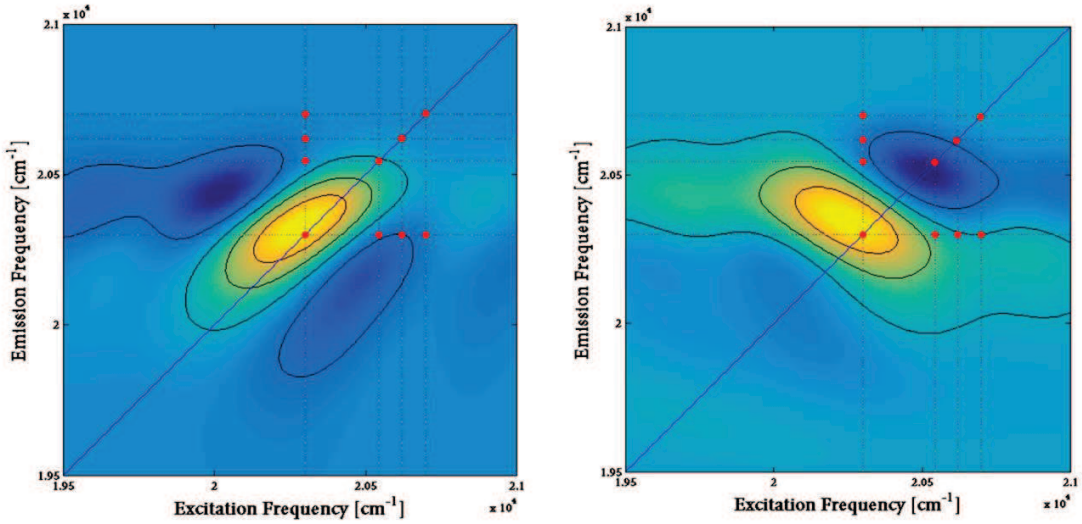

Figure 43 Rephasing (left) and non-rephasing (right) maps at T=0. Red dots highlight the positions where contributions of vibrational and electronic k_1- k_3 coherence should contribute more.

For seek of clarity, it is worthy to stress that the resolution of the maps and broadening effects at room temperature do not allow to well separate and distinguish the contributions. Thus, it is always found that oscillations due to a specific coherence contribute also in points related to other coherences.

The vibrational coherences are present in most part of both rephasing and non-rephasing maps. Figure 44 panel a illustrates where the oscillating contributions of the coherence between k_1 and ν and υ should be present and where they effectively are. Figure 44 panel b shows an example of a time trace obtained plotting the 2D signal at coordinates (ω_{k1}; $\omega_{k1+\nu}$) as a function of t_2 with the corresponding multi-

exponential fit in red; the residuals of the fit containing only the oscillations carrying information about coherent dynamics. At these specific coordinates both ν and υ vibrational coherences are contributing, as confirmed by the time frequency transform of the residuals.

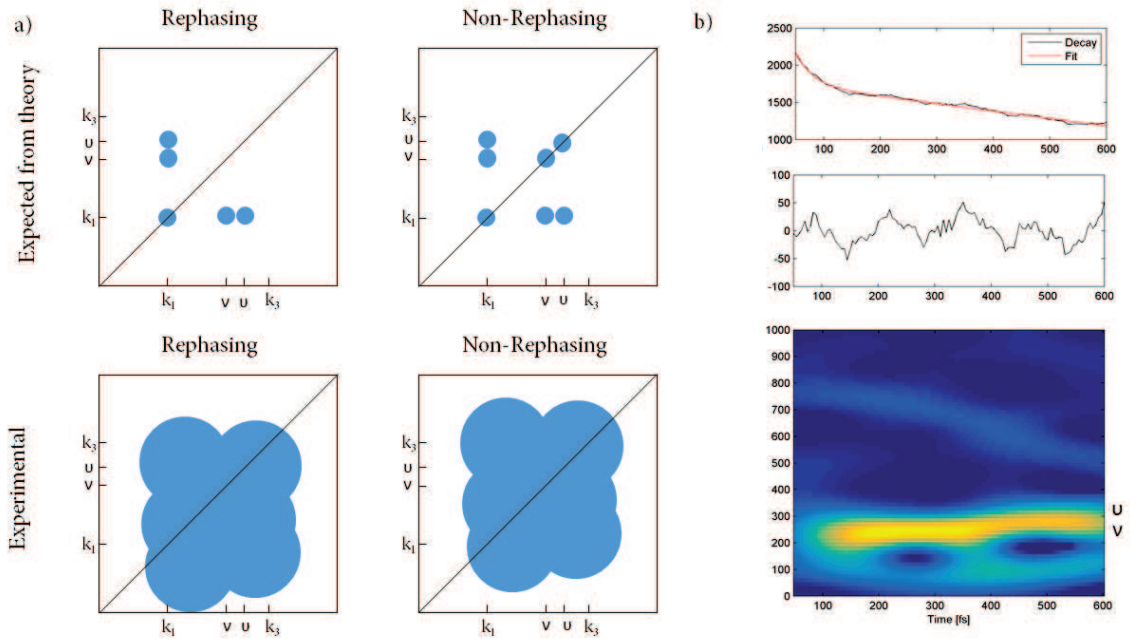

Figure 44 a) Comparison between theoretical and experimental maps. The positions where vibrational coherences are expected to be and where the have been experimenatlly detected are highlighted. b) selected trace extracted at (ω_{k1}; $\omega_{k1+\nu}$). TFT performed on residuals of a muliexponentil fit shows a clear long-lasting oscillation at frequency compatible with ω_ν. The signals corresponding to the two vibrations ν and υ cannot be fully resolved because of the frequency resolution of the 2D equipment.

The same analysis was performed at positions where the electronic k_1-k_3 coherence is expected to appear. The results are summarized in Figure 45. At these positions, together with residual contributions of the k_1-ν and k_1-υ vibrational coherences oscillating at 244 and 319 cm^{-1}, respectively, a third contribution oscillating with a frequency of about 400 cm^{-1} is recorded. This is in perfect agreement with the evolution of the k_1-k_3 coherence.

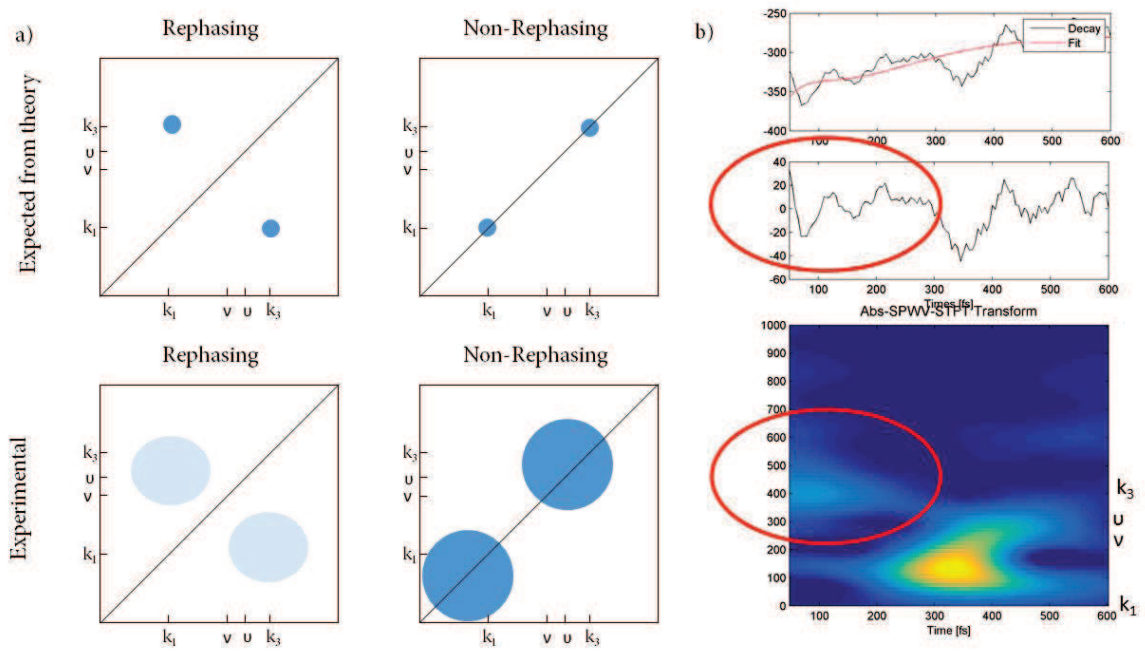

Figure 45 a) Comparison between theoretical and experimental maps. The positions where electronic coherences are expected to be and where the have been experimenatlly detected are highlighted. b) selected trace extracted at (ω_{k3}; ω_{k1}). TFT performed on residuals of a muliexponentil fit shows a fast dephasing oscillation at frequency compatible with $\omega_{k3\text{-}k1}$.

The comparison of the results reported in figures 44 and 45 confirms that vibrational coherences are present in both rephasing and non-rephasing spectrum and contribute at all positions in the map. The TFT analysis shows that they last for the whole time window investigated as expected for vibrational coherences, typically endowed with damping times in the range of few picoseconds. Different is the behavior of the oscillations at 400 cm^{-1}. It appears only at off-diagonal positions in the rephasing spectra and in corresponding on-diagonal positions in the non-rephasing ones. Moreover, the TFT analysis shows that this oscillation is damped within the first 200 fs after photoexcitation. All this characteristics are typical of electronic coherences, confirming the attribution of this feature to the evolution of the k_1-k_3 coherence.

The synergic use of several 2D techniques allowed clearly recognizing the electronic coherence between k_1 and k_3 excitonic state and distinguish it from the vibrational ones, on the bases of subtle data analysis and thanks to the theoretical predictions treated in section 1.4. Since the presence of this coherence was not so clear in the rephasing spectrum, the recognition of this coherence was possible only thank to the

non-rephasing maps. All states of the one exciton band has been completely revealed. Moreover, it was also possible to characterize the dephasing of electronic coherence, that last no longer than 200 fs, thanks to TFT maps. This dephasing time is compatible with electronic coherence decay at room temperature. Consequently, despite the fact that this system should have low interaction with the environment, it does not seem that electronic coherences last excessively longer than in other conventional systems.

Moreover, differently from what suggested for biological light-harvesting complexes, we did not find any evidence that vibrations help and sustain somehow electronic coherence. On contrary, if they have an effect on electronic coherence, it is destructive. This represents an important piece of information since it clearly demonstrate that the presence of strong electronic and vibronic coupling may be necessary but not sufficient conditions to guarantee the 'vibrationally-driven long lived coherence' mechanism invoked to explain 2D data measured on light-harvesting systems[60]. More subtle effects, for example due the proteic environment absent in our system, must thus be investigated. The very close resemblance of TPPS J-aggregates with the bacteriochlorophyll aggregates present in chlorosomes, the extremely efficient light-harvesting antennas of green sulfur bacteria, re-opens the question of the relevance of coherence in natural occurring energy transfer processes. The investigation of this phenomenon is still at its beginning and we are still far from a full comprehension of it. Further investigations are thus needed.

4 SOLVENT EFFECTS ON EXCITATION OF ORGANIC DYES.

The effects of the solvent in absorption spectra of organic dyes were extensively studied since fifties [61]. However, even recently, theory and experiments on solvatochromism and solvent effects are still interesting scientists[62], [63]. Solvent, and more in general the surroundings of the molecule, can interact with the absorbing dye in different ways. The first effect to be considered is related to the electric properties (dielectric constant ε, and refractive index *n*) of the solvent, having an important role in the absorption strength. The oscillator strength for a chromophore transition is defined as:

$$F = \frac{2303 * m_e c}{\pi e^2 N_A} \frac{n}{f^2} \int \varepsilon dv \tag{80}$$

where n is the refractive index of the medium and f is a local field correction that accounts for the different polarizability between molecule and medium. There are different ways of describing the local field correction such as cavity field model, Lorentz model and more recent theoretical developments[11] but, independently on the model, the physical insight is that the oscillator strength is always dependent on n that is characteristic of the solvent.

Moreover, the solvent can modulate the frequency of the transition both with its polarity and with specific solvent–solute interactions such as hydrogen bonding, π-π stacking and dipole-dipole interaction. This effect is due to the stabilization or destabilization, in term of energy, of the ground or the excited state or both.

Besides these static effects, many other dynamic effects can be detected in the time domain. An example is the spectral shift of the fluorescence spectrum when collected at different delay times from the excitation[64]. As the delay increases, the solvent can reorganize spatially to minimize energy of the excited state. This effect is mainly present in polar solvents.

In the ultrafast regime, the interaction of the excited molecule with the surroundings is usually described by mean of random fluctuations and static disorder. For example, electronic or vibrational

states coherently excited undergo a dephasing due to solvent-induced fluctuations. The time evolution of the excited states are described in literature by several theories such as Redfield relaxation theory and further developments[10], [11]. However, the solvent is usually described as a continuum and specific interactions are often neglected.

Recently, it was discovered that the protein environment in the natural photosynthetic antennas offers to the chromophores an optimized geometry for the excitonic interactions and the ideal vibrational landscape to preserve electronic states coherences during the energy transport [19], [6]. Long-lived electronic coherences have been proposed as responsible of the almost unitary efficiency of the exciton transport in natural antennas. This is the first time that vibrations of the environment are considered to be, not only non destructive, but also helpful for the survival of the electronic or vibrational coherences in the molecule. This was the motivation for studying the model system described below.

To study the interaction between solvent and dye, a system was chosen where this interaction is expected to be the strongest possible. Thus, a doubly charged molecule made by two pyridines and a pyrrole units conjugated (called PEPEP) (figure 46) was chosen to strongly interact with high dipolar solvents such as dimethyl sulfoxide (DMSO), deuterated dimethyl sulfoxide (d6-DMSO) and acetonitrile (CH3CN).

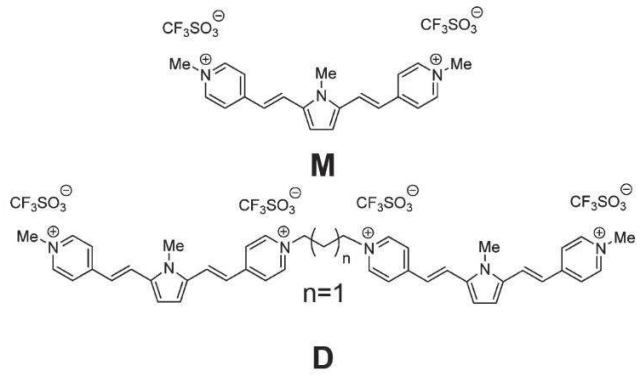

Figure 46 Structure of the organic dyes considered to study solvent-dye interactions..

The IUPAC name of PEPEP molecule is 2,5-bis[1-(4-N-methylpyridinium)ethen-2-yl)]-N-methylpyrrole ditriflate and, for simplicity, it will be named monomer or M. M is a quadrupolar molecule with an Acceptor-π-Donor-π-Acceptor structure. Owing to its electronic structure, M belongs

to a class of molecules endowed with a strong intra-molecular charge-transfer absorption band in the visible, and as such they could be suitable candidates to build artificial antenna systems. Both theoretical and experimental studies have been done on this molecule and especially in some covalently linked homodimer [65][66]. Two PEPEP molecules joined by a short alkyl chain (named dimer or D) already showed interesting optical properties, such as good two photon absorption cross section, due to the presence of excitonic interactions[67]. The presence of excitonic interactions between the two monomeric units in D is confirmed by the reduction of the lifetime and the different dynamics of the excited state.

The aim of this work was to study experimentally possible interactions between vibrations of solvent and the dye. The study was intended to compare dynamical solvent effects on M and D due to three different solvents, having similar electric properties but different frequencies of vibrations. To do that, a combination of linear, vibrational and time resolved spectroscopies was used.

4.1 SOLVENT PROPERTIES

As anticipated before, PEPEP is a doubly charged molecule so it is soluble in highly polar solvents. For this study, three polar solvents were selected for their different vibrational properties: CH_3CN, DMSO and d-6 DMSO.

Table 4 Main electric properties of the three selected solvents.[2]

	CH_3CN	DMSO	d-6 DMSO
Dipole moment (D)	3.92	3.96	3.96
Refractive index	1.344	1.479	1.476
Dielectric constant	38.8	47.24	47.6
Nonlinear femtosecond refractive index	3.3	3.2	

The main electrical and optical properties of the solvents are listed in table 4. It is evident that these solvents are very similar, in particular DMSO and d-6 DMSO, having the same geometry and electronic structure, and differing only for the frequency of their vibrational modes. In fact, when deuterium atoms substitute the hydrogen atoms in DMSO, the frequencies of the vibrations change. Heavier atoms lead to lower frequencies. In figure 47 the Raman spectra of the three solvents are reported. The CH_3CN has three main vibrations in the region of interest, one just below 400 cm^{-1}, one just above 900 cm^{-1} and one around 1400 cm^{-1}. The DMSO has a strong band at 670 cm^{-1} and three other weaker bands around 400, 1050 and 1400 cm^{-1}. The d-6 DMSO has a similar spectrum but all the bands are shifted at lower frequencies of about 50 cm^{-1}.

[2] These data are retrieved from manufacturers' catalogs.

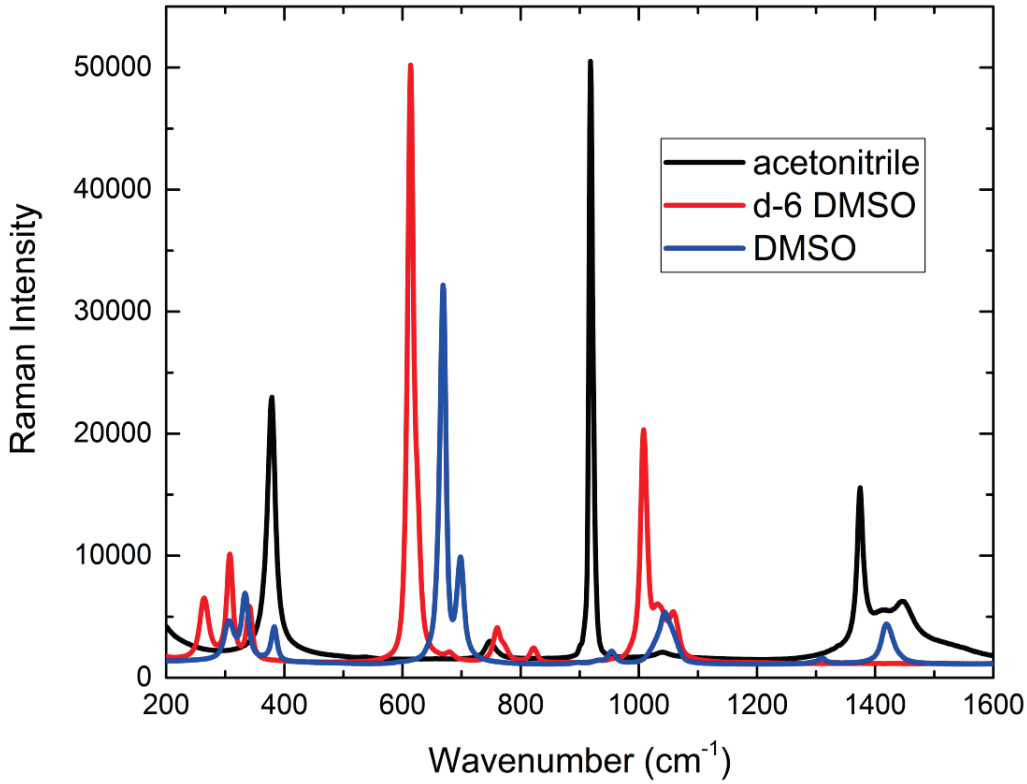

Figure 47 Raman Spectra of the three pure solvents.

4.2 PEPEP PROPERTIES

All the most relevant properties of the PEPEP systems, including the interaction with environment, could be recognized in the linear absorption spectra. The spectra, in all cases, are broad (> 2000 cm^{-1}) due to large inhomogeneous broadening. The spectrum of the dimer is in all solvents redshifted compared to the spectrum of the monomer (figure 48). This means that there is an interaction between the two branches[66]. The absorption spectra of the molecules dissolved in DMSO and deuterated DMSO (d-6 DMSO) are almost superimposed (figure 48).

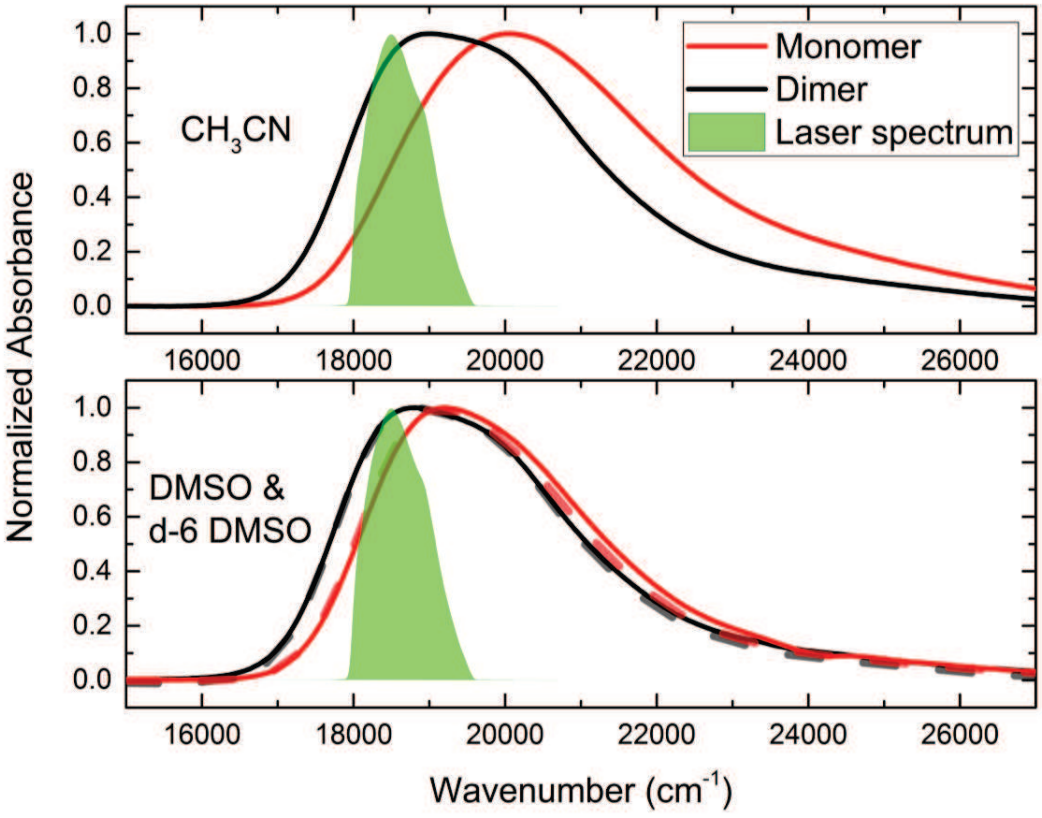

Figure 48 Absorption spectra of M(red) and D (black) in different solvents. Differences in the absorption spectra in DMSO (solid lines) and d-6 DMSO (dashed lines) are negligible. Green shadowed area shows the laser spectrum used in 2D spectroscopy (Section 4.3).

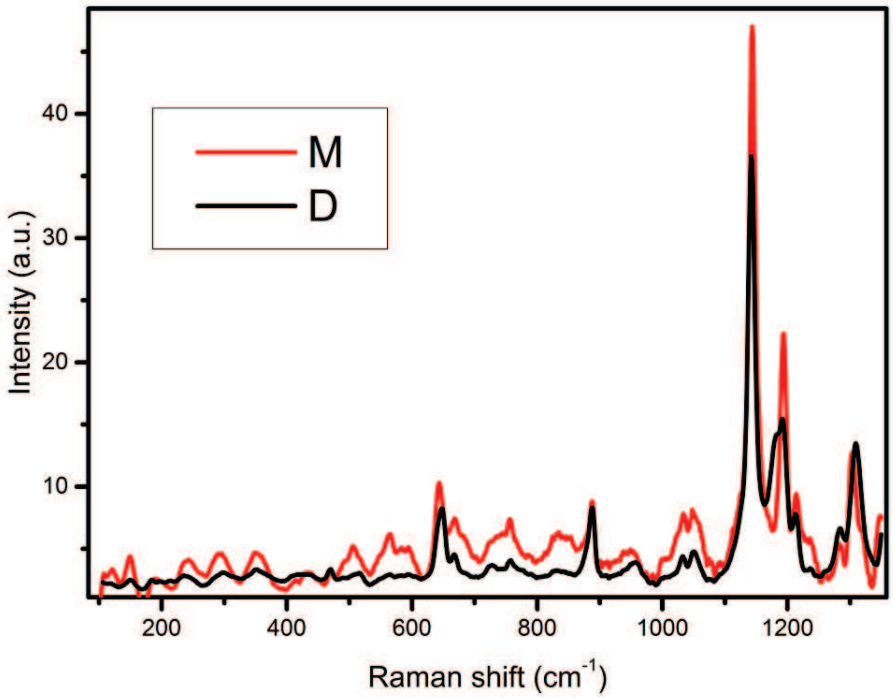

Figure 49 Resonant Raman spectra recorded on powder samples of monomer (red) and dimer (black).

As expected, the Raman spectra of powders of M and D show only few negligible differences, mostly due to different signal-to-noise ratio. The spectra were acquired in resonant conditions, exciting with an argon laser at 514 nm. Unfortunately, the spectra are noisy, especially for M. It was not possible to increase the signal-to-noise ratio because the sample started to burn increasing the laser power as well as lengthening the acquisition time. However, in the region between 0 and 1400 cm^{-1}, that is our region of interest, many peaks can be clearly recognized: at 640, 887 and some over 1000 cm^{-1}. Comparing the position of the Raman signals of PEPEP molecules with those of the solvents, the peak at 640 cm^{-1} matches perfectly the main Raman bands of d-6 DMSO, while a 887 cm^{-1} peak slightly matches an oscillation present in the acetonitrile at 929 cm^{-1}. The most intense peaks are situated in the 1100-1300 cm^{-1} region, where typically the stretchings of C=C contribute.

The IR spectra show similar results. Also in this case only small differences between M and D were recorded. The IR spectra have a greater signal-to-noise ratio compared with Raman so it is possible to

detect also weaker features. However, the main signals fall at the same frequencies as in the Raman spectra.

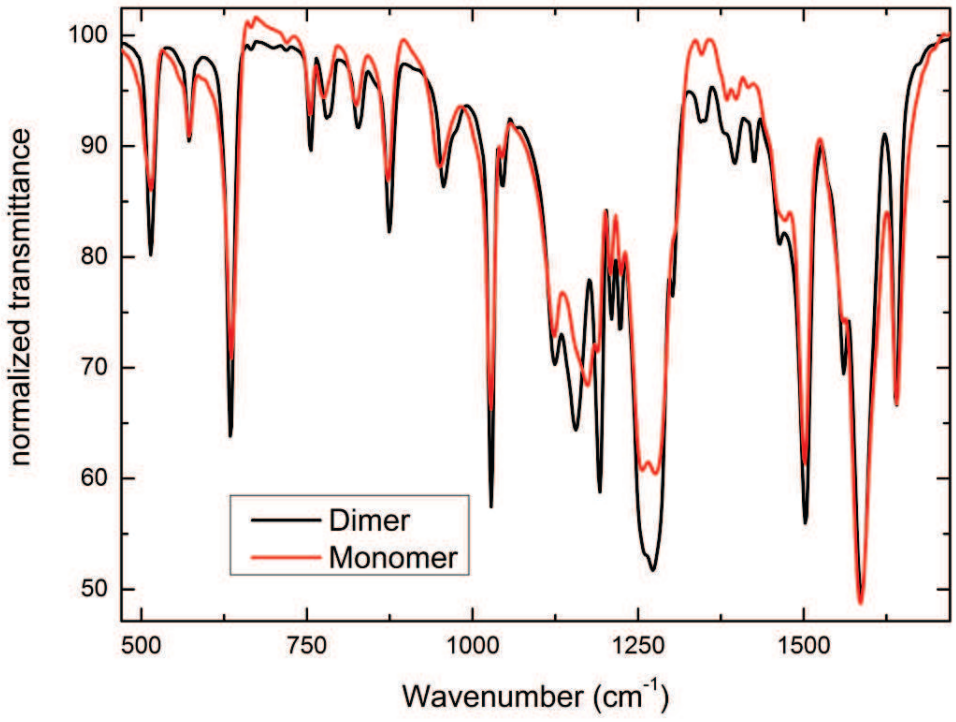

Figure 50 IR spectra of M (red) and D (black) powder samples in KBr .

4.3 2DES

The laser spectrum for 2DES measurements was set broad enough to be able to excite simultaneously states with energy differences until 1400 cm^{-1} but narrow enough to select only a portion of the band. In this way, it is possible to exclude from the spectrum a great number of states present in the absorption band that make the spectrum complicated and the interpretation difficult. No quantum-mechanical calculations are available on the systems to estimate the energy of states included in the absorption band of the PEPEP systems. This made difficult the choice of the most suitable laser band to be used in the 2D spectroscopy. The laser spectrum has thus been tuned to cover a band from 18000 cm^{-1} to 19400 cm^{-1}, as shown in figure 48. This laser band covers the red part of the absorption spectrum in all samples. Because of the great inhomogeneous broadening, the laser excites for sure at least some molecule in the ensemble that, at the time of photoexcitation, occupies the lower vibronic states at that energy. If these molecules are coupled with a vibration of, for example, 700 cm^{-1}, the transition to the first vibrational state is at 18700 cm^{-1}. The molecule that has the 0-0 transition at 18200 cm^{-1} will have its vibronic transition at 18900 cm^{-1} and so on. So, even though the laser spectrum does not cover the whole absorption spectrum, it is still possible to simultaneously excite a sufficient number of vibrational transitions coupled to the electronic one. The time duration of the pulse is 15 fs, measured with frequency resolved optical gating (FROG) at the sample position. The energy of each pulse reaching the sample was about 7 nJ. In order to exclude contribution of coherent spikes and other artifacts in the signal due to pulse overlap, maps are collected from T=50 fs.

Some of the obtained results are summarized in figure 51. At early times, the intensity of the signal is distributed mainly along the diagonal but, as expected, it moves at lower energies at longer T, due to energy relaxation within the excited state. It is also possible to notice the broadening and rounding of the spectrum. This behavior is known as spectral diffusion. It is related to fluctuation of the oscillation frequency of the molecules during T, caused for example by environmental perturbations: in this way molecules excited at a precise frequency emit at slightly different frequencies. The randomness of the process leads to a broader and featureless maps (see also Chapter 1).

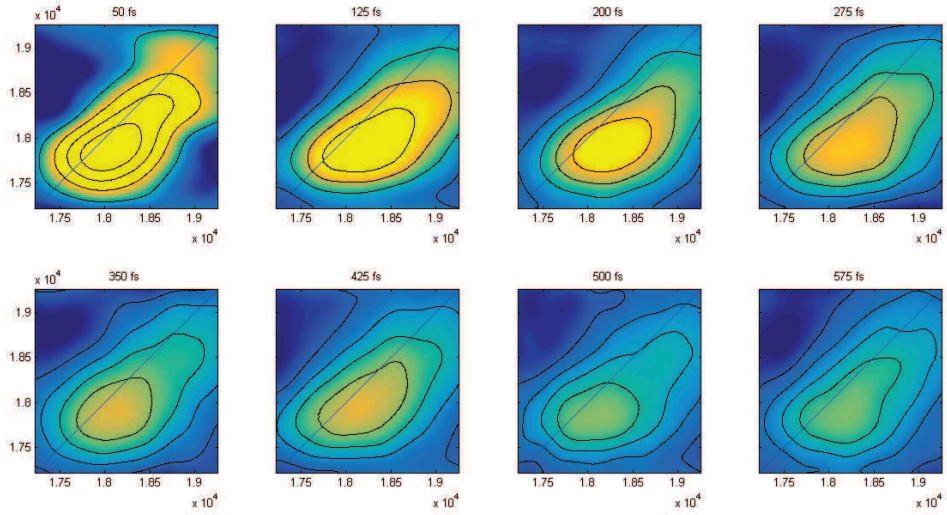

Figure 51 Real rephasing 2D maps of D in d-6 DMSO at increasing values of t_2. Very similar maps have been obtained in DMSO and CH_3CN (not shown here)

However, to find interesting information about coherent dynamics, it is necessary to look more carefully at the evolution of the signal along t_2, in particular at the amplitude oscillations possibly present. As anticipated before, we expected to find oscillations due to vibronic states coupled to the electronic transition. The resonant Raman spectrum should give information of what vibrations are more strongly coupled to the electronic transition. Based on that, since the most intense vibration present in this spectrum is the one at about 1120 cm^{-1}, it was expected to find this oscillation as predominant also in the evolution of 2D maps.

What about the solvent? It is quite common also in literature to find oscillations due to Raman of solvents[68]. The solvent oscillations should last only until the three pulses are temporally overlapped in the sample since the solvent does not have any state resonant with the laser wavelength during the population time. Moreover, Ziegler proposed a method to remove the solvent signal from the molecule's signal. Since there is no energy exchange between radiation and solvent, the solvent oscillations should vanish if the total 3rd order signal is integrated over all detection frequencies[68], [69].

However, experimentally, it was found that the signal is present in the third order signal for times longer than the pulse duration and it was not possible to eliminate the solvent signal with the method proposed

by Ziegler. Nevertheless, if the solvent effect is known, it could be removed or, at least, recognized. For this reason, pure solvents spectra were measured in the same conditions.

The oscillations present in the integrated FFT spectra of the pure solvents are similar to the relative Raman spectra (compared in figure 52a), except for different intensity ratios of bands. Furthermore, the shift of d-6 DMSO bands compared to the DMSO bands is clearly evident. However, in the latter case there is the presence of a significant peak at about 1300 cm^{-1} that is not present in the Raman spectrum.

The same procedure has been applied to all samples. The insets b,c and d of the figure 52 shows the integrated FFT spectra of M and D dissolved respectively in CH_3CN, DMSO and d-6 DMSO, compared with the Raman spectra of M and D powders.

Regarding the samples in CH_3CN, there are some differences in the two spectra. The main peaks are located at about 500, 700 and 900 cm^{-1} for the monomer and 700 and 1200 cm^{-1} for the dimer. In both cases, the oscillations are related to M and D Raman peaks. In fact, 500, 700 and 1200 cm^{-1} are all present in the resonant Raman spectrum of powders. Comparing the integrated FFT spectra with the spectrum of the pure CH_3CN, it is possible to assert that frequencies due to the solvent are not present. In fact, the stronger oscillation present in the CH_3CN spectrum is at 400 cm^{-1} and it is not found nor in M nor in D spectra. The 700 cm^{-1} band could be assigned to the vibrational transition present in the Raman at 640 cm^{-1}. The difference in frequency between Raman and 2D could arise simply because the resolution of the integrated FFT spectra is ≈50 cm^{-1}. This 50 cm^{-1} shift is present also in the spectra of the solvents (see figure 52a).

Concerning the samples in DMSO and d-6 DMSO, the oscillation around 650 cm^{-1} overcomes all other contributions. This mode has a frequency of 700 cm^{-1} in DMSO and of 650 cm^{-1} in d-6 DMSO in agreement with the main peaks in the Raman spectra of solvents. The first hypothesis is to assign this signal to the solvent contribution. However, the spectra are completely different from the contribution of pure solvents as it is possible to appreciate comparing the inset c and d of the figure 52 with the spectra of the pure solvents in panel a.

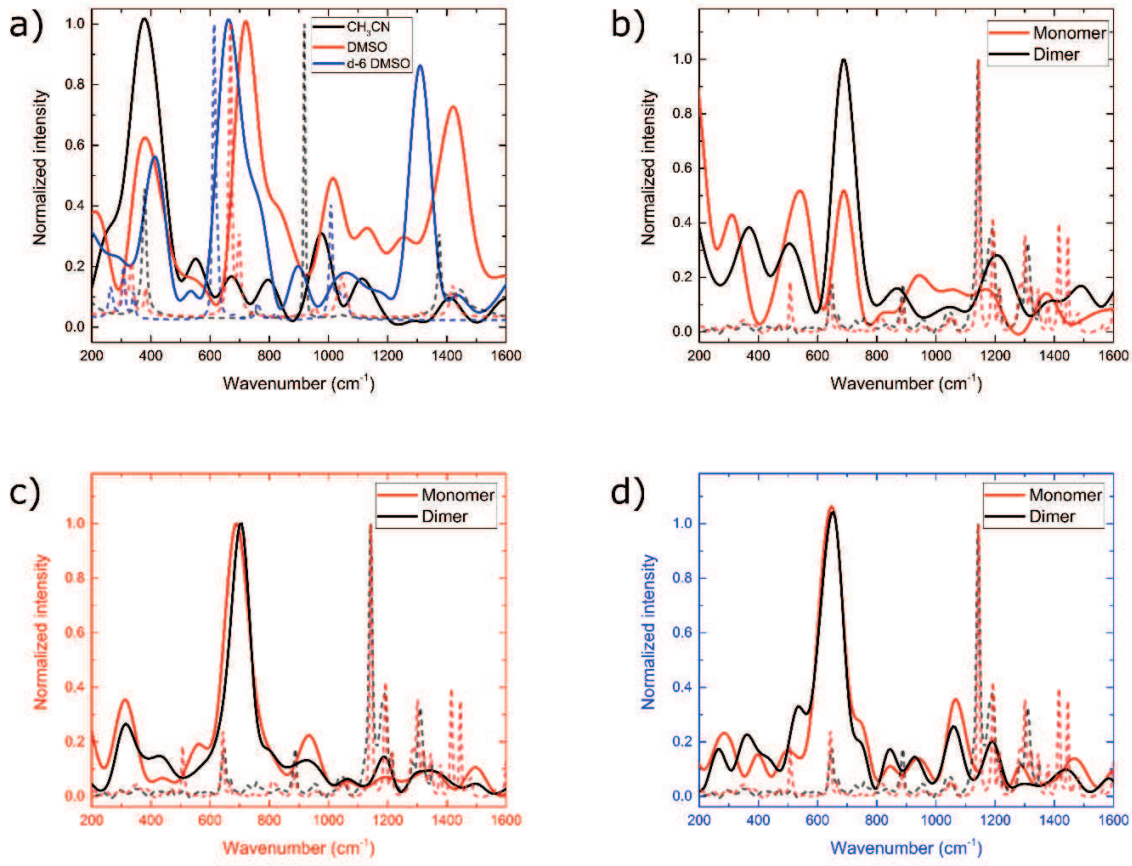

Figure 52 a) Integrated FFT spectra of the three solvents (solid lines), obtained by 2DPE in same conditions of PEPEP measurements, are compared with their raman spectra (dashed lines); CH_3CN: black; DMSO: red and d-6 DMSO: blue. Panels b), c) and d) show the integrated FFT spectra (solid lines) of M (red) and D(black) in CH_3CN, DMSO and d-6 DMSO, respectively, compared with the realtive Raman spectra (dashed lines). The color of the axes reflects the solvent color code of panel (a).

To understand better the nature of this oscillation, it is necessary to look where the oscillations at this frequency are located in the 2D map. As anticipated, in these systems it is not possible to identify the precise energy of the states but, wherever the state in the diagonal is located, a corresponding oscillating signal should be present 650 or 700 cm^{-1} far from the diagonal itself. So it is expected to find oscillating signals in a region parallel to the diagonal and about 700 cm^{-1} far from it. Figure 53 shows, for each sample, the decay traces extracted at 2 points of the map located 650-700 cm^{-1} above and under the diagonal, where that oscillation is supposed to be more intense. The residues of a multi-exponential fit and the associated TFT maps are also shown.

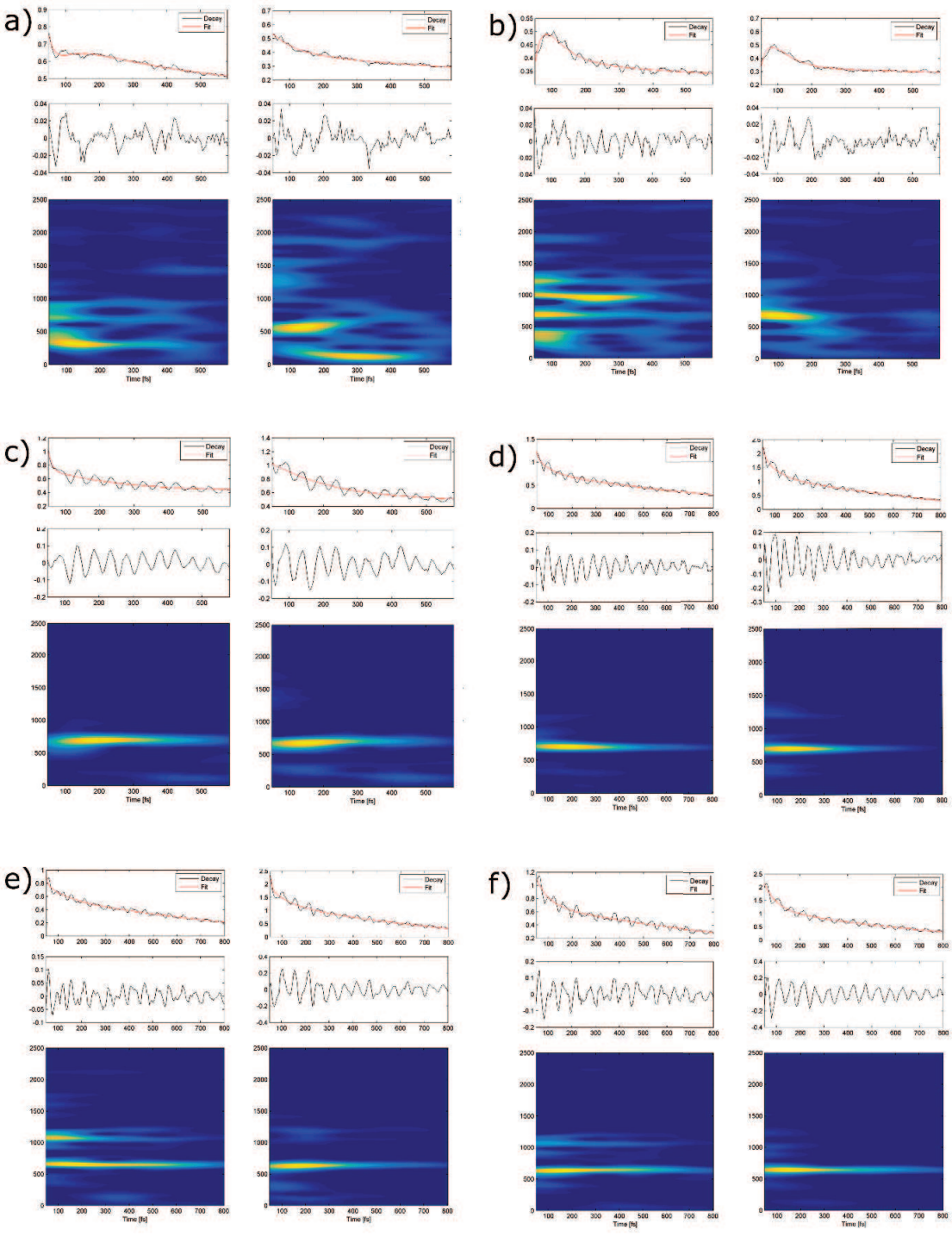

Figure 53 Each panel shows, in the upper part, the decay traces extracted at coordinates 650/700 cm^{-1} above (left) and below (right) the diagonal and the relative multi-exponential fit (red line). In the middle, the residuals of the fit and on the bottom the time-frequency map of residuals. a) and b) are extracted from M and D maps in CH_3CN, respectively; c) and d) from M and D maps in DMSO and e) and f) from M and D maps in d-6 DMSO.

The TFT maps allow comparing the relative intensity and the duration of the oscillations at selected positions. While in the case of CH_3CN, these data do not give any additional information with respect to the integrated FFT map, in DMSO and d-6 DMSO new information could be extracted.

The presence of oscillations of comparable intensity in the upper and lower diagonal points suggest that the oscillation at about 700 cm^{-1} has to be coupled with the excited state of the PEPEP. In fact, oscillations in the upper part of the diagonal could be generated only by vibrations coupled with the excited state[70]. This behavior is present in all spectra of M and D in DMSO and d-6 DMSO. This is a further evidence of the coupling between the vibrational mode of the solvent and the transition of the dyes.

It is possible to do a last consideration about these data. It seems that, in all solvents, the oscillations are more enhanced in the dimer samples. Unfortunately, maps and spectra are normalized because the acquisition method does not allow a comparison of the intensity of the signals. However, in general a better signal-to-noise ratio in the traces and residues means higher oscillations with respect to the signal level.

4.4 FINAL REMARKS

Summarizing the experimental findings of this research, we studied the monomer and a covalently linked dimer of a doubly charged molecule dissolved in very polar solvents to verify the possible presence of interactions between solvents and dyes. We found that, in particular in the systems dissolved in DMSO and d-6 DMSO, a 700 cm^{-1} or 650 cm^{-1} oscillation overcomes all the others. This oscillation is solvent dependent, following the vibrational frequency of the pure solvent detected in the Raman, but it is clearly coupled with the electronic transition of the dye because it is present in the upper cross-peaks. Even though these proofs are not exhaustive to conclude unequivocally that solvent vibrations are involved in the dyes excitation and relaxation, there is some strong suggestion in this direction. However, many other questions find no answer in this experiment. For example:

- Why CH_3CN does not enhance any oscillation?
- Why only the 650-700 cm^{-1} mode is enhanced?
- Why, if confirmed, the oscillations should be more enhanced in the dimer system?
- If our hypothesis is true, how can the solvent interact with the dye at the molecular level?

An attempt of finding an answer to all these doubts can be done imagining the full dye-solvent system. The necessary condition to detect the oscillations induced in the dye response by the solvent is that, in some way, the correspondent vibrational mode has to be excited.

Since the dye has 2 positive charges and the DMSO molecule has a strong dipole moment, it is not completely fanciful to imagine the positive charges in some way 'complexed' by the DMSO molecule. This model of the dye-DMSO system could offer an answer to many of the questions above. Probably, the 700 cm^{-1} vibrational mode is the only one coupled with the electronic transition of PEPEP systems because it can be mixed both geometrically and energetically with the resonant 642 cm^{-1} vibrational mode of the PEPEP itself.

However, also the 929 cm^{-1} of CH_3CN could couple energetically with the 887 cm^{-1} mode of the PEPEP. Probably the nitrogen atom that should complex the positive charge on the dye is less effective than the

oxygen atom of the DMSO and d-6 DMSO, so the positive charge is less affected by the presence of the solvent molecules.

The idea of including the solvent vibrations in the interpretation of the optical properties of dyes is not totally unlikely. In fact, Barone et al. recently found that the shape of the absorption spectrum of chlorophyll a could be simulated in a satisfactory way only when two molecules of solvent, complexing the central metal ion, are included in the ab initio quanto-mechanical calculation[71]. An interesting follow up of these results would be the development of new theoretical models explicitly including the vibrations of the solvent in the description of the optical properties of the system. This would mean include such vibrations in the expression of $g(t)$ (section 1.4). This is not an easy task since it would require a completely new approach in the definition of spectral line shapes.

As final comment, it is worthy to stress that the investigation about the effective role of the solvent molecules more closely surrounding the dye molecule is one of the 'Holy Grail' of the spectroscopy[72], keeping involved scientists since the dawn of spectroscopic techniques. The difficulty in ascertain the real role of such particular solvent molecules is that their behavior is very easily obscured by the (orders of magnitude) greater number of non-interacting solvent molecules. Even we are aware that we are still far from an exhaustive comprehension of the phenomena, we believe that the increasing level of accuracy and sophistication of new experimental techniques, like 2DES, guaranteeing unprecedented levels of clarity in term of frequency and time resolution, will be crucial to gain additional piece of information on this topic. The data reported in this Chapter are a first example in this direction.

CONCLUSIONS

The research work delineated in this thesis has dealt with the study of excitation and relaxation dynamics of different molecular systems. The attention was focused in particular on the characterization of subtle quantum phenomena contributing to the dynamics in the first picosecond after photoexcitiation. The role of quantum coherences and the mechanisms guaranteeing their survival for times longer than expected is currently one of the most hot topic in the field of optical spectroscopy. These phenomena have been invoked for example in biological light-harvesting pigment-protein complexes and started a new and very active research field known as 'quantum biology'. To understand the origin of quantum phenomena in multichromophoric systems and assess the role of different environments in their behavior, two particular model systems have been characterized by means of 2D electronic spectroscopy (2DES) technique.

To this aim, a setup for 2DES was built in our lab, currently representing one of the few available. Special experimental schemes taking advantage of different phase-matching (rephasing, non-rephasing, double quantum), pulse polarization and circular dichroism effects were also tested. A complete toolbox of theoretical formalisms and data analysis software was developed to extract with increasing reliability and accuracy information from the complex 2D signals.

The first model system considered has been porphyrin J-aggregates, a system know to be characterized by strong electronic coupling between monomeric units and very weak coupling with the environment. We were able to unravel the dynamics of intra-band relaxation in TPPS J-aggregates, not easily accessible with other conventional time-resolved techniques. Long lasting vibrational coherences have been found, demonstrating the presence of an unexpected vibronic coupling with two low frequency modes. Moreover, we were able to capture the evolution of an electronic coherence between two excitonic states, thanks to synergic application of different experimental schemes. The fast dephasing of such coherence suggests that vibrational motion does not help electronic coherence to be preserved, as instead suggested for other strongly coupled systems.

Surprising results appeared during the investigation of the second model system, a charged organic molecule (PEPEP) studied both in its monomeric and dimeric forms in different solvents. This system represents the opposite case with respect to the previous one, since the presence of charges make this molecules particularly interacting with the environment, molecules of solvent in particular.

In this system we observed strong oscillations in the excited state dynamic of the dye that could be explained invoking a strong the coupling with a vibration of solvent molecules. If this data will be confirmed, this would be the first observation of vibronic oscillations associated to a vibration of the solvent and not of the molecule itself. However, other experimental confirmations need to be collected to support this hypothesis.

Further development of this work will be the implementation of novel experimental schemes suitably designed to gain more information about the coupling between coherent dynamics and vibronic coupling. A different scheme of 2DES with pump probe geometry instead that BOXCARS phase matching [73], [74] could solve many critical points of the current setup, allowing the investigation of the dynamics in a longer time window, a broader emission frequency range with the use of supercontinuum pulses [75] and an easier acquisition and processing of the experimental data. Moreover, the exploitation of polarized light –not fully successful yet– will be pursued since it could drastically increase the amount of information acquirable from the excited states.

Moreover, more complex multichromophoric systems, characterized for example by inter-molecular energy transfer phenomena will be studied to verify the relevance of quantum effects in transfer rates and efficiencies. In this context, the background of information acquired on the model systems described in this thesis will be of pivotal importance for a correct and reliable interpretation of the data obtained in more complex systems.

References

[1] R. A. Marcus, "Chemical and Electrochemical Electron-Transfer Theory," Nov. 2003.

[2] R. A. Marcus, "On the Theory of Oxidation-Reduction Reactions Involving Electron Transfer. I," *J. Chem. Phys.*, vol. 24, no. 5, p. 966, Dec. 1956.

[3] T. Förster, "Intermolecular energy transference and fluorescence," *Ann Phys.*, vol. 2, pp. 55–75, 1948.

[4] D. L. Dexter, "A Theory of Sensitized Luminescence in Solids," *J. Chem. Phys.*, vol. 21, no. 5, p. 836, Dec. 1953.

[5] "Wiley: Molecular Excitation Dynamics and Relaxation: Quantum Theory and Spectroscopy - Leonas Valkunas, Darius Abramavicius, Tomás Mancal." [Online]. Available: http://eu.wiley.com/WileyCDA/WileyTitle/productCd-3527410082,subjectCd-CH15.html. [Accessed: 28-Jan-2016].

[6] a W. Chin, S. F. Huelga, and M. B. Plenio, "Coherence and decoherence in biological systems: principles of noise-assisted transport and the origin of long-lived coherences.," *Philos. Trans. A. Math. Phys. Eng. Sci.*, vol. 370, no. 1972, pp. 3638–57, Aug. 2012.

[7] P. Drude, "Zur Elektronentheorie der Metalle," *Ann. Phys.*, vol. 306, no. 3, pp. 566–613, 1900.

[8] E. Schrödinger, "An Undulatory Theory of the Mechanics of Atoms and Molecules," *Phys. Rev.*, vol. 28, no. 6, pp. 1049–1070, Dec. 1926.

[9] P. Hamm, "Principles of Nonlinear Optical Spectroscopy : A Practical Approach or : Mukamel for Dummies," 2005.

[10] "Mukamel S. Principles of nonlinear optical spectroscopy (Oxford, 1996)(T)(549s).pdf." .

[11] W. W. Parson, *Modern Optical Spectroscopy: With Examples from Biophysics*. 2009.

[12] M. Blume, "Stochastic theory of line shape: Generalization of the Kubo-Anderson model," *Phys. Rev.*, vol. 174, no. 2, pp. 351–358, 1968.

[13] R. Kubo, *Advances in Chemical Physics*, vol. 15. Hoboken, NJ, USA: John Wiley & Sons, Inc., 1969.

[14] T. Azumi and K. Matsuzaki, "What does the term "vibronic coupling' mean?," *Photochem. Photobiol.*, vol. 25, no. 4, pp. 315–326, 1977.

[15] "Vibronic Coupling: The Interaction Between the Electronic and Nuclear Motions: Gad Fischer: 9780122572401: Books - Amazon.ca." [Online]. Available: http://www.amazon.ca/Vibronic-Coupling-Interaction-Between-Electronic/dp/0122572408. [Accessed: 26-Jan-2016].

[16] A. Tokmakoff, "Time-Dependent Quantum Mechanics and Spectroscopy," 2014.

[17] A. Nemeth, F. Milota, T. Mancal, T. Pullerits, J. Sperling, J. Hauer, H. F. Kauffmann, and N. Christensson, "Double-quantum two-dimensional electronic spectroscopy of a three-level system: Experiments and simulations.," *J. Chem. Phys.*, vol. 133, no. 9, p. 094505, Sep. 2010.

[18] D. B. Turner, R. Dinshaw, K.-K. Lee, M. S. Belsley, K. E. Wilk, P. M. G. Curmi, and G. D. Scholes, "Quantitative investigations of quantum coherence for a light-harvesting protein at conditions simulating photosynthesis.," *Phys. Chem. Chem. Phys.*, vol. 14, no. 14, pp. 4857–74, Apr. 2012.

[19] M. Rey, A. W. Chin, S. F. Huelga, and M. B. Plenio, "Exploiting Structured Environments for E ffi cient Energy Transfer: The Phonon Antenna Mechanism," 2013.

[20] L. Rosenfeld, "Quantum-mechanical theory of the natural optical activity of liquids and gases," *Zeitschrift fuer Phys.*, vol. 52, p. 161, 1928.

[21] B. Nordén, A. Rodger, and T. Dafforn, "Linear Dichroism and Circular Dichroism."

[22] W. Becker, "The bh TCSPC Handbook," *Scanning*, no. 800, pp. 1–566, 2010.

[23] W. Becker and A. Bergmann, "Timing stability of TCSPC experiments," in *Optics East 2006*, 2006, pp. 637209–637209–7.

[24] D. Phillips, R. C. Drake, D. V O'Connor, and R. L. Christensen, "Time Correlated Single-Photon Counting (Tcspc) Using Laser Excitation," *Instrum. Sci. Technol.*, vol. 14, no. 3, pp. 267–292, 1985.

[25] W. Becker, A. Bergmann, and C. Biskup, "Multispectral fluorescence lifetime imaging by TCSPC," in *Microscopy Research and Technique*, 2007, vol. 70, no. 5, pp. 403–409.

[26] I. H. M. van Stokkum, D. S. Larsen, and R. van Grondelle, "Global and target analysis of time-resolved spectra.," *Biochim. Biophys. Acta*, vol. 1657, no. 2–3, pp. 82–104, Jul. 2004.

[27] A. L. Dobryakov, S. A. Kovalenko, A. Weigel, J. L. Pérez-Lustres, J. Lange, A. Müller, and N. P. Ernsting, "Femtosecond pump/supercontinuum-probe spectroscopy: Optimized setup and signal analysis for single-shot spectral referencing," *Rev. Sci. Instrum.*, vol. 81, no. 11, p. 113106, 2010.

[28] C. Manzoni, D. Polli, and G. Cerullo, "Two-color pump-probe system broadly tunable over the visible and the near infrared with sub-30 fs temporal resolution," *Rev. Sci. Instrum.*, vol. 77, no. 2, p. 023103, 2006.

[29] C. Bonetti, M. T. a Alexandre, I. H. M. van Stokkum, R. G. Hiller, M. L. Groot, R. van Grondelle, and J. T. M. Kennis, "Identification of excited-state energy transfer and relaxation pathways in the peridinin-chlorophyll complex: an ultrafast mid-infrared study.," *Phys. Chem. Chem. Phys.*, vol. 12, no. 32, pp. 9256–66, Aug. 2010.

[30] C. Niezborala and F. Hache, "Measuring the dynamics of circular dichroism in a pump-probe experiment with a Babinet-Soleil compensator: erratum," *J. Opt. Soc. Am. B*, vol. 24, no. 4, p. 1012, 2007.

[31] "libra manual on Coherent inc." [Online]. Available: http://lasers.coherent.com/lasers/libra-manual. [Accessed: 28-Jan-2016].

[32] P. F. Tekavec, J. A. Myers, K. L. M. Lewis, F. D. Fuller, and J. P. Ogilvie, "Effects of chirp on two-dimensional Fourier transform electronic spectra.," *Opt. Express*, vol. 18, no. 11, pp. 11015–24, May 2010.

[33] P. Tournois, "Acousto-optic programmable dispersive filter for adaptive compensation of group delay time dispersion in laser systems," *Opt. Commun.*, vol. 140, no. 4–6, pp. 245–249, Aug. 1997.

[34] R. Trebino, K. W. DeLong, D. N. Fittinghoff, J. N. Sweetser, M. A. Krumbügel, B. A. Richman, and D. J. Kane, "Measuring ultrashort laser pulses in the time-frequency domain using frequency-resolved optical gating," *Rev. Sci. Instrum.*, vol. 68, no. 9, p. 3277, Sep. 1997.

[35] A. Nemeth, J. Sperling, J. Hauer, H. F. Kauffmann, and F. Milota, "Compact phase-stable design for single- and electronic spectroscopy," vol. 34, no. 21, pp. 3301–3303, 2009.

[36] T. Brixner, T. Mancal, I. V Stiopkin, and G. R. Fleming, "Phase-stabilized two-dimensional electronic spectroscopy.," *J. Chem. Phys.*, vol. 121, no. 9, pp. 4221–36, Sep. 2004.

[37] R. Augulis and D. Zigmantas, "Two-dimensional electronic spectroscopy with double modulation lock-in detection: enhancement of sensitivity and noise resistance.," *Opt. Express*, vol. 19, no. 14, pp. 13126–13133, 2011.

[38] R. Augulis and D. Zigmantas, "Two-dimensional electronic spectroscopy with double modulation lock-in detection: enhancement of sensitivity and noise resistance.," *Opt. Express*, vol. 19, no. 14, pp. 13126–33, Jul. 2011.

[39] V. P. Singh, A. F. Fidler, B. S. Rolczynski, and G. S. Engel, "Independent phasing of rephasing and non-rephasing 2D electronic spectra.," *J. Chem. Phys.*, vol. 139, no. 8, p. 084201, Aug. 2013.

[40] F. Fassioli, A. Olaya-Castro, and G. D. Scholes, "Coherent Energy Transfer under Incoherent Light Conditions.," *J. Phys. Chem. Lett.*, vol. 3, no. 21, pp. 3136–42, Nov. 2012.

[41] F. V. A. Camargo, H. L. Anderson, S. R. Meech, and I. A. Heisler, "Time-Resolved Twisting Dynamics in a Porphyrin Dimer Characterized by Two-Dimensional Electronic Spectroscopy," *J. Phys. Chem. B*, p. acs.jpcb.5b09964, 2015.

[42] E. E. Ostroumov, R. M. Mulvaney, J. M. Anna, R. J. Cogdell, and G. D. Scholes, "Energy transfer pathways in light-harvesting complexes of purple bacteria as revealed by global kinetic analysis of two-dimensional transient spectra.," *J. Phys. Chem. B*, vol. 117, no. 38, pp. 11349–62, Sep. 2013.

[43] K. M. Mullen and I. H. M. van Stokkum, "The variable projection algorithm in time-resolved spectroscopy, microscopy and mass spectrometry applications," *Numer. Algorithms*, vol. 51, no. 3, pp. 319–340, Sep. 2008.

[44] S. T. Cundiff, "Optical three dimensional coherent spectroscopy.," *Phys. Chem. Chem. Phys.*, vol. 16, no. 18, pp. 8193–200, 2014.

[45] F. Milota, V. I. Prokhorenko, T. Mancal, H. von Berlepsch, O. Bixner, H. F. Kauffmann, and J. Hauer, "Vibronic and vibrational coherences in two-dimensional electronic spectra of supramolecular J-aggregates.," *J. Phys. Chem. A*, vol. 117, no. 29, pp. 6007–14, 2013.

[46] A. Volpato and E. Collini, "Time-frequency methods for coherent spectroscopy.," *Opt. Express*, vol. 23, no. 15, pp. 20040–50, Jul. 2015.

[47] J. Prior, E. Castro, A. W. Chin, J. Almeida, S. F. Huelga, and M. B. Plenio, "Wavelet analysis of molecular dynamics: efficient extraction of time-frequency information in ultrafast optical processes.," *J. Chem. Phys.*, vol. 139, no. 22, p. 224103, Dec. 2013.

[48] E. E. Jelly, "No Title," *Nature*, vol. 139, p. 631, 1937.

[49] G. Scheibe, "No Title," *Angew. Chem.*, vol. 50, p. 212, 1937.

[50] J. Franck and E. Teller, "Migration and Photochemical Action of Excitation Energy in Crystals," *J. Chem. Phys.*, vol. 6, no. 12, p. 861, Dec. 1938.

[51] T. Kobayashi, *J-Aggregates*, vol. 2. 2012.

[52] A. S. R. Koti and N. Periasamy, "Self-Assembly of Template-Directed J-Aggregates of Porphyrin," *Chem. Mater.*, vol. 15, no. 2, pp. 369–371, 2003.

[53] S. . Ma, "Theoretical studies on the structural change in the N-protonated meso-tetrakis(p-sulfonatophenyl)porphyrin," *Chem. Phys. Lett.*, vol. 332, no. December, pp. 603–610, 2000.

[54] T. Kobayashi, *J-Aggregates*. World scientific, 1996.

[55] E. W. Knapp, "Lineshapes of molecular aggregates, exchange narrowing and intersite correlation," *Chem. Phys.*, vol. 85, no. 1, pp. 73–82, Mar. 1984.

[56] M. A. Castriciano, A. Romeo, G. De Luca, V. Villari, L. M. Scolaro, and N. Micali, "Scaling the chirality in porphyrin J-nanoaggregates.," *J. Am. Chem. Soc.*, vol. 133, no. 4, pp. 765–7, Feb. 2011.

[57] N. Micali, V. Villari, M. A. Castriciano, A. Romeo, and L. Monsù Scolaro, "From fractal to nanorod porphyrin J-aggregates. Concentration-induced tuning of the aggregate size.," *J. Phys. Chem. B*, vol. 110, no. 16, pp. 8289–95, Apr. 2006.

[58] M. A. Castriciano, A. Romeo, V. Villari, N. Micali, and L. M. Scolaro, "Structural Rearrangements in 5,10,15,20-Tetrakis(4-sulfonatophenyl)porphyrin J-Aggregates under Strongly Acidic Conditions," *J. Phys. Chem. B*, vol. 107, no. 34, pp. 8765–8771, Aug. 2003.

[59] T. K. Chandrashekar, H. Van Willigen, and M. H. Ebersole, "Optical and electron spin resonance study of cation and cation-crown ether induced dimerization of tetrakis(4-sulfonatophenyl)porphyrin," *J. Phys. Chem.*, vol. 88, no. 19, pp. 4326–4332, Sep. 1984.

[60] G. Panitchayangkoon, D. Hayes, K. a Fransted, J. R. Caram, E. Harel, J. Wen, R. E. Blankenship, and G. S. Engel, "Long-lived quantum coherence in photosynthetic complexes at physiological temperature.," *Proc. Natl. Acad. Sci. U. S. A.*, vol. 107, no. 29, pp. 12766–12770, 2010.

[61] H. E. Ungnade, "The Effect of Solvents on the Absorption Spectra of Aromatic Compounds," *J. Am. Chem. Soc.*, vol. 75, no. 2, pp. 432–434, 1953.

[62] X. Liu, J. M. Cole, and K. S. Low, "Solvent effects on the uv-vis absorption and emission of optoelectronic coumarins: A Comparison of three empirical solvatochromic models," *J. Phys. Chem. C*, vol. 117, no. 28, pp. 14731–14741, 2013.

[63] M. Homocianu, "Solvent effects on the electronic absorption and fluorescence spectra," *J. Adv. Res. Phys.*, vol. 2, no. 1, p. 011105, 2011.

[64] W. R. Ware, "Nanosecond Time-Resolved Emission Spectroscopy: Spectral Shifts due to Solvent-Excited Solute Relaxation," *J. Chem. Phys.*, vol. 54, no. 11, p. 4729, 1971.

[65] E. Collini, L. Bolzonello, M. Zerbetto, C. Ferrante, N. Manfredi, and A. Abbotto, "Lifetime Shortening and Fast Energy-Tansfer Processes upon Dimerization of a A-π-D-π-A Molecule," *ChemPhysChem*, vol. 15, no. 2, pp. 310–319, 2014.

[66] C. Sissa, F. Terenziani, A. Painelli, A. Abbotto, L. Bellotto, C. Marinzi, E. Garbin, C. Ferrante, and R. Bozio, "Dimers of quadrupolar chromophores in solution: electrostatic interactions and optical spectra.," *J. Phys. Chem. B*, vol. 114, no. 2, pp. 882–93, 2010.

[67] R. Signorini, C. Ferrante, D. Pedron, M. Zerbetto, E. Cecchetto, M. Slaviero, I. Fortunati, E. Collini, R. Bozio, A. Abbotto, L. Beverina, and G. a Pagani, "Effective two-photon absorption cross section of heteroaromatic quadrupolar dyes: dependence on measurement technique and laser pulse characteristics.," *J. Phys. Chem. A*, vol. 112, no. 18, pp. 4224–34, 2008.

[68] R. Moca, S. R. Meech, and I. A. Heisler, "Two-Dimensional Electronic Spectroscopy of Chlorophyll a: Solvent Dependent Spectral Evolution," *J. Phys. Chem. B*, vol. 119, no. 27, pp. 8623–8630, 2015.

[69] S. Constantine, Y. Zhou, J. Morais, and L. D. Ziegler, "Dispersed optical heterodyne detected birefringence and dichroism of transparent liquids," *J. Phys. Chem. A*, vol. 101, no. 30, pp. 5456–5462, 1997.

[70] D. B. Turner, K. E. Wilk, P. M. G. Curmi, and G. D. Scholes, "Comparison of Electronic and Vibrational Coherence Measured by," pp. 1904–1911, 2011.

[71] V. Barone, M. Biczysko, and M. Borkowska-panek, "A Multifrequency Virtual Spectrometer for Complex Bio- Organic Systems : Vibronic and Environmental Effects on the UV / Vis Spectrum of Chlorophyll a," pp. 3355–3364, 2014.

[72] A. Tokmakoff, "Private communication." .

[73] S.-H. Shim and M. T. Zanni, "How to turn your pump-probe instrument into a

multidimensional spectrometer: 2D IR and Vis spectroscopies via pulse shaping.," *Phys. Chem. Chem. Phys.*, vol. 11, no. 5, pp. 748–61, Feb. 2009.

[74] J. A. Myers, K. L. Lewis, P. F. Tekavec, and J. P. Ogilvie, "Two-color two-dimensional Fourier transform electronic spectroscopy with a pulse-shaper," *Opt. Express*, vol. 16, no. 22, p. 17420, Oct. 2008.

[75] P. F. Tekavec, J. A. Myers, K. L. M. Lewis, and J. P. Ogilvie, "Two-dimensional electronic spectroscopy with a continuum probe," *Opt. Lett.*, vol. 34, no. 9, p. 1390, Apr. 2009.